

University of Southern Queensland  
Faculty of Health, Engineering and Sciences

# **Analysis of Circular Section blade profiles in a Simple Peripheral Drag VAWT: Design Investigations and Performance Modelling**

A dissertation submitted by

**Kristan Sedgman**

in fulfilment of the requirements of  
**ENG4111 and 4112 Research Project**

towards the degree of  
**Bachelor of Engineering (Honours) (Mechanical)**

Submitted October, 2016

# Abstract

Global demand for off grid power generation in remote and rural locations and in low socio-economic communities has renewed interest in the use of hybrid Vertical Axis Wind Turbines (VAWTs). This type of wind turbine is more easily manufactured using simple construction techniques and materials than other wind turbine designs. They are also able to produce useable power at lower wind speeds. The use of a simple numerical modelling tool to predict the behaviour of novel hybrid Savonius and Simple Peripheral Drag (SPD) turbines would allow analysis of the performance of designs prior to construction. This would allow tailoring of a turbine design to specific local operating conditions. To enable this, investigations were undertaken to ascertain the usefulness of CFD in data generation of SPD blade performance data using ANSYS software, correlated with wind tunnel experiments. This data was then used in a MATLAB simulation script to predict the behaviour of numerically modelled turbines using a range of variables.

While useful in showing the characteristics of flow around individual SPD blades, the CFD data generated did not reflect the wind tunnel results accurately, and the wind tunnel data was used for numerical modelling in its place. The quasi-static numerical model created in MATLAB showed that increasing turbine radius increased acceleration but reduced maximum velocity. Additionally it was seen that 180° arc angle SPD blades gave better acceleration and maximum at lower wind speeds but with lower maximum velocity at higher wind speeds. However no wind tunnel correlations were undertaken and the accuracy of the model was unable to be determined. It is suggested, however, that due to the complex nature of turbulent flow around the turbine blades, the quasi-static modelling approach may have limited applicability. Further research into modelling methods may be required before reliable predictions of performance can be made.

© University of Southern Queensland  
University of Southern Queensland  
Faculty of Health, Engineering and Sciences

## ENG4111 & ENG4112 Research Project

### **Limitations of Use**

The Council of the University of Southern Queensland, its Faculty of Health, Engineering and Sciences, and the staff of the University of Southern Queensland, do not accept any responsibility for the truth, accuracy or completeness of material contained within or associated with this dissertation.

Persons using all or any part of this material do so at their own risk, and not at the risk of the Council of the University of Southern Queensland, its Faculty of Health, Engineering and Sciences or the staff of the University of Southern Queensland.

This dissertation reports an educational exercise and has no purpose or validity beyond this exercise. The sole purpose of the course pair entitles “Research Project” is to contribute to the overall education within the student’s chosen degree program. This document, the associated hardware, software, drawings, and any other material set out in the associated appendices should not be used for any other purpose: if they are so used, it is entirely at the risk of the user.

# **Certification**

I certify that the ideas, designs and experimental work, results, analyses and conclusions set out in this dissertation are entirely my own effort, except where otherwise indicated and acknowledged.

I further certify that the work is original and has not been previously submitted for assessment in any other course or institution, except where specifically stated.

Kristan Sedgman

Student Number: 0061045908

# Acknowledgements

I would like to thank Dr Ray Malpress for sharing the little time and considerable knowledge he has.

I would also like to thank Mr Andreas Helwig for his inspiring conversations and for offering this interesting project for students to be a part of.

Additionally I thank the staff at the University of Southern Queensland who have assisted me over the last year, particularly Ruth Mossad, Adrian Blockland, Khalid Saleh and Prof. Andrew Wandel.

I would also like to thank my partner for her patience through the last 6 years of our life, nearly done now my dear.

# Table of Contents

## Contents

Abstract .....	ii
Limitations of Use.....	iii
Certification .....	iv
Acknowledgements .....	v
Table of Contents .....	vi
List of Figures .....	x
Glossary of terms .....	xiii
1. Introduction .....	1
1.1 Background .....	1
1.2 Aims and Objectives .....	1
1.3 Project Scope.....	2
2. Literature Review .....	7
2.1 CFD literature review.....	7
2.1.1 Computational Fluid Dynamics .....	7
2.1.2 ANSYS program – equations.....	7
2.1.3 Meshing.....	7
2.1.4 Wall models .....	8
2.1.5 Turbulence in CFD.....	8
2.1.6 SST turbulence modelling.....	9
2.1.7 Mesh independency.....	9
2.1.8 Domain.....	10
2.1.9 Boundary conditions .....	10
2.2 Wind Tunnel Literature Review.....	10
2.2.1 Wind Tunnels.....	10
2.2.2 Tunnel types.....	10
2.2.3 Inlet considerations .....	11
2.2.4 Test section considerations .....	11
2.2.5 Blockage effects .....	11
2.2.6 Measurement methods .....	12
2.3 VAWT Literature Review.....	12
2.3.1 Vertical Axis Wind Turbines .....	12
2.4 Additive Manufacture Literature Review .....	15
2.4.1 Additive manufacture.....	15
3. Methodology .....	17
3.1 CFD Methodology .....	17

3.1.1 Geometry.....	17
3.1.2 Meshing.....	17
3.1.3 Mesh Independency process .....	19
3.1.4 Solution discovery.....	20
3.2 Wind Tunnel Testing Methodology .....	20
3.2.1 Tunnel Information .....	20
3.2.2 Test Apparatus .....	21
3.2.3 Testing Procedure .....	22
3.3 Additive Manufacturing Methodology .....	23
3.4 MATLAB Methodology .....	23
4. Results.....	26
4.1.1 CFD results .....	26
4.1.2 CFD Results Discussion.....	28
4.2.1 Wind Tunnel Results.....	31
4.2.2 Wind Tunnel Results Discussion .....	34
4.2.3 Dimensionless Analysis .....	35
4.3 MATLAB Results .....	37
4.3.1 Arc angle comparison .....	37
4.3.2 Offset comparison .....	39
4.3.3 Turbine Radius Comparison .....	40
4.3.4 Blade Number Comparison.....	40
4.4 MATLAB Results Discussion.....	41
4.4.1 Optimum Offset .....	41
4.4.2 Optimum Arc Angle.....	42
4.4.3 Optimum Blade Number .....	42
5. Discussion .....	44
5.1 Experimental Procedure .....	44
5.2 Test Apparatus .....	44
5.3 CFD analysis .....	45
5.4 Numerical Modelling .....	45
5.5 Wind Tunnel Testing of a Prototype Turbine .....	46
5.6 Benefits .....	46
6. Conclusion .....	48
6.1 Contribution .....	48
6.2 Further work.....	49
6.3 Reflection .....	49
Bibliography.....	51
Appendices.....	- 1 -
<b>Appendix A .....</b>	<b>- 1 -</b>

<b>A1 Project Specification .....</b>	<b>- 1 -</b>
<b>Appendix B .....</b>	<b>- 2 -</b>
<b>B1 Risk Management Plan .....</b>	<b>- 2 -</b>
<b>B2 Test Apparatus Base .....</b>	<b>- 9 -</b>
<b>B3 Pitot Assembly and Graduation Collar .....</b>	<b>- 9 -</b>
<b>B4 STL File For 3D Printing.....</b>	<b>- 10 -</b>
<b>B5 Force Measurement Assembly .....</b>	<b>- 10 -</b>
<b>Appendix C .....</b>	<b>- 11 -</b>
<b>C1 Risk Management Plan.....</b>	<b>- 11 -</b>
<b>C2 Scales comparison .....</b>	<b>- 18 -</b>
<b>C3 Test Rig on Wind Tunnel.....</b>	<b>- 19 -</b>
<b>C4 Assembled Test Rig .....</b>	<b>- 20 -</b>
<b>Appendix D .....</b>	<b>- 20 -</b>
<b>D1 MATLAB code .....</b>	<b>- 20 -</b>
<b>D1.1 Main Script .....</b>	<b>- 20 -</b>
<b>D1.2 veloc Function.....</b>	<b>- 22 -</b>
<b>D1.3 apparent Function.....</b>	<b>- 23 -</b>
<b>D1.4 det_range Function .....</b>	<b>- 24 -</b>
<b>D1.5 get_ws_data Function .....</b>	<b>- 24 -</b>
<b>D1.6 get_angles Function.....</b>	<b>- 26 -</b>
<b>D1.7 get_forces Function .....</b>	<b>- 26 -</b>
<b>D1.8 get_torc Function .....</b>	<b>- 27 -</b>
<b>D2 Variable Comparison.....</b>	<b>- 29 -</b>
<b>D2.1 Blade arc angle comparison data.....</b>	<b>- 29 -</b>
<b>D2.2 Blade Number comparison data .....</b>	<b>- 31 -</b>
<b>D2.3 Turbine Radius comparison data .....</b>	<b>- 33 -</b>
<b>D3 MATLAB Simulation data: 0.75ms<sup>-1</sup>.....</b>	<b>- 37 -</b>
<b>D3.1 Acceleration with Offset data.....</b>	<b>- 37 -</b>
<b>D3.2 Velocity with Offset data .....</b>	<b>- 38 -</b>
<b>D3.3 Tip Speed with Offset data .....</b>	<b>- 39 -</b>
<b>D4 MATLAB Simulation data: 7.0ms<sup>-1</sup>.....</b>	<b>- 41 -</b>
<b>D4.1 Acceleration with Offset data.....</b>	<b>- 41 -</b>
<b>D4.2 Velocity with Offset data .....</b>	<b>- 42 -</b>
<b>D4.3 Tip Speed with Offset data .....</b>	<b>- 43 -</b>
<b>E1 CFD Force Data.....</b>	<b>- 44 -</b>
<b>E2 Domain for Transient Solution.....</b>	<b>- 45 -</b>
<b>E3 Mesh Refinement for Transient Solution .....</b>	<b>- 46 -</b>
<b>E4 Inflation on Blade for Transient Solution .....</b>	<b>- 47 -</b>
<b>E5 Transient Solution Parameters .....</b>	<b>- 48 -</b>



<b>E6 Pressure field for Transient Solution.....</b>	<b>- 50 -</b>
<b>E7 Velocity field for Transient Solution.....</b>	<b>- 50 -</b>
<b>E8 Turbulent Kinetic Energy for Transient Solution.....</b>	<b>- 51 -</b>
<b>F1 Wind Tunnel spreadsheet data.....</b>	<b>- 52 -</b>
<b>F2 Dimensionless Parameter Table .....</b>	<b>- 54 -</b>
<b>F3 Plots of Dimensionless Parameters.....</b>	<b>- 55 -</b>

## List of Figures

Figure 1: Potential layout of a hybrid Savonius(bottom) and SPD (top)wind turbine cluster. ....	2
Figure 2: Idealisation of the SPD (Simple Peripheral Drag) VAWT design. ....	3
Figure 3: Some of the SPD design parameters (plan view). ....	4
Figure 4: CFD results showing the flow field around traditional (a) and Bach (b) style VAWT rotors ( Flow coloured by velocity magnitude).(Source: Zhou et.al, 2013) .....	5
Figure 5: Helical Savonius configurations showing various twist angles. (Source: Lee et. al, 2015) .....	13
Figure 6: Various end plate configurations for a helical VAWT (Source: Jeon et.al, 2014) .....	14
Figure 7: Domain for CFD analysis showing the 3 mesh size areas. ....	18
Figure 8: Meshing applied to the 3 domain regions. ....	18
Figure 9: Inflation of the boundary layer mesh from an initial cell thickness of 0.01mm to regional mesh size of 0.15mm (region C). ....	19
Figure 10: Comparison of x direction force results from the CFD analysis with wind tunnel data (CFD dashed lines, wind tunnel solid lines) at the tested wind speeds of 6.6 ms <sup>-1</sup> , 15.1 ms <sup>-1</sup> and 20.1 ms <sup>-1</sup> .....	27
Figure 11: Comparison of the y direction force results from the CFD analysis with wind tunnel data (CFD dashed lines, wind tunnel solid lines) at the tested wind speeds of 6.6 ms <sup>-1</sup> , 15.1 ms <sup>-1</sup> and 20.1 ms <sup>-1</sup> .....	27
Figure 12: Pressure fields and velocity vectors for the 180° blade at 0° offset and 180° offset angles. ....	29
Figure 13: Pressure fields and velocity vectors for the 120° blade at 0° offset and 180° offset angles. ....	30
Figure 14: Pressure fields around a 180° blade from 15° offset to 60° offset angle. At 30° and 45° vortex flow is closer to the trailing surface of the blade. ....	31
Figure 15: Plot of x direction forces from wind tunnel data interpolated over a full revolution (180° arc solid line, 120° arc dashed line) at the tested wind speeds of 6.6 ms <sup>-1</sup> , 15.1 ms <sup>-1</sup> and 20.1 ms <sup>-1</sup> . ....	32
Figure 16: Plot of y direction forces from wind tunnel data interpolated over a full revolution (180° arc solid line, 120° arc dashed line) at the tested wind speeds of 6.6 ms <sup>-1</sup> , 15.1 ms <sup>-1</sup> and 20.1 ms <sup>-1</sup> . ....	32
Figure 17: Radar plot of the net force results from wind tunnel testing (180° arc solid line, 120° arc dashed line), interpolated over a full 360° revolution. ....	33
Figure 18: Sample ANSYS fluent solution showing approximate locations of the inner three static pressure readings taken by the Pitot tube (black circles). ....	35
Figure 19: Plot of C <sub>D</sub> vs Re for (180° and 120°) blades at their maxima and minima C <sub>D</sub> angles .....	36
Figure 20: Plot of C <sub>L</sub> vs Re for (180° and 120°) blades at their maxima and minima C <sub>L</sub> angles. ....	36
Figure 21: Angular velocity of 180° and 120° arc blades in 0.75 ms <sup>-1</sup> wind speed (0° offset data used for comparison). ....	37
Figure 22: Angular velocity of 180° and 120° arc blades in 7.0 ms <sup>-1</sup> wind speed (0° offset data used for comparison). ....	38
Figure 23: Rotational anomaly for 180° blade in 0.75 ms <sup>-1</sup> wind at -15° and -30° offset. ....	39
Figure 24: Comparison of rotational velocity for a three 180° bladed turbine in 0.75 ms <sup>-1</sup> wind, showing both 0.03 m radius and a 0.01 m radius geometry. ....	40
Figure 25: Comparison of 5 and 3 bladed turbines at 0.75 ms <sup>-1</sup> wind speed (both 180° blades). ....	41
Figure 26: Risk management plan image 1. ....	- 2 -
Figure 27: Risk management plan image2. ....	- 3 -

Figure 28: Risk management plan image 3. ....	- 4 -
Figure 29: Risk management plan image 4. ....	- 5 -
Figure 30: Risk management plan image 5. ....	- 6 -
Figure 31: Risk management plan image 6. ....	- 7 -
Figure 32: Risk management plan image 7. ....	- 8 -
Figure 33: LENS printed base and universal joint with load cells attached. ....	- 9 -
Figure 34: Test specimen with graduated collar fitted (top) and complete Pitot tube and microcontroller assembly (bottom).....	- 9 -
Figure 35: Creo model ready to be transferred as an *.stl file for LENS printing. ....	- 10 -
Figure 36: Test specimen with graduation collar fitted in universal joint ready for wind tunnel testing. ....	- 10 -
Figure 37: Risk management plan image 1. ....	- 11 -
Figure 38: Risk management plan image 2. ....	- 12 -
Figure 39: Risk management plan image 3. ....	- 13 -
Figure 40: Risk management plan image 4. ....	- 14 -
Figure 41: Risk management plan image 5. ....	- 15 -
Figure 42: Risk management plan image 6. ....	- 16 -
Figure 43: Risk management plan image 7. ....	- 17 -
Figure 44: Image 1 from the verification process of the jewellery scales. A range of 0.04 grams was seen between the 3 scales. This was far below the level of fluctuations experienced in the wind tunnel testing. ....	- 18 -
Figure 45: Image 2 from the verification process of the jewellery scales. ....	- 18 -
Figure 46: Image 3 from the verification process of the jewellery scales. ....	- 19 -
Figure 47: Photograph of the testing apparatus on top of the wind tunnel test section, inlet to the left hand side of the image. The Pitot tube can be seen inserted into one of the 6 self-sealing slots available. ....	- 19 -
Figure 48: Photograph of the assembled test apparatus showing the Pitot tube for pressure data acquisition (left) and a test specimen connected through to the force measurement apparatus. The static pressure reading ports on the Pitot tube are too small to be seen in this image, and are about 2cm from the tip of the tube. ....	- 20 -
Figure 49: Comparison of (3) blade arc angles at $0.75 \text{ ms}^{-1}$ . ....	- 29 -
Figure 50: Comparison of (3) blade arc angles at $7.0 \text{ ms}^{-1}$ . ....	- 29 -
Figure 51: Comparison of (5) blade arc angles at $7.0 \text{ ms}^{-1}$ . ....	- 30 -
Figure 52: Comparison of $180^\circ$ vs $120^\circ$ blades at $0.75 \text{ ms}^{-1}$ . ....	- 30 -
Figure 53: Comparison of (5) blade arc angles at $7.0 \text{ ms}^{-1}$ . ....	- 31 -
Figure 54: Comparison of $(120^\circ)$ blade numbers at $0.75 \text{ ms}^{-1}$ . ....	- 31 -
Figure 55: Comparison of $(120^\circ)$ blade numbers at $7.0 \text{ ms}^{-1}$ . ....	- 32 -
Figure 56: Comparison of $(180^\circ)$ blade numbers at $0.75 \text{ ms}^{-1}$ . ....	- 32 -
Figure 57: Comparison of $(180^\circ)$ blade numbers at $7.0 \text{ ms}^{-1}$ . ....	- 33 -
Figure 58: Comparison of $(120^\circ)$ turbine radius at $0.75 \text{ ms}^{-1}$ . ....	- 33 -
Figure 59: Comparison of $(120^\circ)$ turbine radius at $7.0 \text{ ms}^{-1}$ . ....	- 34 -
Figure 60: Comparison of $(180^\circ)$ turbine radius at $0.75 \text{ ms}^{-1}$ . ....	- 34 -
Figure 61: Comparison of $(180^\circ)$ turbine radius at $7.0 \text{ ms}^{-1}$ . ....	- 35 -
Figure 62: Comparison of $(0.03 \text{ m})$ turbine blade angle at $0.75 \text{ ms}^{-1}$ . ....	- 35 -
Figure 63: Comparison of $(0.03 \text{ m})$ blade angle at $7.0 \text{ ms}^{-1}$ . ....	- 36 -
Figure 64: Angular acceleration of all offsets for $180^\circ$ blade at $0.75 \text{ ms}^{-1}$ . ....	- 37 -
Figure 65: Angular acceleration of all offsets for $120^\circ$ blade at $0.75 \text{ ms}^{-1}$ . ....	- 37 -
Figure 66: Angular velocity for all offsets of $180^\circ$ blade at $0.75 \text{ ms}^{-1}$ . ....	- 38 -
Figure 67: Angular velocity for all offsets of $120^\circ$ blade at $0.75 \text{ ms}^{-1}$ . ....	- 38 -
Figure 68: Tip speed for all offsets of $180^\circ$ blade at $0.75 \text{ ms}^{-1}$ . ....	- 39 -
Figure 69: Tip speed for all offsets of $120^\circ$ blade at $0.75 \text{ ms}^{-1}$ . ....	- 39 -
Figure 70: Comparison of angular velocity for $180^\circ$ vs $120^\circ$ blades at $7.0 \text{ ms}^{-1}$ . ....	- 40 -
Figure 71: Angular acceleration of all offsets for $180^\circ$ blade at $7.0 \text{ ms}^{-1}$ . ....	- 41 -

Figure 72: Angular acceleration of all offsets for 120° blade at 7.0 ms <sup>-1</sup> . .....	- 41 -
Figure 73: Angular velocity for all offsets of 180° blade at 7.0 ms <sup>-1</sup> . .....	- 42 -
Figure 74: Angular velocity for all offsets of 120° blade at 7.0 ms <sup>-1</sup> . .....	- 42 -
Figure 75: Tip speed for all offsets of 180° blade at 7.0 ms <sup>-1</sup> . .....	- 43 -
Figure 76: Tip speed for all offsets of 120° blade at 7.0 ms <sup>-1</sup> . .....	- 43 -
Figure 77: EXCEL worksheet showing the total x and y components of force from the CFD solutions for the 180° blade at the three wind speeds tested. ....	- 44 -
Figure 78: Domain of the transient solution mesh showing the three separate meshing regions. ....	- 45 -
Figure 79: Image showing the three relative mesh sizes in each zone, used for the transient solution. ....	- 46 -
Figure 80: Close up of the mesh around the blade surface region showing inflation from the surface, the 0.2mm rounded corners, and the triangular mesh (for the transient solution). ....	- 47 -
Figure 81: Solution parameters image 1, transient setup and mesh statistics. ....	- 48 -
Figure 82: Transient solution setup using PISO scheme and the transition SST turbulence model, suitable for flows where separation of the boundary layer is apparent. ....	- 49 -
Figure 83: Pressure field from transient solution showing detached vortex in low pressure (blue) region of the flow. ....	- 50 -
Figure 84: Velocity field from the transient solution showing high velocity flow (red) on the lower side of the image, and lower velocity flow (blue) on the upper side of the image, with some flow back across the rear side of the blade from the vortex. ....	- 50 -
Figure 85: Turbulent kinetic energy regions from the transient solution. ....	- 51 -
Figure 86: EXCEL spreadsheet 1 for wind tunnel data. ....	- 52 -
Figure 87: EXCEL spreadsheet showing C <sub>D</sub> and C <sub>L</sub> for various Re values. ....	- 54 -
Figure 88: Plot of C <sub>D</sub> vs Re for 180° blade. ....	- 55 -
Figure 89: Plot of C <sub>L</sub> vs Re for 180° blade. ....	- 55 -
Figure 90: Plot of C <sub>D</sub> vs Re for 120° blade. ....	- 56 -
Figure 91: Plot of C <sub>L</sub> vs Re for 120° blade. ....	- 56 -

Table 1: Table showing the 3 top offsets in terms of angular velocity at the later stages of the initial acceleration phase. ....	41
-----------------------------------------------------------------------------------------------------------------------------------	----

# Glossary of terms

SPD: Simple Peripheral Drag

VAWT: Vertical Axis Wind Turbine

Offset: angle between the centreline of a blade and the tangential vector

Arc angle: internal circular arc describing the blade extent

CFD: Computational Fluid Dynamics

RANS: Reynolds Averaged Navier Stokes equations

SRANS: Steady Reynolds Averaged Navier Stokes equation

$y^+$ : Dimensionless wall distance

$y$ : normal distance to wall

$u$ : time averaged velocity of flow

$\tau_w$ : wall shear stress value

$\rho$ : Density

$\mu$ : Viscosity

$u_\tau$ : wall friction velocity

Re: Reynolds number

$C_D$ : Coefficient of drag

$C_L$ : Coefficient of lift

F: force

m: mass

a: acceleration

I: mass moment of inertia

r: radius

$\tau$ : Torque

$\alpha$ : Angular acceleration

$\omega$ : angular velocity

PISO: Pressure Implicit with Splitting of Operators

SST: Shear Stress Transport

LES: Large Eddy Simulation

DES: Detached Eddy Simulation

DNS: Direct Numerical Simulation

STL: Stereo Lithography

FFF: Fused Filament Fabrication

LENS: Laser Engineered Net Shaping

UV: Ultraviolet

PLA: Polylactic Acid

ABS: Acrylonitrile Butadiene Styrene

PIV: Particle Imaging Velocimetry

# **1. Introduction**

## **1.1 Background**

In 2013 the International Energy Agency released their “World Energy Outlook 2013” document (IEA 2013), in which they state that 1.3 Billion people around the globe live without access to electricity in their homes. This has many negative consequences, including lower than average literacy rates and health problems (Kanagawa & Nakata 2008). One study regarding the effects of access to household electrification in Madagascar (Daka & Ballet 2011) showed increased scholastic abilities in children, especially females, with associated health benefits and reduced social reproduction rates. Another study showed 82% of householders with access to off-grid electricity spent time reading in the evenings, against only 53% of householders without access to off-grid electricity (Gustavsson 2007). Researchers (Dornan & Shah) have shown that investment in modern and efficient energy generation, combined with access to this power, leads to positive economic benefits in surrounding communities.

Renewable off-grid energy production is also aligned with the University of Southern Queensland’s Food Security and Regional Resilience initiatives. These projects aim to ensure that innovation and progress in the areas of infrastructure, natural resources and agriculture allow regional Australia to remain competitive and prosperous into the future.

## **1.2 Aims and Objectives**

Renewable energy resources that could be promoted as solutions to this need for off-grid energy production are hydrokinetic power, wind power and solar power. In this study the development of wind resource harvesting is pursued, due mainly to the fact that wind is readily accessible, and can be gathered by relatively simple equipment, most of which could potentially be constructed using recycled materials. The task then, is to design a low technology hybrid wind turbine which can operate at lower wind speeds than conventional commercial wind turbine technology, and demonstrate self-furling behaviour under adverse wind conditions. This work is part of the multi-disciplinary research work associated with permanent magnet alternators that operate with no cogging torque that make low wind speed wind harvesting possible. The other main aim of the project is that the turbine can be manufactured in low income communities using simple production techniques and predominantly recycled materials.



*Figure 1: Potential layout of a hybrid Savonius(bottom) and SPD (top)wind turbine cluster.*

### 1.3 Project Scope

The project scope was to create a model that can be used to predict some of the optimum design values for a small scale wind turbine, given input parameters by a user. The type of turbine design used was nominated by one of the project supervisors to match the permanent magnet no cogging alternator design, and thus selection of turbine is not a consideration. The chosen design is a hybrid Savonius and Simple Peripheral Drag (SPD) VAWT system (fig.1), of which the Peripheral Drag components are to be investigated in this model.

Peripheral drag refers to the use of several blades of a partial circular section, arranged about the turbines axis at some distance, together producing a net torque on the turbines shaft when exposed to airflow (fig.2). Even though the peripheral drag system is not uncommon, very little literature is available describing performance characteristics or optimal configuration. Most literature relating to VAWT design addresses the Savonius and Darrieus designs, both of which fit different niches within the VAWT market. These being that the Savonius design has superior self-starting characteristics at lower wind speeds, and the Darrieus design has a higher coefficient of power at its optimum operating wind speed ('HAWT versus VAWT: Small VAWTs find a clear niche' 2003).



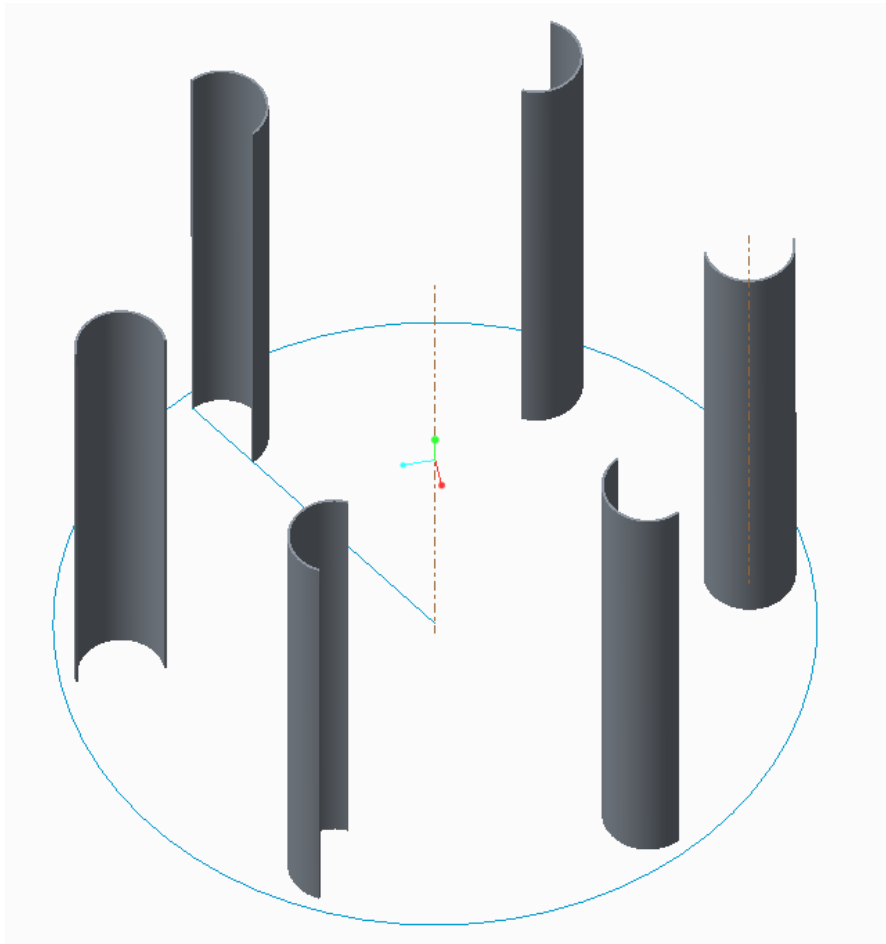


*Figure 2: Idealisation of the SPD (Simple Peripheral Drag) VAWT design.*

The SPD system is to be incorporated into the design of this hybrid VAWT in the hope that it can increase the power production at higher tip speeds where the Savonius power curve begins to level out (Roy & Ducoin 2016), without detrimental effects at lower speeds. While not as efficient as the Darrieus design, peripheral drag components are far easier to manufacture with simple tools and materials.

The SPD system can be described by several of its design parameters, including (fig.3)...

- Blade diameter (the diameter of the circular section the blade is produced from)
- Blade arc (the fraction of a full circle that the blade section represents)
- Blade offset (the angle between the normal face of the blade and the tangential path of the turbine), positive offset turning the open face towards the axis.
- Rotor diameter (the distance between the centre of the circular blade section and the turbine axis of rotation)
- Blade number (the number of equally spaced blades on the turbine)
- Blade length (the longitudinal dimension of the blade)

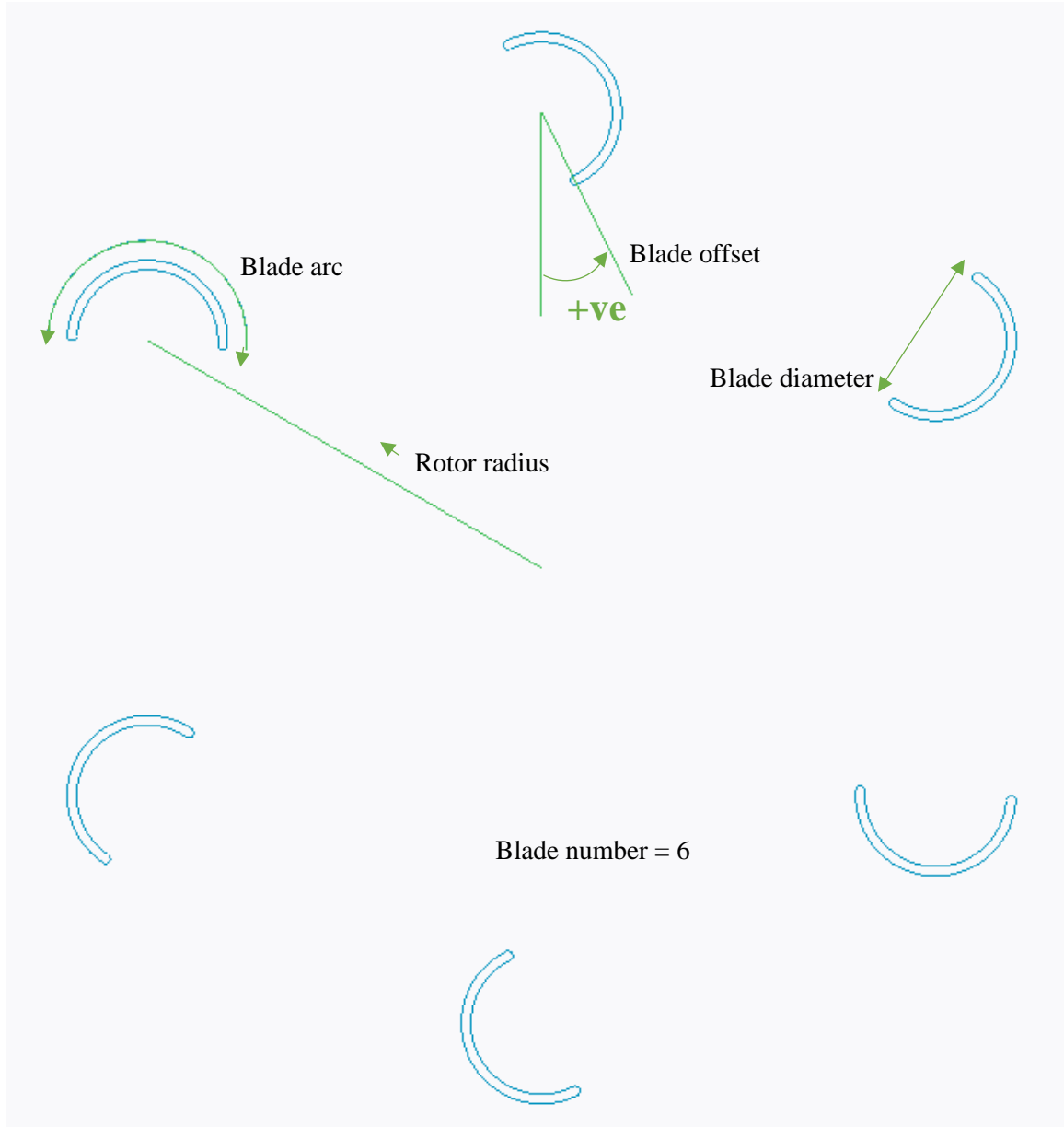


Figure 3: Some of the SPD design parameters (plan view).

Literature on the optimisation of Savonius style VAWT's was investigated as a reference point for this study. One study of note (Zhou & Rempfer 2013) investigated the effect of blade shape on the performance of Savonius turbines, and concluded that the traditional  $180^\circ$  arc (semicircular) blade shape was not the best option for power generation, and that the Bach style rotor gave superior results. The results of this study indicated that some portion of the power produced by Savonius turbines was due to lift effects generated by airflow over the blades (fig.4). However it was noted that the close proximity of the blades in the Savonius layout affected the nature of the flow around the turbine, a feature not present in the SPD design.

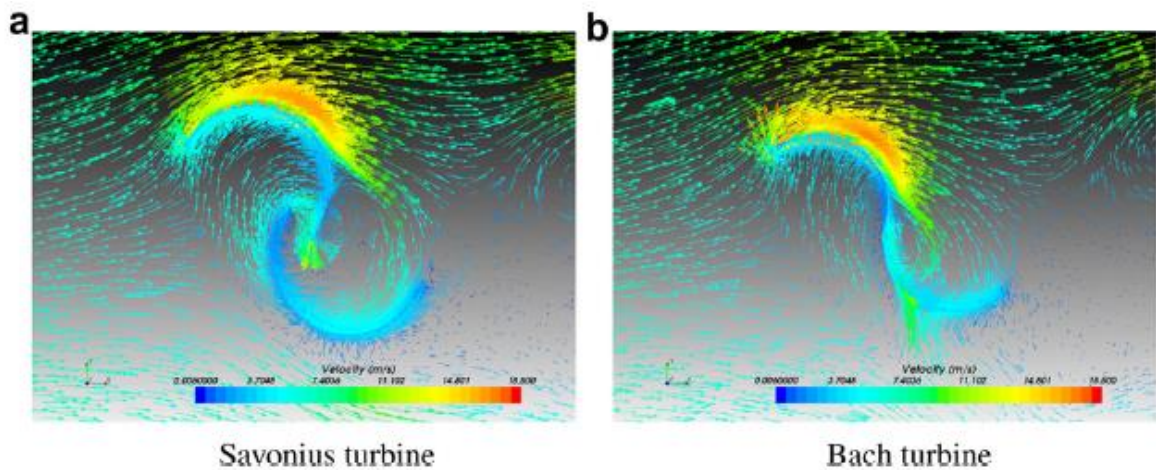


Figure 4: CFD results showing the flow field around traditional (a) and Bach (b) style VAWT rotors ( Flow coloured by velocity magnitude). (Source: Zhou et.al, 2013)

This discovery prompted the desire to further investigate the generation of lift effects on circular sectioned VAWT blades. In the interests of sustainable promoting sustainable resource usage, the decision was made to compare 180° and 120° blade arcs, these representing whole fractions of a circular section, meaning no waste material would be generated in the construction of blades from a length of pipe.

Investigations into this phenomena were undertaken using a combination of Computational Fluid Dynamics (CFD) software and more traditional wind tunnel testing. The flow fields around the two 180° and 120° arcs were modelled with CFD software, and the resulting forces on these sections determined. This gave both qualitative and quantitative data to be examined. Wind tunnel testing of blades of the same dimensions as those used in the CFD models was then performed, to assess the level of correlation between the physical and numerical systems. These tests were carried out at a range of wind speeds and arc offsets to give a representation of the forces on the blades over a full revolution of a turbine at varying wind conditions. The data from these tests was analysed to determine what, if any, lift effects were observable, and whether the 120° arc blades were suitable to be used as design components for any turbine models, or whether to abandon this variant from the rest of the project.

The next aim of the project was to create a numerical modelling program to allow prediction of a novel turbine design. Given the associated input parameters, the forces generated by airflow over the simulated blades would be determined by interpolating force values generated by CFD analysis and stored as datum values in the model. To simplify the modelling process somewhat, only the blade offset, turbine radius and wind magnitude would be variable components of this initial model. It was expected that this would allow an optimal offset angle to be determined through incremental adjustment of this variable. Once this optimal offset value was determined, other variables could be introduced to the model.

The result of these investigations would be a relatively simple modelling package that could give an approximation of the performance of an SPD VAWT design, given the values of certain variables. A program such as this would allow determination by a user of the approximate performance of a novel SPD VAWT without the need to construct several prototypes and test their performance. This in turn would save time and

resources, and ensure that a design would generate the required amount of power for a particular application over the range of local wind speeds expected.

This ability to minimise resource requirements would allow communities or organisations to design a VAWT system to meet their individual needs before committing to any expenditure. Generation of reliable off-grid power will give impoverished communities another tool to use in the fight for a better education and improved standard of living. It will also allow remote regions to improve their power security by assisting on site construction and modification of simple small scale wind turbines.

## **2. Literature Review**

### **2.1 CFD literature review**

#### **2.1.1 Computational Fluid Dynamics**

Computational Fluid Dynamics (CFD) utilizes computers to solve numerical simulations of fluid systems (Tu 2013). Several approaches have been taken towards this end, mostly characterised by the explicit or implicit equations used to solve the system. These include the Finite Element methods, Finite Difference methods, Finite Volume methods also some meshless methods (Roy & Saha 2013). Excluding the meshless methods, these all involve solving systems of differential equations relating individual adjacent nodes of a meshed system.

#### **2.1.2 ANSYS program – equations**

The ANSYS CFD program uses the finite volume method for its governing equations. The Reynolds Averaged Navier Stokes equations (RANS) are used to determine the solution to the discretised equations of the system, with various turbulence models used in addition depending on the nature of the system being modelled. These RANS equations are time averaged equation used to describe fluid flow, and particularly turbulent flows. There are numerous sources describing their derivation and use, and as such they will not be discussed any further in this paper. The turbulence models are required to complete the RANS equations, namely the fluctuating component of the flow. This program has previously been used for modelling of VAWTs, for example (Deda Altan et al. 2016) and (Shaheen et al. 2015), both studies quite similar to this one.

#### **2.1.3 Meshing**

Meshing is the process of discretising a 2D or 3D domain into individual elements (nodes). Two main types of mesh are typically used, structured and unstructured. Each has advantages and disadvantages that make them more applicable to particular flow conditions (Tu 2013). Structured meshes are often used adjacent to wall surfaces as they are suited to capture boundary layer characteristics, while unstructured meshes are typically used in far field flows where they can fill volumes without cell skewness effects. While structured grids are more stable and converge faster when used with implicit formulations and unstructured grids are easier to apply with explicit formulae, some promising attempts have recently been made into methods that work equally well on both mesh types (Çete et al. 2008).

### 2.1.4 Wall models

Special functions are often used in the regions of CFD meshes adjacent to walls to accurately capture the boundary layer effects in the flow (Tu 2013). It is important to pay special attention to the solution of this region, particularly in the case of wind turbine blades, as this is often the region of most interest. The size and inflation of the grid in this region should be assessed using the  $y^+$  criterion to determine its likely efficacy. The  $y^+$  variable refers to the dimensionless wall distance, and is affected by the particular flow properties for a region of a system. Below is a description of the mathematics relating to this variable...

$y$  = normal distance to the wall

$y^+$  = dimensionless wall distance

$u$  = time averaged velocity parallel to the wall

$\tau_w$  = wall shear stress value

$\rho$  = fluid density

$\mu$  = fluid viscosity

$u_\tau$  = wall friction velocity

$$u_\tau = \sqrt{\tau_w / \rho}$$

$$u^+ = u / u_\tau$$

$$y^+ = y \rho u_\tau / \mu$$

It can be seen the  $y^+$  variable is a function of the flow properties. Usually an iterative process is required to determine its value, by determining the wall shear stress from a solution, using this to find the local  $y^+$  value and then altering the mesh size until a suitable  $y^+$  value is achieved. A value of at least 1 is usually desired in the node adjacent to the wall. In nodes where the  $y^+$  is less than 5, viscous forces dominate the fluids behaviour, and this region is referred to as the viscous sub-layer. For  $y^+$  values greater than 5 turbulent diffusion effects are encountered, and a different numerical relationship is sought. It should also be apparent that as flow behaviour changes along a surface, so too will the  $y^+$  value, meaning grid refinement may be a lengthy procedure that needs to be repeated for the same surface under different conditions.

### 2.1.5 Turbulence in CFD

Modelling of turbulence is required to achieve an accurate energy balance in the numerical solution by accounting for turbulent kinetic energy. There are a multitude of models used to determine how turbulence is created and accounted for, in the case of modelling VAWTs success has been had using the SST model, albeit with some over prediction of power coefficients in 2D simulations (Roy & Saha 2013). Large Eddy Simulations (LES) and Detached Eddy Simulations (DES) have shown better results,

however with a great deal more computational resource requirements. In one study showed how turbulence model choice could affect the time taken to reach a solution. Using the Steady Reynolds Averaged Navier Stokes (SRANS) equations took 7.2 hours to solve, while LES and DES models took 120.0 hours to solve the same system (Liu & Niu 2016).

### **2.1.6 SST turbulence modelling**

The SST turbulence model (Menter 1996) is a two equation model that differentiates between different parts of the system it is employed in. For regions adjacent to surfaces it uses the  $(k - \varepsilon)$  turbulence model to more accurately predict boundary layer conditions. Further away from these regions the  $(k - \omega)$  turbulence model is used to stabilize the system against turbulence effects introduced by inlet conditions. The  $(k - \varepsilon)$  and  $(k - \omega)$  models are themselves two equation models, each using slightly different approaches to simulate turbulence effects. This results in the SST model being a four equation turbulence model, accounting for both turbulent kinetic energy ( $k$ ), and a scaling effects that describe the length of turbulence ( $\varepsilon, \omega$ ) in the different regions of the domain being studied. This turbulence model is therefore suited to flows that encounter transitions from laminar flow regions (boundary layers) to turbulent flow regions, such as wind turbine systems.

### **2.1.7 Mesh independency**

Mesh independency is another aspect of CFD meshing that is worth considering during any investigation into a system. One investigation into the nature of mesh independency (Almohammadi et al. 2013) noted that an independent mesh is one in which reducing the size of the elements will not affect the resulting solution. It went on to investigate how successful several different mesh independency tests were at finding this element size in a 2D system. The conclusion reached was that the success of mesh independency determination was reliant on the nature of the system studied, and different methods may be required depending on the system at hand.

The importance of mesh independency is due to the computational requirement of CFD investigations. Using a mesh that is too coarse may result in inaccurate results that do not fully and accurately describe the flows within a system. On the other hand, using a grid with an excessive number of nodes will require increased computational resources to obtain a solution, with no improvement in the quality of the results obtained. The same study mentioned above recommended that for a 2D aerofoil simulation, in a suitably sized domain, an independent solution would require at least 400,000 nodes, assuming that the mesh was structured in a suitable manner. It was also noted that other studies that ran simulations with node numbers in the multiples of millions, did not have any evidence of mesh independency.

### **2.1.8 Domain**

Selection of a suitable domain for a CFD study is an important decision. The domain describes the outer limits of the mesh used in the analysis, and is where boundary conditions for the study are set (Tu 2013). It is important that the boundaries for the system are far enough from the region of interest to allow convergence of the equations to an accurate solution.

### **2.1.9 Boundary conditions**

Boundary conditions are used to define the initial values used in solution of the discretised equations for the CFD study. Typical examples of boundary conditions include constant pressure, constant velocity, constant heat flux, constant temperature and constant mass flow rate. A combination of boundary conditions is applied to at least two faces of a fluid system to describe the nature of the flow under study. Using the properties of the fluid being studied, the governing equations of the CFD model will be solved iteratively.

After each iteration a balance of the system is taken with respect to the boundary conditions imposed. Any imbalance in the system is shown as a residual values for each node. Values of each node are then altered between iterations in an attempt to correct for any imbalance. When the total number of iterations is reached, or the average residuals reach a predefined lower limit, the system is said to be converged. Residuals can refer to masses, forces, velocities or variables related to the governing equations used.

## **2.2 Wind Tunnel Literature Review**

### **2.2.1 Wind Tunnels**

Wind tunnel testing is an important tool for the study of fluid dynamics, offering the researcher the ability to control different aspects of a system systematically, and document the results of changes. In a typical scenario a test sample or object will be placed in a test section of the wind tunnel, exposed to fluid flow, and some data (qualitative or quantitative) measured. Some commonly utilised variables include velocity of the fluid (air) stream, angle of the test sample relative to the airflow direction, and shape of the test sample.

### **2.2.2 Tunnel types**

Wind tunnels can be divided into two broad groups, recirculating and single pass systems. Recirculating systems direct exhaust air from the test section back to the inlet, thus re-using fluid momentum already generated in previous passes of the tunnel. If used in



conjunction with a closed test section, this also allows for conditioning of the fluid, for example, changing the pressure above or below atmospheric pressure, changing the fluid temperature, or using non atmospheric gases. One distinct drawback of a recirculating wind tunnel is the larger volume required to extend the tunnel into a loop.

Single pass wind tunnels do not re-use exhaust air from the test section, and instead simply discharge the exhaust to the atmosphere. They require a smaller footprint than the recirculating tunnel model, and cannot modify fluid properties beyond the mass flowrate through the test section. Despite this, their relative simplicity of design and lower cost make them an attractive option where atmospheric flow is the primary fluid regime of interest.

### **2.2.3 Inlet considerations**

Both wind tunnel types are required to condition the fluid flow entering the test section to some degree. It is generally preferable to have a uniform laminar flow field through the test section of the tunnel. In some cases it is necessary to account for a minimal, or prescribed, amount of turbulence in the flow. Commonly this is achieved by using a converging section at the inlet of the test section, with an interface structure across the tunnel to encourage either laminar flow, or flow with a predetermined amount of turbulence. This could be as simple as a section of wire mesh across the tunnel.

### **2.2.4 Test section considerations**

The test section may be one of two general types, closed or open. Closed test sections are bounded by walls to restrict all flow to the cross sectional area of the test section, while open test sections have no walls, and allow flow to interact somewhat with the local atmospheric conditions. Open test sections are often used when a test sample is large relative to the test section, and blockage effects need to be reduced.

### **2.2.5 Blockage effects**

Blockage effects are (typically unwanted) effects caused by incompressible fluid flow between an object and the bounding walls of the test section. As per Bernoulli's hypothesis, the reduced area that the incompressible flow has available to it either side of the test specimen causes changes in the flows characteristics. As the mass flowrate must be the same through all sections of the tunnel, the flow velocity will increase around the test specimen. After passing the specimen the area available to the flow increases again, and some pressure differential may result as part of the flow reduces velocity.

The effect of this is that the flow interacting with a test specimen is different from the flow introduced into the inlet of the wind tunnel. Pressure differentials that are not present in the real system will skew the results obtained from the test. Also, a flow modelled at, for example,  $10 \text{ ms}^{-1}$ , will actually interact with the test specimen at  $12 \text{ ms}^{-1}$ , again skewing the results of the test.

There has been quite a bit of literature devoted to quantifying the effects of blockage in wind tunnels, and how to deal with it. One review of blockage correction (Ross & Altman 2011) studied several different blockage correction methods. It found that further research is necessary to determine a definitive correction strategy, as no single strategy could account for all situations posed. The conclusion was reached that awareness of blockage effects is an important consideration when designing and analysing experimental procedures. The same study also drew attention to the difference in blockage effects between static and dynamic models of the same geometry and instantaneous orientation to the flow.

A more specific study on blockage effects in an open test section (Roy & Saha 2014) concluded that blockage ratio and wind speed values were not sufficient to determine the required blockage correction for different tip speed ratios and torque values of a Savonius turbine. However, it notes that for small blockage ratios (less than 10%) in open test sections, the blockage correction required is negligible. For closed sections a blockage ratio of 2.0% to 3.5% has been deemed small enough to give negligible blockage effects (Ross & Altman 2011).

## **2.2.6 Measurement methods**

Data that may be taken from wind tunnel test includes

- Flow velocities
- Pressure values
- Force values
- Turbulence intensity
- Temperatures
- Vorticity

The data of interest to this project was the forces experienced by the test specimen, however pressure and velocity measurements were also used to attempt a correlation between the wind tunnel test data and the CFD predictions. Details of the exact measurement techniques employed is covered in the methodology section of this report.

## **2.3 VAWT Literature Review**

### **2.3.1 Vertical Axis Wind Turbines**

Vertical Axis Wind Turbines have received renewed interest due to increasing awareness of the environmental impact of fossil fuel use for power generation and rising energy resource costs for consumers. This increase interest has been driven by the evolution of materials and production techniques during the latter part of the 20<sup>th</sup> century (Tjiu et al. 2015). While technology has played its part in the construction of VAWTs, it has also allowed better research into their operating principals and allowed better design analysis.

Research into improving the self-starting characteristics of the Savonius type VAWTs, one of their major advantages, has led to the concept of using multiple stacked units, as well as investigations into the optimum number of buckets per rotor (Sheldahl et al. 1978). These small alterations have contributed a significant increase in the effectiveness of Savonius type VAWTs in low wind speed conditions. Another study (Shaheen et al. 2015) have investigated the increase in performance resulting from selective placement of adjacent Savonius turbines within close proximity to one another. This study noted a 34% increase in the power co-efficient of clustered Savonius VAWTs compared to isolated units, due to the interaction of the flow field amongst the clustered units.

Advances in manufacturing techniques have enabled researchers to investigate the use of helical shaped Savonius buckets (fig.5). Turbines utilising this blade shape enjoy smoother power delivery compared to the traditional straight bucket turbines, as well as improved self-starting characteristics (Saha & Rajkumar 2006), with a twist angle of  $15^\circ$  from the vertical axis of revolution found to give optimum results in terms of the rotors performance. It should be noted that the construction of helical buckets may require more technical effort than using simple straight buckets.

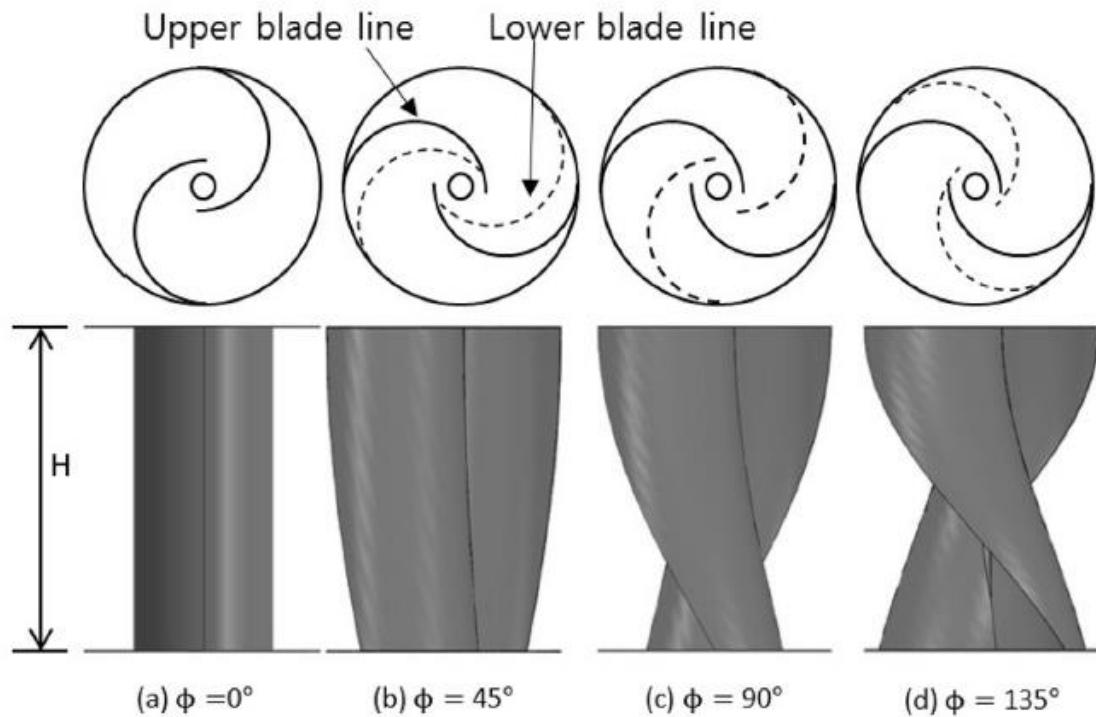


Figure 5: Helical Savonius configurations showing various twist angles. (Source: Lee et. al, 2015)

The effect of end plates (fig.6) on the performance of Savonius rotors has also been studied, both numerically and using wind tunnel experiments. One study (Jeon et al. 2015) showed a significant improvement in the performance of Savonius turbines utilising various configurations of end plates has been observed. The full circular end plate showed the best improvement out of the designs tested. The end plates serve to stop flow of air around the upper and lower ends of the blade, increasing the flow around the

sides, and therefore increasing the useful momentum transfer from the oncoming air stream.

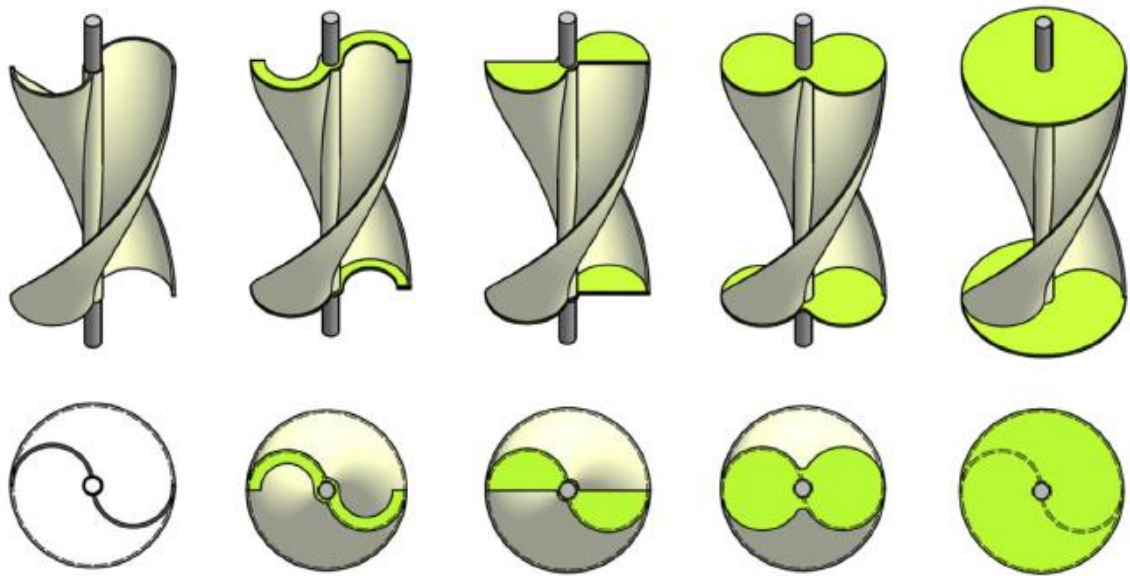


Figure 6: Various end plate configurations for a helical VAWT (Source: Jeon et.al, 2014)

It is widely noted in the literature that the relative positioning of Savonius buckets to one another has a large effect on the performance of the turbine. The overlap ratio between the inner edges of the buckets on a 2 rotor Savonius turbine has been determined to give maximum efficiency at an overlap ratio of 0.15 (Akwa et al. 2012). This was due to the flow of air between the advancing and retreating buckets, reducing the pressure difference across the advancing blade.

Research into SPD type VAWTs was sparse, only literature that was non peer reviewed could be found by the author. This is probably due to the better performance of Darrieus and Savonius VAWTs and the resulting interest in them by both academia and industry. Nevertheless, it seems likely that some of the research methods applied to Savonius rotors is applicable to SPD designs. This is due to the probable similarities in flow characteristics between their similar blade profiles. While the flow around an isolated SPD blade is likely to vary greatly compared to the flow produced by interaction between adjacent Savonius blades, structures such as end plates would likely have identical effects on both systems.

## 2.4 Additive Manufacture Literature Review

### 2.4.1 Additive manufacture

Additive Manufacture, also referred to as 3D printing or stereolithography, is the process of forming a structure by successive addition of layers of a construction material. This process results in the ability to form constructs that other more traditional subtractive fabrication methods are unable to replicate. There are many different methods and materials used to form these layers, with a range of mechanical properties and economic considerations. Two additive manufacturing methods were available for use in this project. Fused Filament Fabrication (FFF) in the form of heated polymer filaments, and Laser Engineered Net Shaping (LENS) utilizing a UV laser cured resin.

The FFF machines used either Polylactic Acid (PLA) or Acrylonitrile Butadiene Styrene (ABS) filaments. Investigation into the mechanical properties of components manufactured using PLA (Farah et al.) has determined a maximum tensile stress in samples of 60 MPa immediately after manufacture, reducing to 40 MPa after 3 months of ageing. Another study (Dawoud et al. 2016) determined a maximum tensile strength for ABS printed components of 34.3 MPa, however it noted that this value was higher in injection moulded processes.

The available FFF units available were the UPBOX and UPBOX mini, capable of 0.1 mm vertical layer thickness at maximum resolution (UP3D 2015). Thicker layers were possible, resulting in a decrease in production time, but with an associated increase in surface roughness. This roughness is due to the thickness of the individual layers of deposited material, and their tendency to “squash out” at the sides of the print. PLA prints can be surface treated after deposition to decrease this roughness by soaking in an acetone vapour bath. The acetone vapour partially melts the outer surface of the printed item, allowing the individual layer edges to run together. This process also increases the durability of the printed object, reducing the number of surface defects that may initiate fracture under strain.

The LENS UV curing machine available was a ProJet® 3500 HD. In its highest resolution this machine will produce items with a thickness resolution of 0.032mm. The manufacturing process for this type of printer does not use extruded material, but rather focused UV laser light. The light produces a reaction in a UV sensitive resin, which then hardens into a solid. To allow cavities to be produced, a second material can be printed alongside the resin, a wax which melts above 60 °C. The ProJet printer available was equipped with a proprietary resin, namely VisiJet® M3 Crystal. When cured, this material exhibits a tensile strength of 42.4 MPa (3dsystems 2015). Total possible build size for the ProJet machine is 298 mmx 185 mm x 203 mm (xyz).

In terms of sustainability, PLA is the most preferable choice for additive manufacturing material. It is a non-toxic biodegradable material, commonly produced from natural renewable resources (Farah et al.). However, anecdotal advice to the author indicated that this material was more prone to fatigue failure than ABS or UV cured resins. Some investigation of low cycle fatigue failure was found in the literature (Senatov et al. 2016), however this was in relation to compression loading of lattices of PLA, and not to the small fluctuating loads that may be expected during operation of a small scale wind turbine.

After consideration of the options, the UV curing printer was selected for production of some of the data collection apparatus. Its ability to deliver components with acceptable mechanical properties at the highest resolution was the deciding factor. This would allow the use of small air galleries for pressure measurement, and the ability to mate components and test pieces without necessitating any further machining of any parts. A risk management plan was instigated to ensure safe procedure during the use of the LENS printer and subsequent processing (Appendix B1).

## 3. Methodology

### 3.1 CFD Methodology

#### 3.1.1 Geometry

The geometry used in the CFD modelling was created using the ANSYS Designmodeler package. The simulation was run as a 2D model to reduce computational time restraints, a practice not uncommon in CFD analysis (Almohammadi et al. 2013). The domain of the study was modelled as a rectangular representation of the test section of the wind tunnel, intersecting the centre of the test blade horizontally, with the domain extending five times the diameter of the test blade upwards of the blade, ten times downwind, and five times either side (fig.7).

The test blades were modelled as 20mm outside diameter with 1mm wall thickness, matching the test blades used in the wind tunnel tests. The sections were divided with a radial line originating at the centre of the circle. Early meshes indicated that sharp edges around the corners of the blade caused problems, with poor convergence of the solution. For this reason 0.2mm radii were introduced to the corners of the model where the circular faces met the radial intersecting faces see (fig.9).

For each incremental angle tested, the radial lines were redefined in the Designmodeler geometry, resulting in a change in the apparent offset angle of the test blade around the centre of the 20mm diameter. One of the radial lines was designated as the “offset” angle, while the other radial line was set as a fixed angle from the offset line, keeping the arc of the blade at the set  $120^\circ$  or  $180^\circ$  required for the model. The offset angle was redefined as a parameter, while the arc angle was not changed. This resulted in an axis of rotation offset from the axis of rotation of the physical test blade. This small detail would have no appreciable difference in the results, and was done for convenience after problems modelling the CFD blade rotation about the blade surface.

#### 3.1.2 Meshing

The 400mm x 200mm domain of the model was divided into 3 distinct regions for the meshing process. Each had a different resolution depending on the flow characteristics expected. Each region will be referred to as region A, B or C (fig.7). The dimensions of the regions were modified through a series of meshes, each being a modification after a qualitative analysis of the results of the previous mesh (fig.8). The inner region was gradually increased in size until the majority of turbulent flow was within its borders. The intermediary region was then also increased in size to ensure an area of resolution surrounding the turbulence to capture any unexpected flow alterations during the solution process. Some of the higher air velocities overlapped with this region.

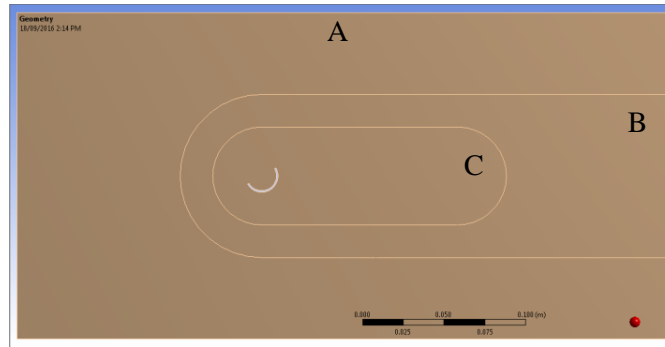


Figure 7: Domain for CFD analysis showing the 3 mesh size areas.

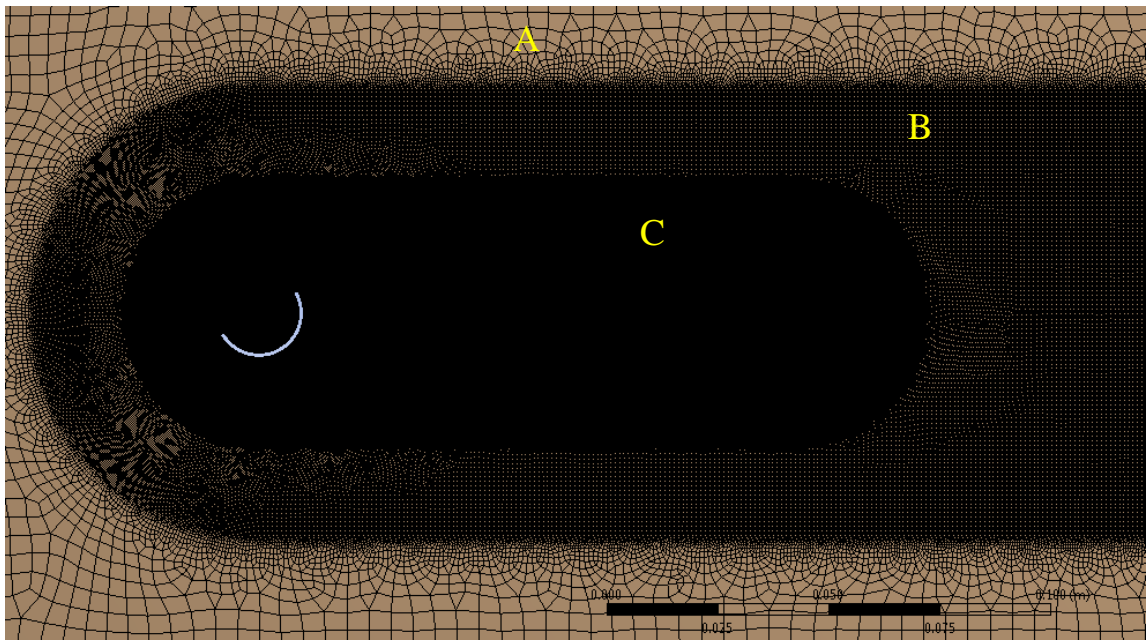


Figure 8: Meshing applied to the 3 domain regions.

Region A had the largest resolution applied to it, as the flow here had very little relevance to the region of interest around the SPD blade representation. A maximum face size of 5mm was prescribed for this region. The cell behaviour was set to soft to allow smooth adaptation between region A and region B's cell sizes. The upper and lower walls had a default edge sizing applied with a local minimum size of 5mm. The inlet boundary was located on the left-most face of region A.

Region B was an intermediary region included to allow a more gradual reduction in mesh size towards the blade. The flow in this region was expected to be less linear than region A, however as it was not in contact with the blade surface the maximum cell size was decreased to a value of 0.35mm. The right-most face of region B formed the central region of the outlet boundary.

Region C was the innermost portion of the domain, and contained the blade surfaces. As such it was given the smallest mesh size. A maximum face size of 0.15mm was used to capture as closely as reasonably possible all the flow dynamics in the air around the SPD



blade surface. The outer border of region C where it met region B was given an edge sizing constraint of 0.15mm.

The SPD blade surface located in region C was given an edge sizing constraint of 0.05mm across its entire length. This was selected after numerous meshing attempts, and seemed to give reasonable results in terms of node spacing across the rounded corners of the surface. An inflation parameter was set in region C to allow inflation of the surface cells from an initial cell thickness (normal to the surface) of 0.01mm, through a maximum of 14 layers, each with a 1.2 times growth rate. This resulted in a region of mesh modelling the boundary layer of approximately 0.8mm thickness (fig 9).

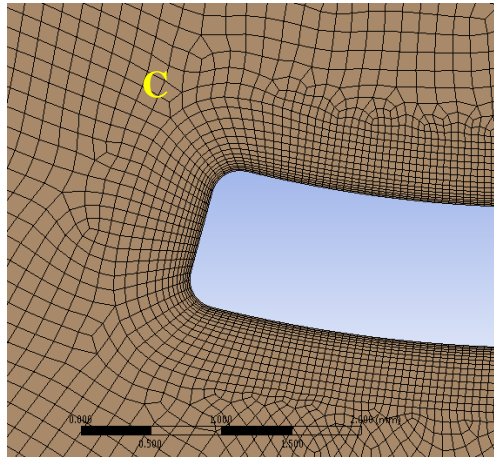


*Figure 9: Inflation of the boundary layer mesh from an initial cell thickness of 0.01mm to regional mesh size of 0.15mm (region C).*

### 3.1.3 Mesh Independency process

The grid independency study focused on region C, where higher resolution of flow characteristics was required. Force results for the SPD blade surface were used as a datum for the grid independency study. The meshing started at a maximum face size of 2mm, reducing in size until the maximum face size reached 0.15mm. At this point the mesh size was deemed accurate enough for this study.

It should be noted that the results obtained from the grid reduction process do not indicate that grid independency was actually achieved. Force results on the blade surface were still not stable, however the limits of reasonable computational time had been reached. The mesh size reduction did result in a decrease in the difference between the CFD blade force results and the wind tunnel test blade force results. This was taken to indicate that the mesh size reduction had indeed improved the accuracy of the CFD results, albeit not to the level that was sought originally.

The final meshes that resulted from the grid independency study had approximately 650,000 nodes (fig.8), depending on the actual blade arc angle and blade offset angle of each iteration. As the initial 180° CFD results had produced unusable results, only three 120° arc angle meshes were created, at 0°, 90° and 180° offset angles. These were purely to correlate the CFD results with the wind tunnel results for completeness. A total of 42 meshes were created.

### **3.1.4 Solution discovery**

The Transition SST model was used for solving the meshes generated, with all variables left at the default settings

For all solutions the boundary conditions for the analyses were set as a constant flow velocity at the inlet boundary, and a zero gauge pressure on the outlet boundary. The flow velocities determined by the wind tunnel tests were used ( $6.6\text{ms}^{-1}$ ,  $15.1\text{ms}^{-1}$  and  $20.1\text{ms}^{-1}$ ) for each mesh. This resulted in 126 solutions being calculated. For each solution the x and y direction force values on the SPD blade surface were written to a data file. A separate data file was created to contain images from the solutions.

Each solution had three images recorded from the CFD-post package on the ANSYS workbench. One showed the pressure field around the SPD blade. This was to be used qualitatively in reference to the other solutions, as well as quantitatively in reference to the static pressure recordings from the wind tunnel tests. Another image was recorded showing the predicted flow velocities around the SPD blade, to be used purely as a qualitative reference. The third image showed the pressure distribution field overlaid with the flow velocities, again purely for qualitative analysis.

## **3.2 Wind Tunnel Testing Methodology**

### **3.2.1 Tunnel Information**

The wind tunnel used for testing of the prototypes is a single pass type driven by a fixed speed electric motor connected to a centrifugal air pump. In operation the centrifugal pump draws air from its inlet adjacent to the test section of the tunnel, and expels this air through a baffle to the atmosphere. The electric motor and air pump are mounted to a sliding base that can be manually moved using a hand screw, allowing them to be moved axially in relation to the test section. This regulates an amount of air that can be drawn into the pump directly from the atmosphere instead of via the test section. The result is adjustable flow through the test section with constant electric motor speed.

The test section itself has a 310mm x 310mm square cross section, 590 mm in length. The test section walls are constructed of 10mm thick Acrylic sheets, allowing visual observation of the test section interior. A removable top wall allows modification and replacement of mounting equipment easily. The test section is fed by a fibreglass inlet housing that gradually decreases in square cross sectional area towards the test section. This, combined with two layers of wire mesh screening, provides an air flow into the test section with minimised turbulence.

The operation of the wind tunnel involves high noise levels and the possibility of harm to both operating personnel and people in the immediate vicinity. For these reasons a risk management plan was enacted to minimise any potential danger (Appendix C1).

### 3.2.2 Test Apparatus

Test forces were measured using a pivoted hollow cylindrical brass lever. One end of the tube was rigidly attached to the brass test blade using silver solder. The other end was attached to the external force testing rig through a 10mm hole in a 12mm thick marine ply board which formed the roof of the test section. This rig consisted of 3D printed components forming a central universal joint and surrounding support frame. The inner portion of the universal joint was extended to form a two part clamping structure. This structure allowed graduated rotation of the brass tube and test blade relative to the air stream, as well as the transmission of the forces to the measurement devices. The surrounding support frame included mounting points for the force measuring devices (Appendix B2).

The measuring devices were three 0g-200g jewellery scales, which gave measurements to two decimal places. With their cases cut in half to reduce their size, the load cells and measurement plates were detached and mounted to the force test rig frame. The load cells were tested against each other before the test using a nut and bolt, and some slight variation in the weights measured was noted (Appendix C2). The load cells were mounted vertically on the frame, and the measured forces were transmitted normal to their surfaces.

A Pitot tube was used for the pressure measurements. It was purchased from a hobby supplies company, and is designed for use with radio controlled aircraft. The pressure from its static and stagnation ports was transferred by the pressure probe apparatus to a Bosch BMP280 barometric pressure sensor, interfaced using an Arduino ATmega microcontroller board. The sensor output an absolute barometric pressure reading every 3 seconds, averaged over the last two readings to reduce noise. This data was recorded via a serial monitor. Two pressure readings (static and stagnation) were used to determine the airstream velocity at a point upstream of the test specimen. The static line was also used to measure the static air pressure data behind the test specimen. Pitot tube, pressure lines, breadboard with the sensors attached and microcontroller were assembled into a single unit using 3D printed components (Appendix B3). Small covers were required to cover the pressure sensors, as they are sensitive to the effects of light. The Pitot tube could be placed through the marine ply roof at various locations (Appendix C3), and when removed rubber covers would seal the slots to prevent unwanted air flow into the test section.

The Pitot tube uses Bernoulli's equation to determine the velocity of a moving air stream by comparing its static and stagnation air pressures. Bernoulli's equation is re-arranged as below to allow determination of the velocity of an incompressible fluid flow. Here we will consider data denoted with subscript 1 as the static stream values and those denoted with a subscript 2 as the stagnation values.

Bernoulli's Equation for incompressible, frictionless flow neglecting viscous effects:

$$\frac{v_1^2}{2} + g \cdot z_1 + \frac{p_1}{\rho} = \frac{v_2^2}{2} + g \cdot z_2 + \frac{p_2}{\rho}$$

From this, the second term of each side relating to difference in height can be ignored in this case, giving...

$$\frac{v_1^2}{2} + \frac{p_1}{\rho} = \frac{v_2^2}{2} + \frac{p_2}{\rho}$$

As the stagnation pressure is found when the velocity of the fluid is zero, the equation simplifies again to...

$$\frac{v_1^2}{2} + \frac{p_1}{\rho} = \frac{p_2}{\rho}$$

Next rearrange to determine the velocity of the fluid in question...

$$v_1 = \sqrt{\frac{2 * (p_2 - p_1)}{\rho}}$$

The test blade shows a maximum frontal section at 0° and 180° offset angle, totalling 1200 mm<sup>2</sup>. The test section of the wind tunnel has a total cross sectional area of 96,100 mm<sup>2</sup>. This results in a maximum blockage ratio for the wind tunnel test of approximately 1.25%. Although this does not take into account the additional frontal section of the brass tube, very little blockage effects would be expected. Therefore it was not deemed necessary for the data collected in the static blade tests to be treated with any blockage correction factors.

### 3.2.3 Testing Procedure

The purpose of the wind tunnel testing was to correlate predicted flow characteristics and resulting forces on the test blades with data predicted by the CFD model. The two test models were tested at 30° increments from 0° offset angle from the airflow to 180° offset angle. Each of these 7 angular increments was tested at 3 wind speeds. The lowest wind speed attainable for the wind tunnel was 6.6 ms<sup>-1</sup> and thus was used as the lowest test wind speed. At a wind speed of 20.1 ms<sup>-1</sup> the measuring equipment reached its maximum operating load of 200g, and thus this was used as the largest wind speed. An intermediate wind speed of 15.1 ms<sup>-1</sup> was chosen to complete the testing regime.

The wind tunnel tests performed measured two variables to compare with the CFD model. Force against the test blade was measured in both the tangential flow direction and normal to the flow in the horizontal plane, at all wind speeds and blade orientations. In addition to this the static air pressure was recorded at five different locations behind the test blade. The locations measured were on the central horizontal plane of the test section, at 0mm, 50mm and 100mm either side of the centre of the test specimen, and 30mm behind it.

The static air pressures were recorded to compare to the pressure distribution predicted by the CFD model. This was to be quantitative in the actual pressure value comparisons, as well as providing a qualitative interpretation of the pressure profile across this section of the tunnel. Unfortunately, due to the 3 dimensional nature of the flow in this region, measurement of flow velocities was deemed too difficult to attempt.

After the force measurements were taken, they were treated to give actual force values. This was necessary due to the nature of the scales, which gave data in units of grams, not newtons. The complete treatment process for a force reading was as follows...

1. Multiply the value displayed by the load cell by the gravitational constant  $9.81 \text{ ms}^{-1}$  to convert the mass to a force value as per Newton's second law  $F = m * a$ , the scales having already converted the force value to a mass interpolation.
2. Use the lever function

$$F_{arm} * x_{arm} = F_{rig} * x_{rig} \quad \text{therefore} \quad F_{arm} = \frac{F_{rig} * x_{rig}}{x_{arm}}$$

to determine the force being generated by the test blade and the brass tube it was anchored to.

3. Subtract the drag force generated by the brass tube at that wind speed (experimentally determined).
4. Divide the resulting force by the length of the test blade to give a force per millimetre value, the same as the data supplied by the Fluent CFD package.

### 3.3 Additive Manufacturing Methodology

The Additive manufacturing process began with 3D modelling of the test rig components required for testing. CREO parametric 3.0 was chosen due to its availability and the author's recent experience with its use. The individual parts of the testing apparatus that needed to be printed were identified and modelled. These individual models were then arranged into assemblies to allow printing of all parts via a single file (Appendix B4). Next, the assemblies were saved as standard tessellation files (\*.stl) and transferred to the LENS printer software. The files were smoothed to reduce the size of the tessellations, converted to machine code and then printed.

The completed components were transferred to an oven where they were heated to approximately  $60^{\circ}\text{C}$  to melt the support wax. They were then transferred to an ultrasonic oil bath to assist the removal of wax from some of the smaller galleries in the parts. Any parts that still had wax blockages in their small galleries were heated in a hot water bath to  $60^{\circ}\text{C}$  and compressed air was used to force the liquid wax out. Surfaces that would be used with adhesives, such as the Pitot tube support, were wiped clean and roughened slightly with sandpaper to ensure complete wax removal and assist adhesion. The test apparatus components were then assembled (Appendix B5).

### 3.4 MATLAB Methodology

MATLAB was used to derive predicted behaviour of novel turbines using the wind tunnel results saved in excel spreadsheets. The algorithm (Appendix D1) used this data, loaded as .csv files, and a range of user defined variables to perform the calculations. User defined data included...

- Wind speed
- Radius of turbine
- Offset range to be tested
- Offset increments to be used
- Number of blades on turbine

Two wind speeds were used for the simulations, one set at  $0.75 \text{ ms}^{-1}$  and another at  $7 \text{ ms}^{-1}$ . This was done to determine the different responses for low and high wind speeds. Similitude to a scaled prototype was not considered when choosing the test wind speeds. Two turbine radius values were used, one at 0.01m and another at 0.03 m. The purpose of these values was to analyse the different behaviours to be expected when altering the radius of a prototype turbine. The wind speeds were simulated using turbines with 3 blades.

Offset range were tested in  $15^\circ$  increments from  $-30^\circ$  through to  $45^\circ$ . Any changes in performance either side of the neutral offset could then be determined. The offset range was chosen arbitrarily based on a belief by the author that angling the open face of the blade towards the axis of revolution would be more beneficial, hence the slight bias in this direction.

Turbines with 3 blades were tested as well as turbines with 5 blades. This was done to assess the effect of altering the number of blades with respect to turbine performance. Both of these simulations were performed at both trial wind speeds. The results from each turbine were analysed with respect to each other at each wind speed, as well as between the same turbine designs at the different wind speeds.

Other variables were common to all simulations, and as such were not considered to be user defined as such. These included...

- Blade type ( $180^\circ$  and  $120^\circ$  arc)
- Duration of simulation
- Time step of simulation
- Rotational inertia of turbine

The time step used for the simulations was determined after considering the time that the simulations would require to run, the amount of memory of the computer used to run the simulations, and the accuracy of the results determined by the simulation. After several trials a time step of 0.0002 seconds was determined to give results that seemed reasonably stable, and kept computational time to a reasonable level. Duration of each simulation was limited to 40 seconds, at which point most of the results had become relatively stable.

Each simulation that was run gave the following data sets.

Time\_data\_1

- Incremental time step values for  $180^\circ$  blade
- $180^\circ$  blade angular acceleration at each time step
- $180^\circ$  blade angular velocity at each time step
- $180^\circ$  blade tip speed at each time step

Time\_data\_2

- Incremental time step values for  $120^\circ$  blade
- $120^\circ$  blade angular acceleration at each time step
- $120^\circ$  blade angular velocity at each time step
- $120^\circ$  blade tip speed at each time step

The rotational inertia value used was aimed at a likely value for a wind tunnel prototype. The design was idealized as a simplified hoop mass, with a mass of 200g, radius to the centre of mass 0.02m. Using the formula for rotational inertia of a hoop mass

$$I = m * r^2 = 0.2 * 0.02^2 = 0.00008 \text{ kgm}^2$$

The mass of 200g was included to allow more accurate data to be gathered during any tests. The higher rotational inertia would decrease the angular acceleration of a turbine, thus allowing an observer to gather more data on torque generated by the turbine at sequential rotational velocities starting from rest.

## 4. Results

### 4.1.1 CFD results

From the solutions to the CFD analyses performed, force values on the turbine blade surface were determined by the ANSYS software. This was recorded in the form of x and y vector components of the net surface forces on the model (APPENDIX E1), x being parallel to the fluid stream direction, y being normal to the fluid stream direction, in the 2D model. The force values were given in units of  $\text{Nmm}^{-1}$ , indicating a total force exerted on an extruded surface formed by the blade section modelled, per mm of extrusion. These data points were compared to the analogous wind tunnel test data.

The CFD data points were not correlated by the wind tunnel force data through the entire range of angles tested. The force vectors of the CFD predictions in the x direction all showed a maximum value at  $30^\circ$ , and a smaller maxima at  $120^\circ$  offset angle (fig.10). The force data points in the y direction were erratic, with multiple maxima in the positive and negative tenses (fig.11).

The x direction forces predicted by the CFD analysis had a maximum deviation from the wind tunnel data at  $30^\circ$  rotation, over predicting the force by 312% in the  $20.1 \text{ ms}^{-1}$  analysis. The second major deviation at  $135^\circ$  rotation over predicted the force by 174%. This pattern was observed for all three wind speeds analysed.

The y direction forces predicted by the CFD analysis showed erratic over prediction of the magnitude of forces measured in the wind tunnel tests. The maximum deviation was  $5.7 \text{ Nmm}^{-1}$  in the  $20.1 \text{ ms}^{-1}$  analysis of the  $150^\circ$  rotation mesh. As with the x direction CFD data, the CFD data followed the same trend over the three wind speeds analysed.



## X direction forces: Wind tunnel data vs CFD predictions (180° arc)

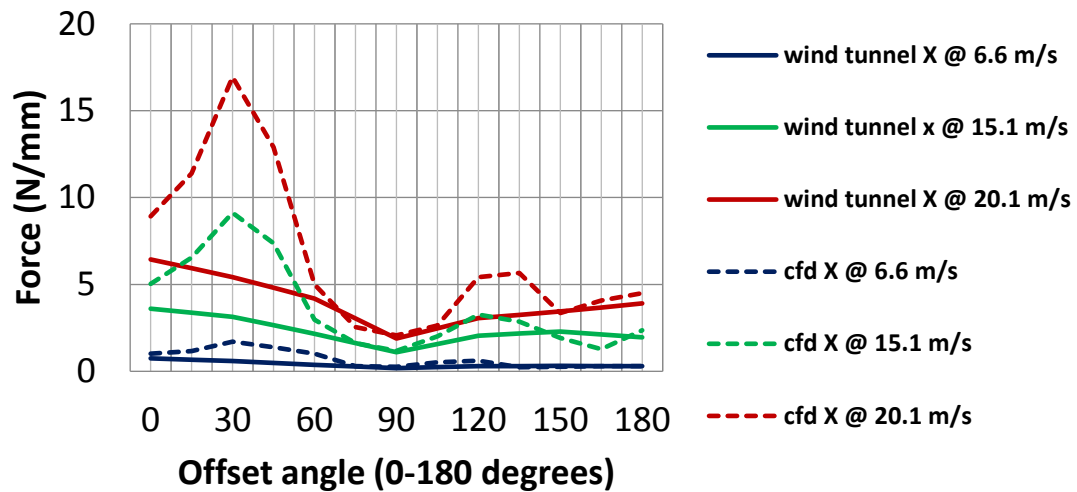


Figure 10: Comparison of x direction force results from the CFD analysis with wind tunnel data (CFD dashed lines, wind tunnel solid lines) at the tested wind speeds of  $6.6 \text{ ms}^{-1}$ ,  $15.1 \text{ ms}^{-1}$  and  $20.1 \text{ ms}^{-1}$ .

## Y direction force: Wind tunnel data vs CFD predictions (180° arc)

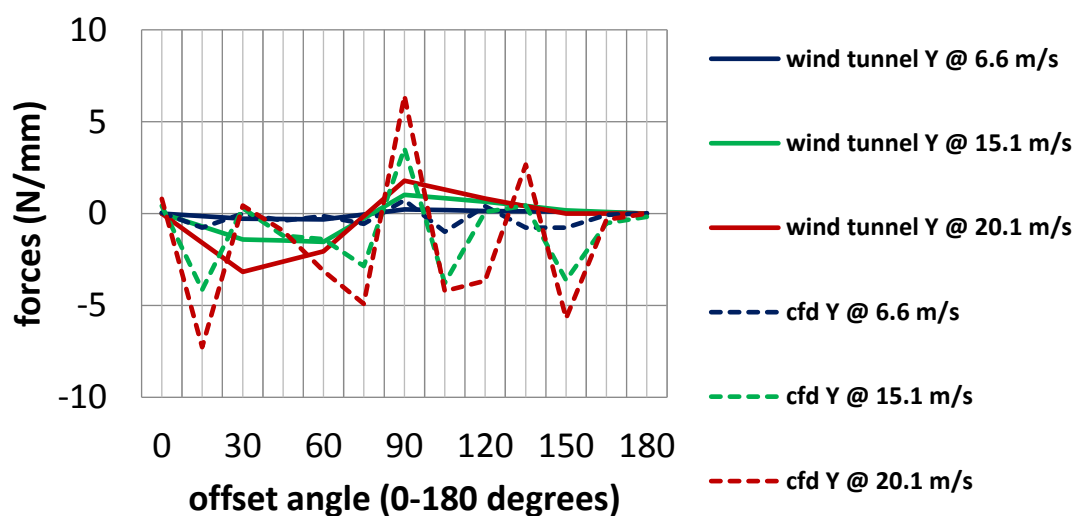


Figure 11: Comparison of the y direction force results from the CFD analysis with wind tunnel data (CFD dashed lines, wind tunnel solid lines) at the tested wind speeds of  $6.6 \text{ ms}^{-1}$ ,  $15.1 \text{ ms}^{-1}$  and  $20.1 \text{ ms}^{-1}$ .

After the comparison of these unexpected results from the CFD analysis, further research was conducted. Discussion with peers revealed that use of a steady state model for the ANSYS solution may have resulted in the large deviations observed. It was suggested to the author that use of a transient solution was probably warranted. A targeted literature review into ANSYS methodology used in similar research found agreeable results.

In the course of research in Darrieus Turbine modelling (Lanzafame et al. 2014), it was determined that the use of a transient solution was required for accurate results. This same study also found that a PISO (Pressure Implicit with Splitting of Operators) solution approach gave better accuracy, and that calibration of the Transition SST variables for the turbulence model was necessary. Using this approach the authors found a good correlation between CFD and experimental data.

A second attempt at CFD analysis was conducted using this information as a guideline. The domain of a 2D CFD analysis was meshed for a 180° arc blade at an offset of 30°. The face of the domain was split into three zones (Appendix E2), the smallest one surrounding the blade, an intermediate one surrounding the first and the third representing the remainder of the domain. The innermost zone (A) of the mesh surrounding the blade was given a maximum face size of 0.10 mm, the intermediate zone (B) a maximum face size of 0.35 mm, and the outer zone (C) a maximum face size of 7 mm. A triangular mesh was used for all three zones (Appendix E3). An inflation was applied to the mesh on the surface of the blade to capture the boundary layer flow Appendix D4).

The inlet condition for the analysis was set as a 20.1 ms<sup>-1</sup> flow velocity, with a zero gauge pressure outlet condition. The PISO scheme was used and a transient time step of 0.02 seconds was applied over a series of 50 time steps (Appendix E5). The resulting analysis required approximately 4 hours to solve. The force results indicated the same 16.3 Nmm<sup>-1</sup> in the x direction, and 16.2 Nmm<sup>-1</sup> force in the negative y direction, an even larger deviation from the wind tunnel data acquired. The flow showed some similarity with the original solution (Appendix E6), however the trailing vortex was detached from the blade surface (Appendix E7), with several regions of turbulent kinetic vortices (Appendix E8).

#### **4.1.2 CFD Results Discussion**

The CFD results obtained are of no use in modelling due to their large deviation from physical test data for the same system. The erratic nature of the y force data in particular would likely lead to spurious results in any MATLAB model. The poor data may have been due to one of several causes, poor meshing, poor numerical model selection, or boundary posing problems.

While a mesh independency study was attempted for the initial CFD models, it was not completed due to restriction of computational power and time constraints. To determine the independency of a mesh used for analysis it would be necessary to iteratively reduce the node sizing of a mesh, use the solver to determine a solution, and compare a monitor value such as surface force. At the point of mesh independency the difference in the monitored value results between mesh iterations would be negligible. For this study the force results were still irregular at the time of maximum mesh node number being reached.

Mesh quality was also an issue with the CFD analyses conducted. Orthogonal quality varied between meshes, as did average skewness values of the cells within the mesh.

Unfortunately the author was not sufficiently skilled in the use of the software to be able to fix this problem. While the meshes were not of a terrible quality, improvement of meshes would most probably improve the accuracy of the results obtained, as well as reduce time required to reach a convergent solution.

The numerical model selected (RANS with Transition SST turbulence model) has been used with good results in other studies. While best practice is to tailor the equations by setting the variable values such as turbulence intensity and dissipation rates for each system studied, this process was not followed in the present study due to time constraints. It is quite possible that some of the error obtained between the wind tunnel test data and CFD data was due to this. Additionally, the values for wall  $y^+$  values was not determined in the numerical models. Again the reason for this was time constraints relating to the number of meshes studied. Checking that  $y^+$  values of less than 1 were shown in the solutions would help ensure accurate representation of boundary layer flow (Tu 2013). As with the numerical model selected, the boundary conditions chosen have been used effectively in previous studies.

There is an inherent problem with using 2D analyses in comparison with wind tunnel testing, in that 2D numerical simulations cannot account for flow in the 3<sup>rd</sup> dimension, in this case end flow around the top and bottom of the test specimens. It is probable that some of the difference noted between the experimental and numerical data found in this study can be traced to this problem. Using a 3D analysis of the system would be preferable, however the increase in computational cost was not affordable for the number of simulations required in this study, in the time frame and that was available.

Despite these problems, there was much to be learned from the CFD results. Possible location and intensity of turbulent vortices was shown, describing the nature of the flow around the test specimens throughout their rotation. This was useful in determining possible reasons for some of the unexpected wind tunnel results. For example, the favourable ratio of forces for the 180° test blade at 0° and 180° orientations seems to be caused by the formation of more compact vortices behind the 180° blade compared to the 120° blade (fig.12,13). This seems to indicate a relatively higher pressure on the trailing surface of the 180° blade, less affected by the low pressures in the vortices. This in turn results in a smaller pressure difference across the blade.

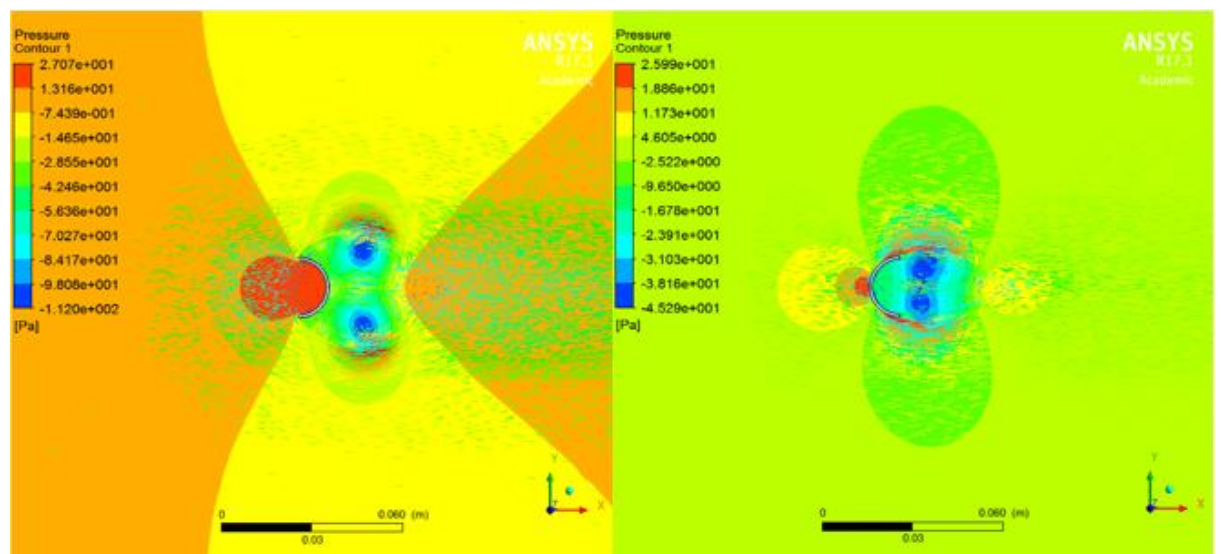


Figure 12: Pressure fields and velocity vectors for the 180° blade at 0° offset and 180° offset angles.

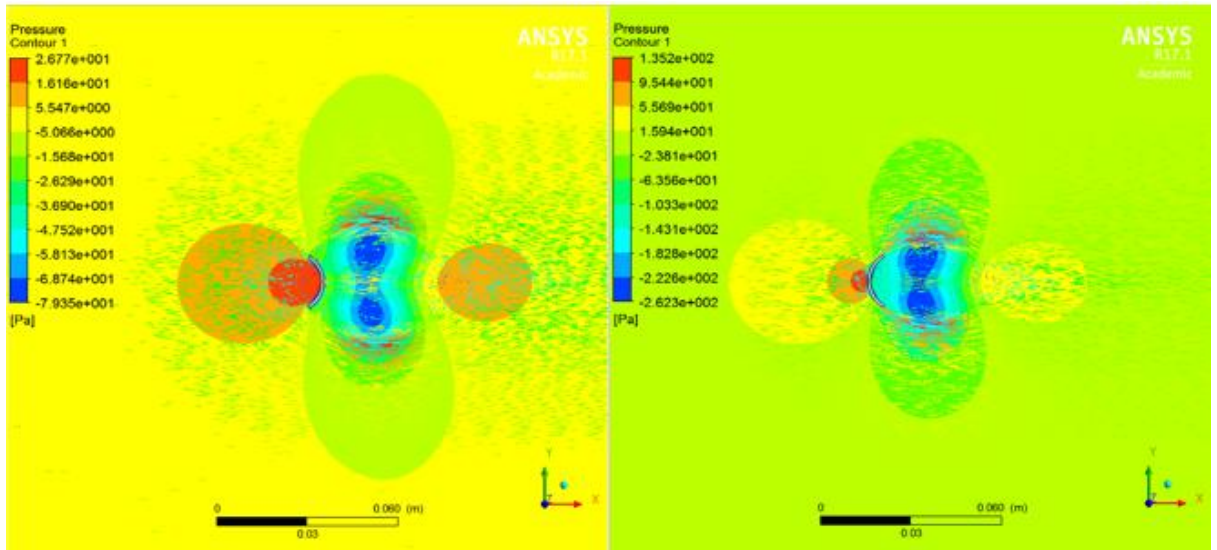


Figure 13: Pressure fields and velocity vectors for the 120° blade at 0° offset and 180° offset angles.

The CFD results also show that during the portion of rotation where the predicted forces spiked above the experimental force results, turbulent vortices were forming much closer to the trailing surface of the blades (fig.14). The impact of vortex generation closer to the surface of the blade is to introduce lower pressures against the blade surface, resulting in a higher pressure difference across the blade. While there are obviously some problems with the forces predicted, this may be due to the transient nature of the vortex generation and detachment process, and the lack of the steady state solution being able to track this feature of the flow. It would be helpful to track this process with a transient analysis, and compare it with experimental observations of the flow field behind a similar blade over a period of time. This procedure has been used in many previous studies, for example using Particle Imaging Velocimetry (PIV) techniques (Dobrev & Massouh 2011). One feature that was not witnessed in any of the CFD renders was evidence of significant lift effects, with flow separation in all cases.

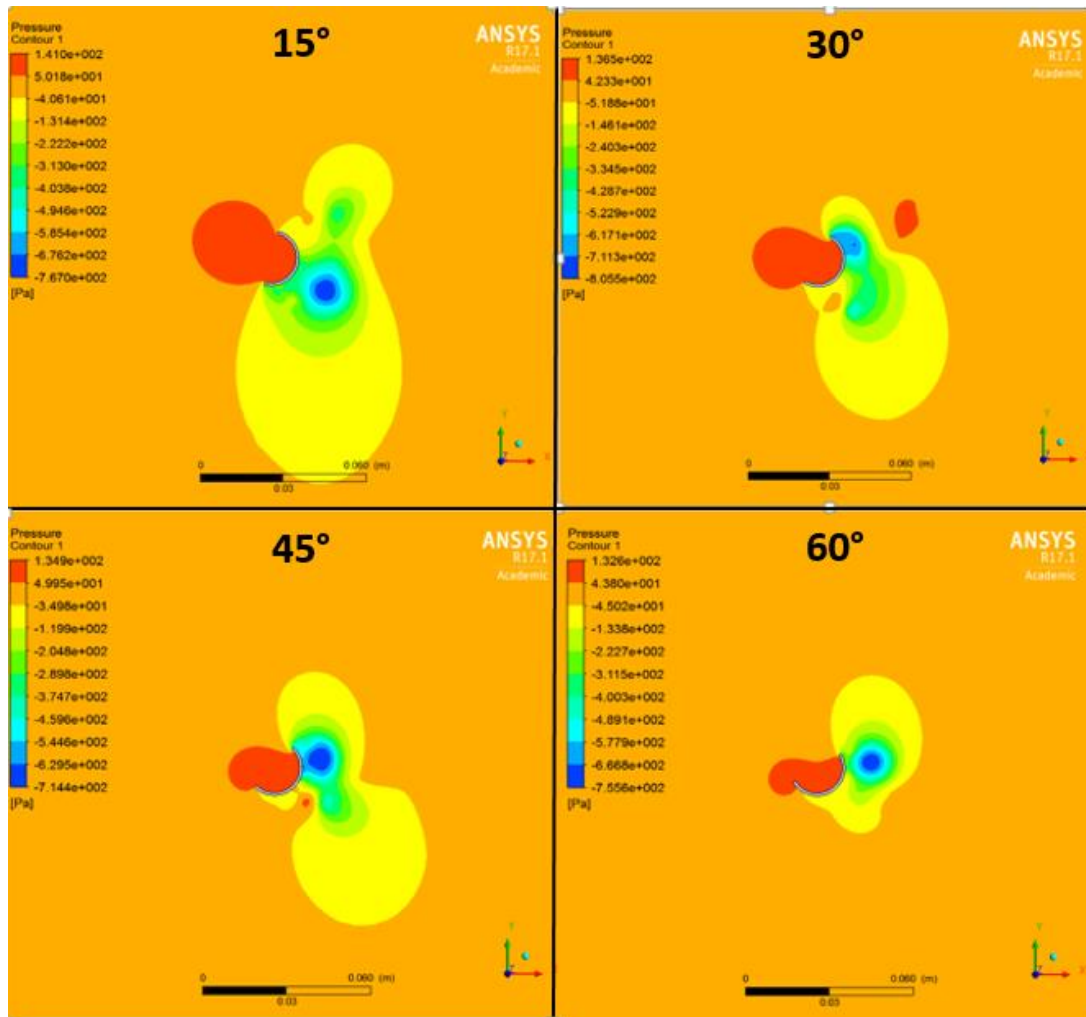


Figure 14: Pressure fields around a 180° blade from 15° offset to 60° offset angle. At 30° and 45° vortex flow is closer to the trailing surface of the blade.

#### 4.2.1 Wind Tunnel Results

The results of the wind tunnel testing of the two test specimens were collated into a spreadsheet (APPENDIX F1). The results were interpolated over a full revolution using the principal of symmetry, recognizing that y direction forces should be equal in magnitude and opposite in tense for the second half of a full revolution. Comparisons between the x direction forces (fig.15), y direction forces (fig. 16), and net force results (fig.17) are presented. The analysis of the pressure distribution of the flow behind the test specimens was not considered after it was discovered that the region tested was too distant from the test specimen to be of any use in correlating the CFD data.

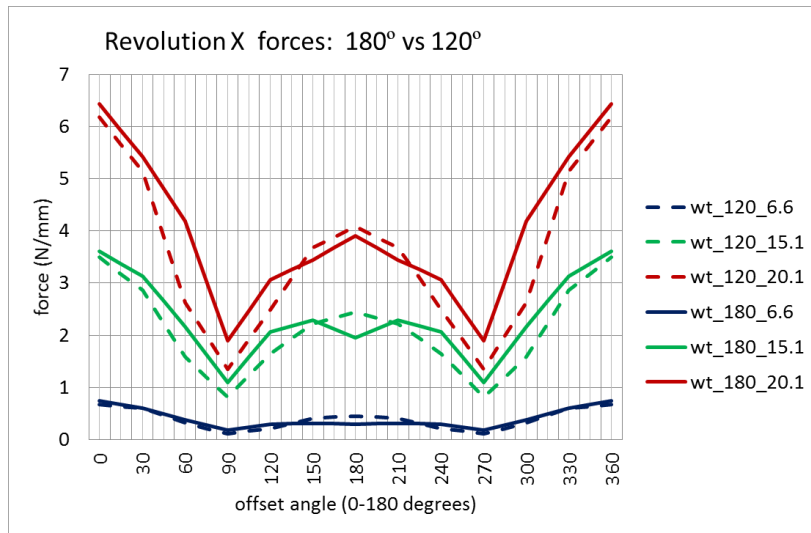


Figure 15: Plot of x direction forces from wind tunnel data interpolated over a full revolution (180° arc solid line, 120° arc dashed line) at the tested wind speeds of  $6.6 \text{ ms}^{-1}$ ,  $15.1 \text{ ms}^{-1}$  and  $20.1 \text{ ms}^{-1}$ .

The highest forces experienced in the x direction during the wind tunnel tests were on the 180° specimen at 0° offset angle from the flow. A second maxima was experienced at 180° offset angle. The minima for x direction forces was at 90° offset. The 180° arc blade experienced higher x direction forces over most of the revolution, except for the region of approximately 25° either side of the 180° offset angle. Here the 180° arc specimen experienced slightly lower x direction forces than the 120° arc section. These trends were common across all three wind speeds tested.

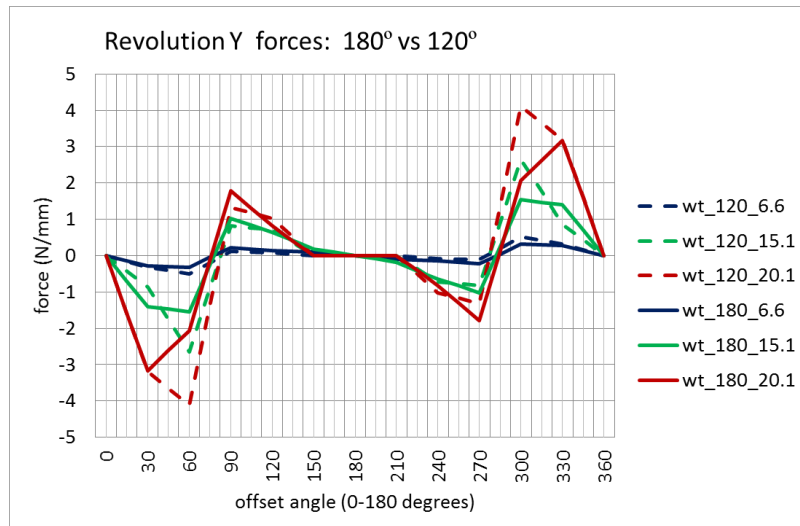


Figure 16: Plot of y direction forces from wind tunnel data interpolated over a full revolution (180° arc solid line, 120° arc dashed line) at the tested wind speeds of  $6.6 \text{ ms}^{-1}$ ,  $15.1 \text{ ms}^{-1}$  and  $20.1 \text{ ms}^{-1}$ .

The y direction forces experienced by the two test specimens showed some variance in their magnitude and location. For the  $20.1 \text{ ms}^{-1}$  wind speed test the 180° arc specimen

had a maximum magnitude in the negative tense at 30° offset, and a second maxima of smaller magnitude in the positive tense at 90° offset. At the same wind speed the 120° arc specimen had a maxima in the negative tense at 60° offset, and a smaller maxima in the positive tense at 90° offset.

The maximum magnitude of force experienced in the negative y direction was larger in the 120 arc specimen than in the 180 arc specimen across the three wind speeds. Additionally the second maxima in the positive direction at 90° offset was smaller in the 120° arc specimens compared to the 180° arc specimens. As expected, no y direction forces were experienced at 0° and 180° offset.

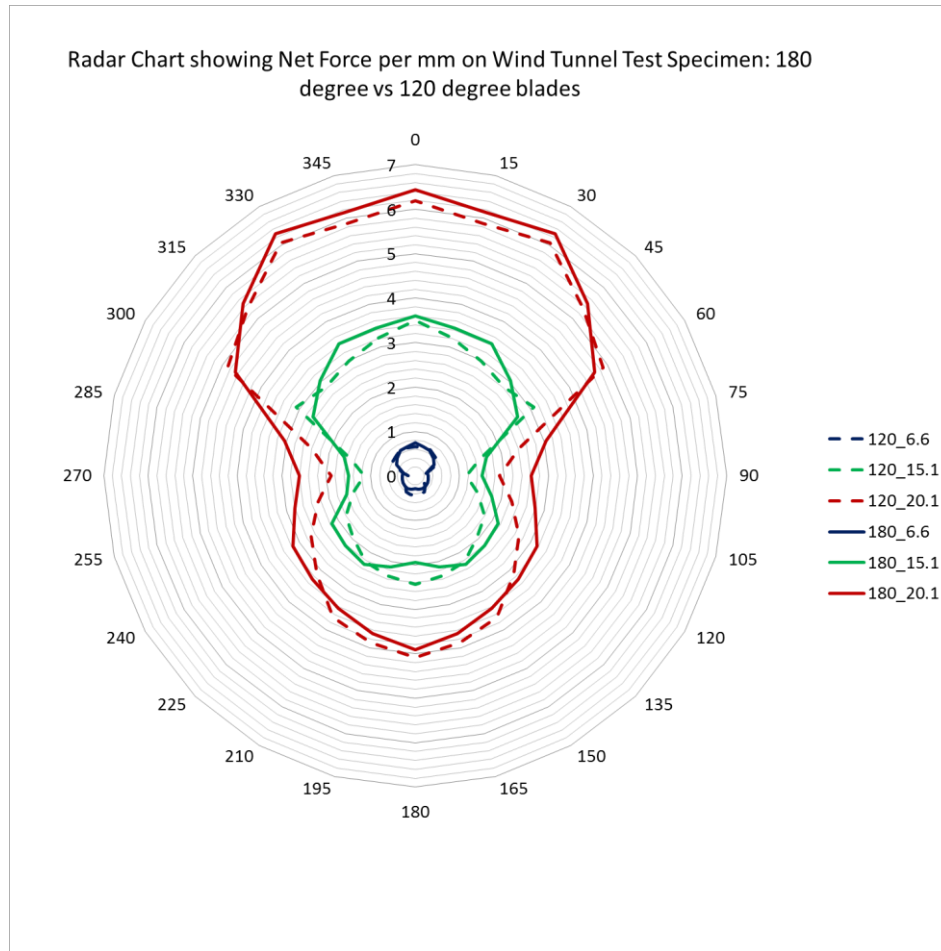


Figure 17: Radar plot of the net force results from wind tunnel testing (180° arc solid line, 120° arc dashed line), interpolated over a full 360° revolution, at the tested wind speeds of 6.6 ms<sup>-1</sup>, 15.1 ms<sup>-1</sup> and 20.1 ms<sup>-1</sup>.

The net magnitude of forces on the two specimens showed some overlap throughout an interpolated full revolution. While the 180° arc specimen experienced a higher net force over most of the revolution, at approximately 60° either side of 0° offset, and over the range of 135°-225° offset, the 120° arc specimen experienced slightly higher net forces, by approximately 0.3 Nmm<sup>-1</sup>.



## 4.2.2 Wind Tunnel Results Discussion

There was some interesting information contained within the results of the wind tunnel tests. It was found that the 180° arc blade gave a higher tangential force in the downwind direction, with a similar resistive force to 120° arc blade in the upwind direction. The forces normal to tangential path of the blade were also different between the two blades specimens, with the 120° blade producing a higher magnitude of y direction force compared to the 180° arc blade during the initial 30° to 90° rotation angles.

If the forces generated in the tangential direction when the blade is directly facing towards and away from the oncoming air stream are considered in isolation, the 180° arc blade is clearly more preferable. It will generate higher torque during the downwind portion of the blades revolution, with an equal resistive torque to the 120° blade during the advancing portion of the revolution. However, when considering the normal forces generated by the blades, it is possible that the 120° blade may generate more useful torque during the period of rotation between 90° and 180° of the revolution. This is investigated in the MATLAB model.

There are some limitations to the data delivered by the wind tunnel tests. The test specimens had no end plates, and as such air flow around the ends of the specimens was present. This limits the usefulness of the data to numerical modelling of turbines with the same relative blade dimensions. To use the wind tunnel data for blades of different lengths, specimens would need to be tested that did not allow end flow. Alternatively, research would need to be conducted to ascertain what amount of end flow was present in different blade configurations at different offset angles and different wind speeds. Testing blades that did not allow end flow would probably be more useful, as this mimics the way in which the SPD blades would most likely be used in a hybrid VAWT configuration.

The force measurements recorded had a significant error present due to fluctuating readings from the load cells used on the test apparatus. Deviations of approximately  $\pm 0.5g$  were noted during the testing procedure. There are several reasons that this may have occurred. Firstly, the generation and separation of vortices about the surface of the test specimens would have resulted in fluctuating forces on the specimens. Secondly, the method used to transfer surface forces on the specimens to the load cells, a lever arm about a universal joint, offered an opportunity for oscillations in the test apparatus to occur. Having the test specimen secured above and below the test section would likely reduce the effect these oscillations would have on the data recording.

Additionally, the digital readout of the forces on the load cells was not continuous, and readings were displayed only several times a second. Having a higher frequency of readings, perhaps as a digital file of continuous readings, would have allowed the data to be analysed more accurately. As it was, the author had to estimate an average for each measurement mentally by watching the digital display for several seconds. Data recordings above the Nyquist rate for the system would be more reliable.

The Pitot tube measurements the pressure distribution behind the test specimen were not as useful as hoped, due to poor positioning in the flow (Appendix C4). As the wind tunnel tests were performed before useful CFD data was available, the Pitot tube measurements were inadvertently taken in regions of flow that did not reflect the turbulent regions of the flow (fig.18). The pressure readings taken instead measure regions of flow that while affected by the test specimen, do not help to correlate the CFD



estimation of the turbulent flow around the trailing surface of the specimen. Availability of CFD results would have allowed a more useful selection of measurement points.

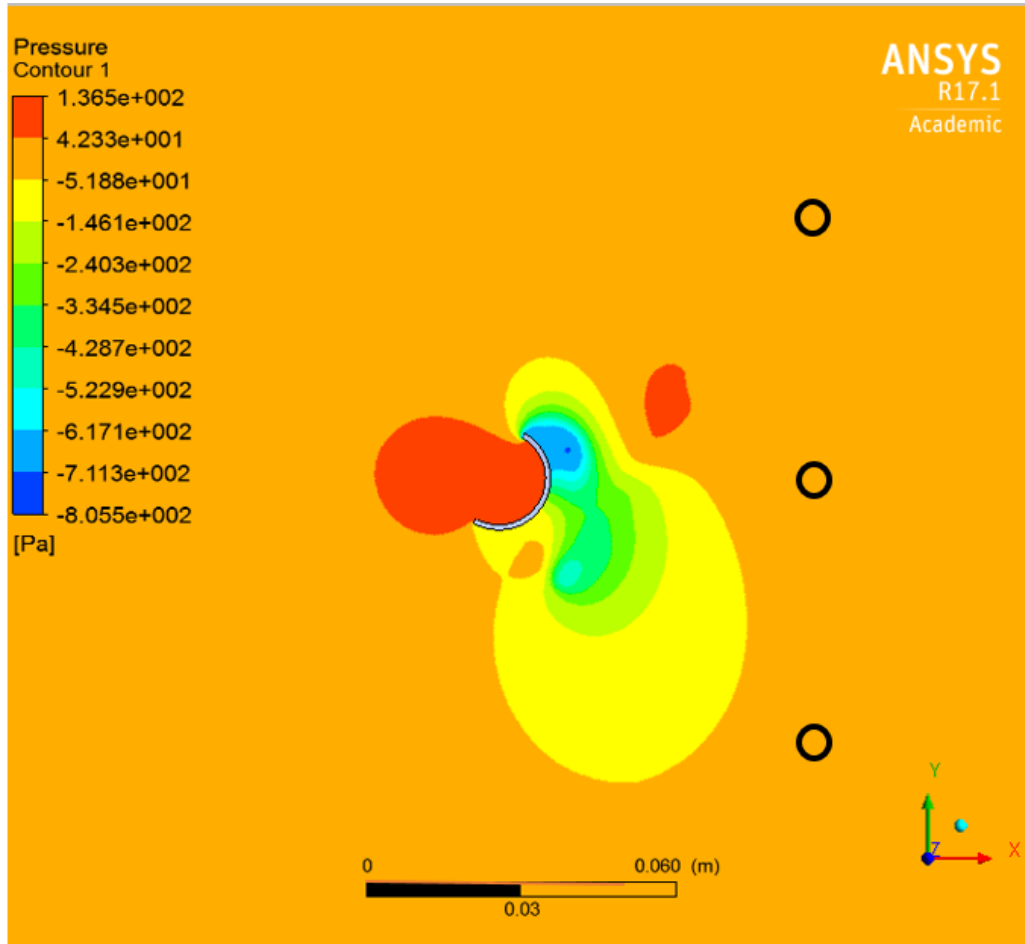


Figure 18: Sample ANSYS fluent solution showing approximate locations of the inner three static pressure readings taken by the Pitot tube (black circles).

### 4.2.3 Dimensionless Analysis

For the purpose of conducting of similitudinous comparisons, the data obtained from the wind tunnel testing is presented as a plot of dimensionless parameters. Using the pressure and temperature data acquired at the time of the experiment as recorded by the BMP280 sensors, the density and viscosity of the air were determined. This, in conjunction with the dimensions of the blade and flow velocity allowed the Reynold's number and Coefficients of lift and drag to be determined for each of the wind speeds, for each blade type and offset angle, using the formulae...

$$Re = \frac{\rho * V * D}{\mu}$$

$$C_D = \frac{F_D}{\frac{1}{2} * \rho * V^2 * A}$$

$$C_L = \frac{F_L}{\frac{1}{2} * \rho * V^2 * A}$$

These operations were performed in an EXCEL spread sheet (Appendix F2), allowing the results to be plotted against one another (Appendix F3). The coefficient of drag for the two blades had a maxima at 0° offset, minima at 90° and 270°, and a second minor maxima at 180° offset (fig.19), the largest being that of the 180° blade. The greatest coefficient of lift produced was for the 120° blade, at 60° and 300° offset (fig.20).

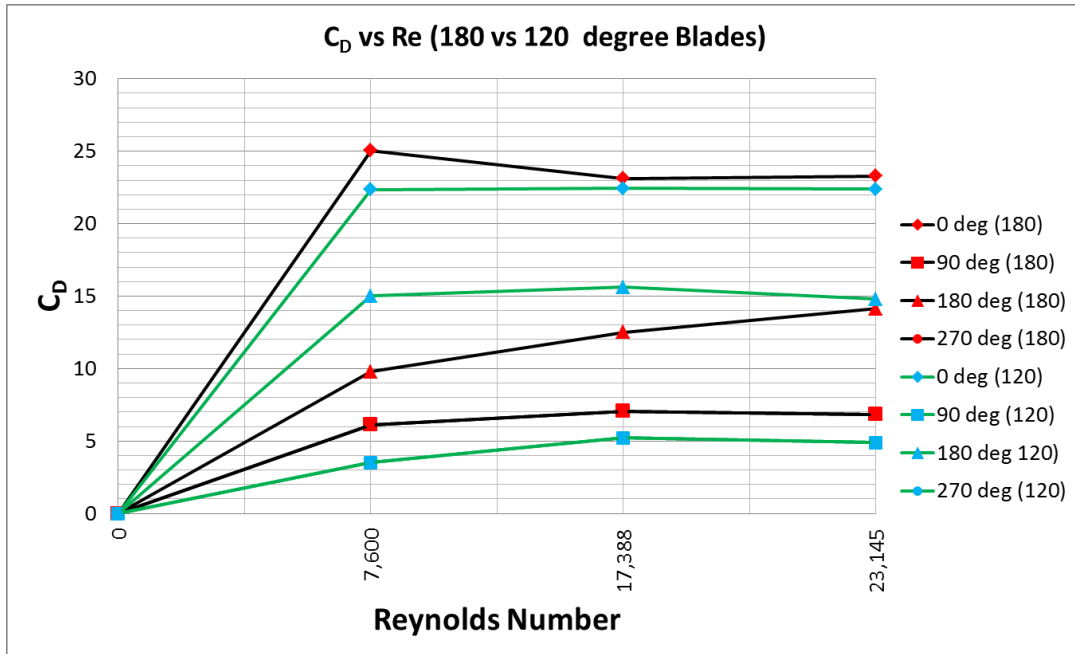


Figure 19: Plot of  $C_D$  vs Re for (180° and 120°) blades at their maxima and minima  $C_D$  angles

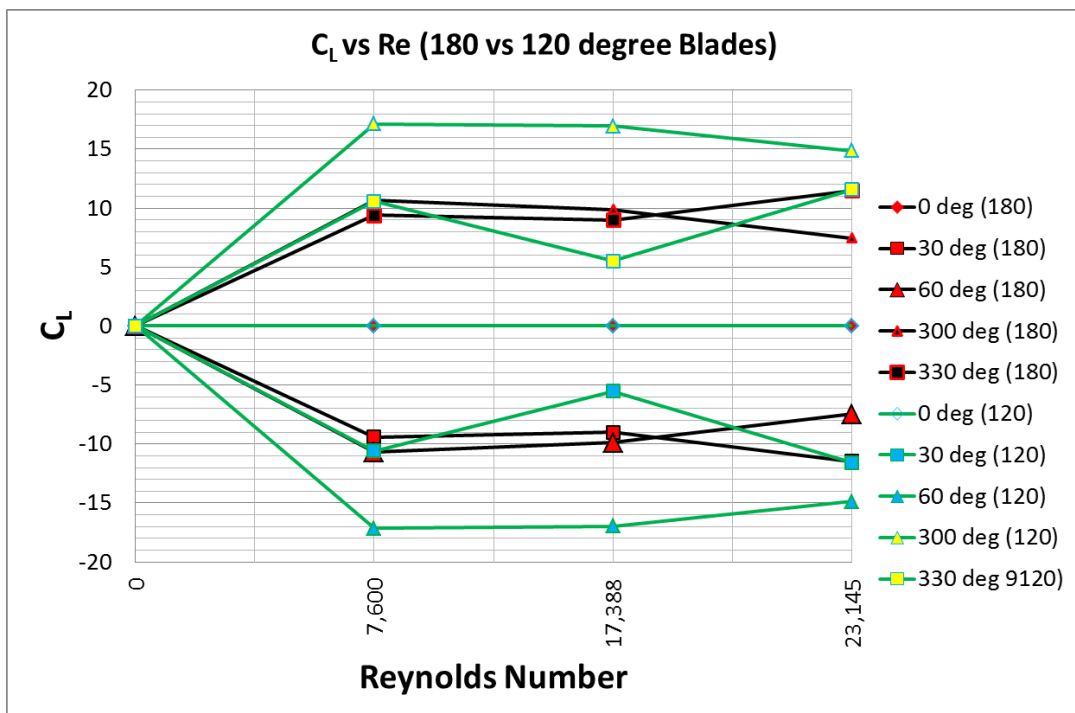


Figure 20: Plot of  $C_L$  vs Re for (180° and 120°) blades at their maxima and minima  $C_L$  angles.

It can be seen from the plots of dimensionless parameters that the 120 blade gave a significantly increased maximum coefficient of lift compared to the 180 blade. This was despite the separation of flow from the blade surface at these angles.

## 4.3 MATLAB Results

### 4.3.1 Arc angle comparison

At the lower wind speed of  $0.75 \text{ ms}^{-1}$  the  $180^\circ$  blade accelerated to approximately  $44 \text{ rads}^{-1}$  over the duration of the simulation, while the  $120^\circ$  blade accelerated to approximately  $37 \text{ rads}^{-1}$  (fig.21). The  $180^\circ$  blade reached top speed in approximately 18s, while the  $120^\circ$  blade took the entire 40s to reach its top speed.

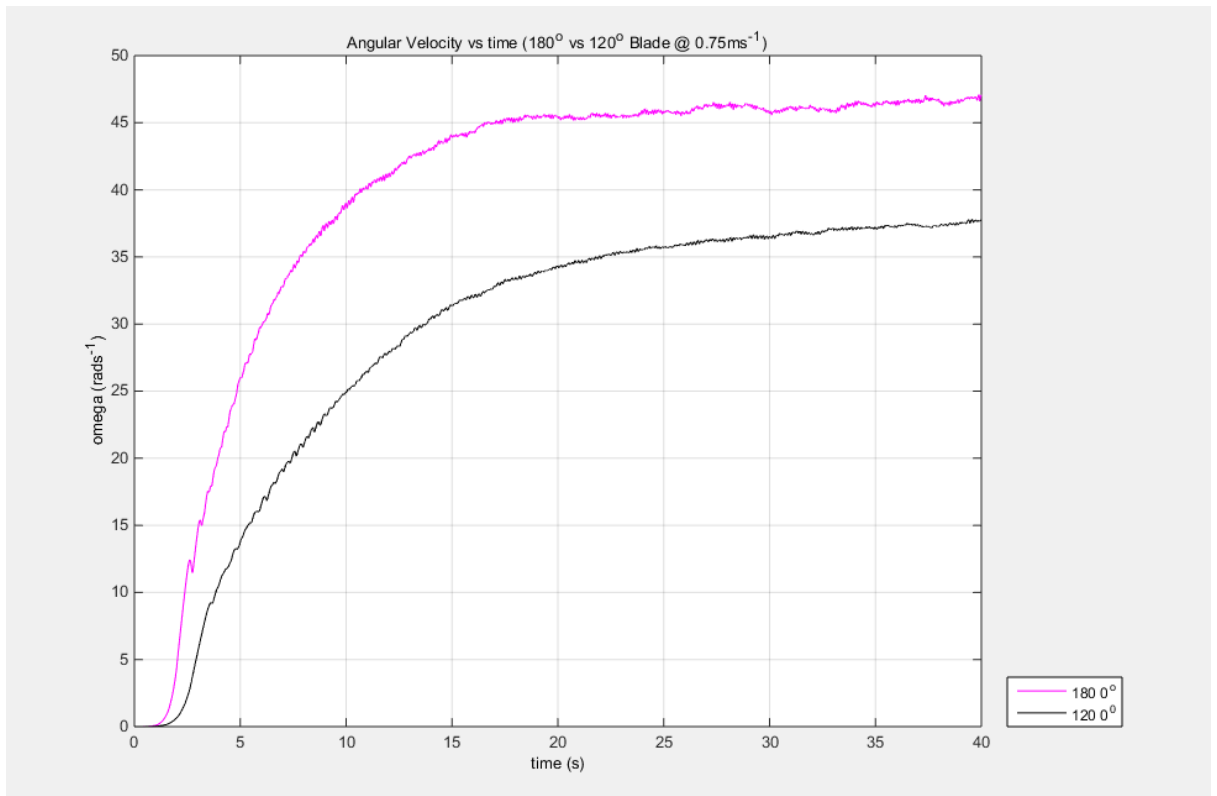


Figure 21: Angular velocity of  $180^\circ$  and  $120^\circ$  arc blades in  $0.75 \text{ ms}^{-1}$  wind speed ( $0^\circ$  offset data used for comparison).

At the higher wind speed of  $7\text{ms}^{-1}$  the  $180^\circ$  blade accelerated to a maximum angular velocity of approximately  $106\text{ rads}^{-1}$  in 25 seconds, where the  $120^\circ$  blade accelerated to a maximum angular velocity of approximately  $122\text{ rads}^{-1}$  in 40 seconds, with this turbine still showing some slight acceleration (fig.22). More complete data can be found in (Appendix D2).

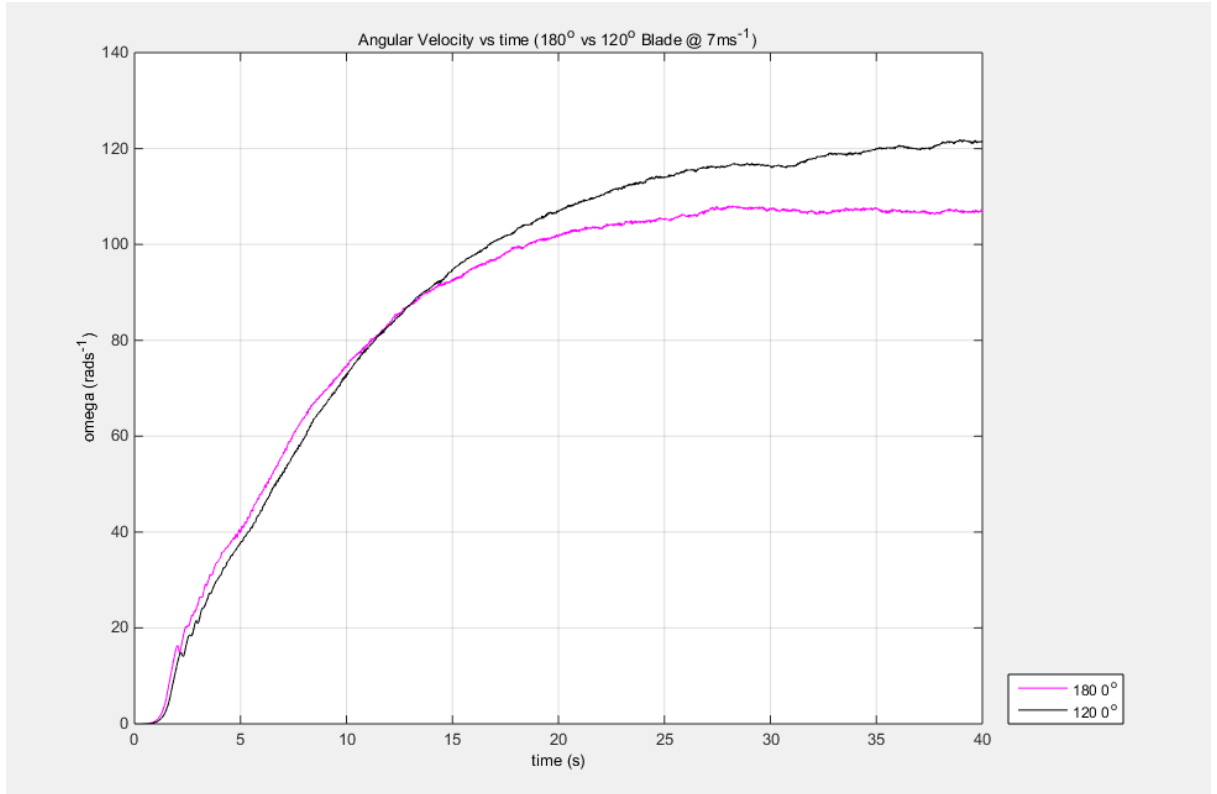


Figure 22: Angular velocity of  $180^\circ$  and  $120^\circ$  arc blades in  $7.0\text{ ms}^{-1}$  wind speed ( $0^\circ$  offset data used for comparison).

### 4.3.2 Offset comparison

Most simulations showed similar results to the alteration of the blade offset amount, in that only a small amount of change in performance was noted over the range of offsets (Appendix F3.1 and F4.1). However for the  $0.75\text{ms}^{-1}$  wind speed on the  $180^\circ$  blade, the  $-30^\circ$  and  $-15^\circ$  offsets yielded an anomaly where the turbine initially rotated backwards, and then settled into a gradually diminishing oscillation about the origin (fig.23).

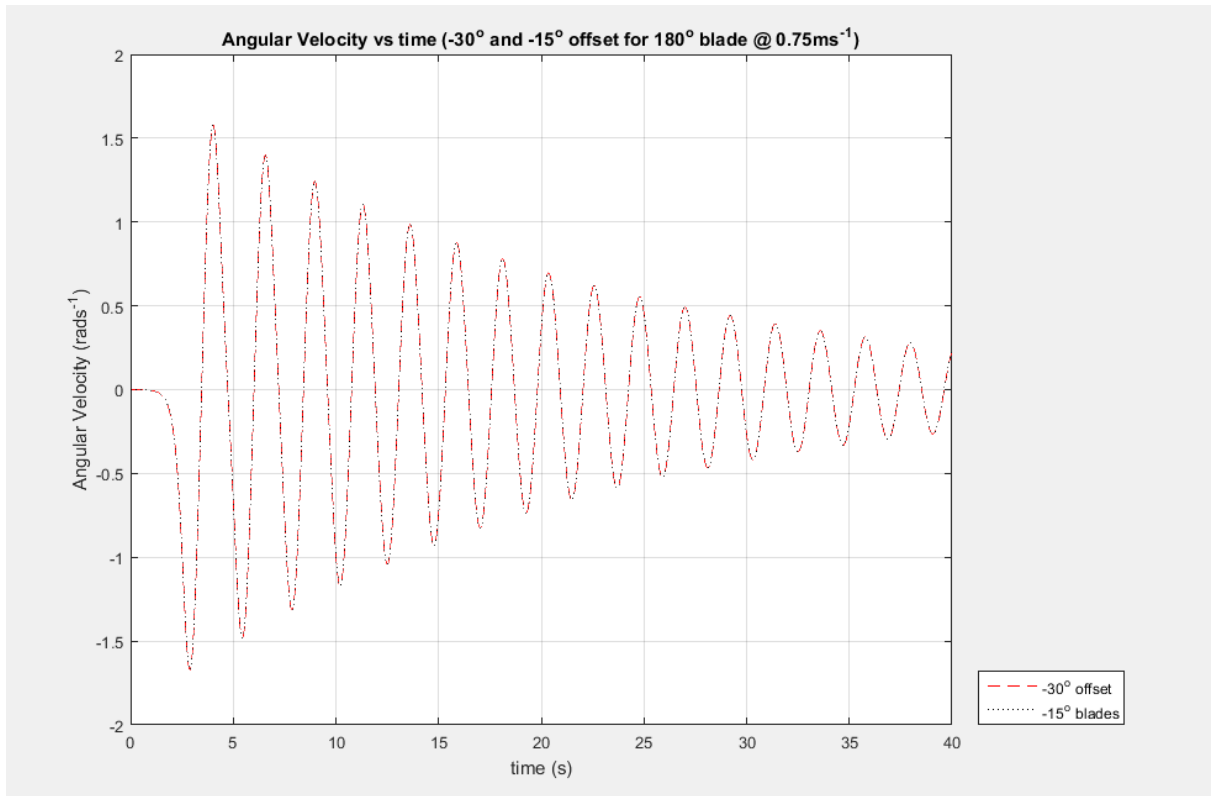


Figure 23: Rotational anomaly for  $180^\circ$  blade in  $0.75\text{ms}^{-1}$  wind at  $-15^\circ$  and  $-30^\circ$  offset.

### 4.3.3 Turbine Radius Comparison

At both wind speeds and for both blade arcs the effect of increasing the turbine radius was similar (Appendix F2.3). The turbine with the larger radius would accelerate faster, and reach a peak rotational velocity sooner. However, the peak rotational velocity was greatly diminished in the turbine with the larger radius (fig.24).

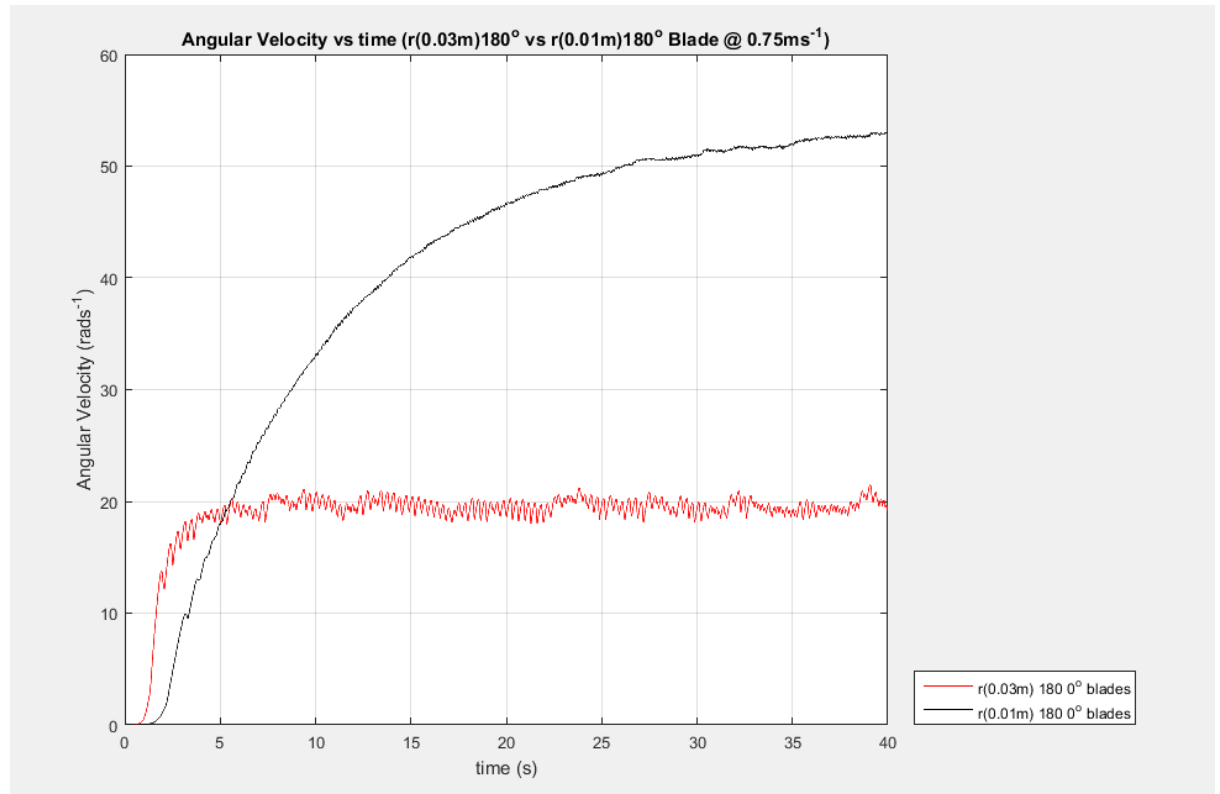


Figure 24: Comparison of rotational velocity for a three 180° bladed turbine in  $0.75 \text{ ms}^{-1}$  wind, showing both 0.03 m radius and a 0.01 m radius geometry.

### 4.3.4 Blade Number Comparison

The results for the analysis of 3 bladed turbines against 5 bladed turbines showed some interesting results (See Appendix F2.2). The 5 bladed turbines accelerated faster and reached their peak angular velocity in a faster time. The 3 bladed turbines, however, continued accelerating for a longer time, reaching peak rotational velocities higher than the 5 bladed turbines. For example in the 180° turbine at  $0.75 \text{ ms}^{-1}$  wind speed, the 5 bladed turbine reached a peak angular velocity of approximately  $45 \text{ rads}^{-1}$  in 18 seconds, while the 3 bladed turbine was still accelerating at 40 seconds past  $53 \text{ rads}^{-1}$  (fig.25).

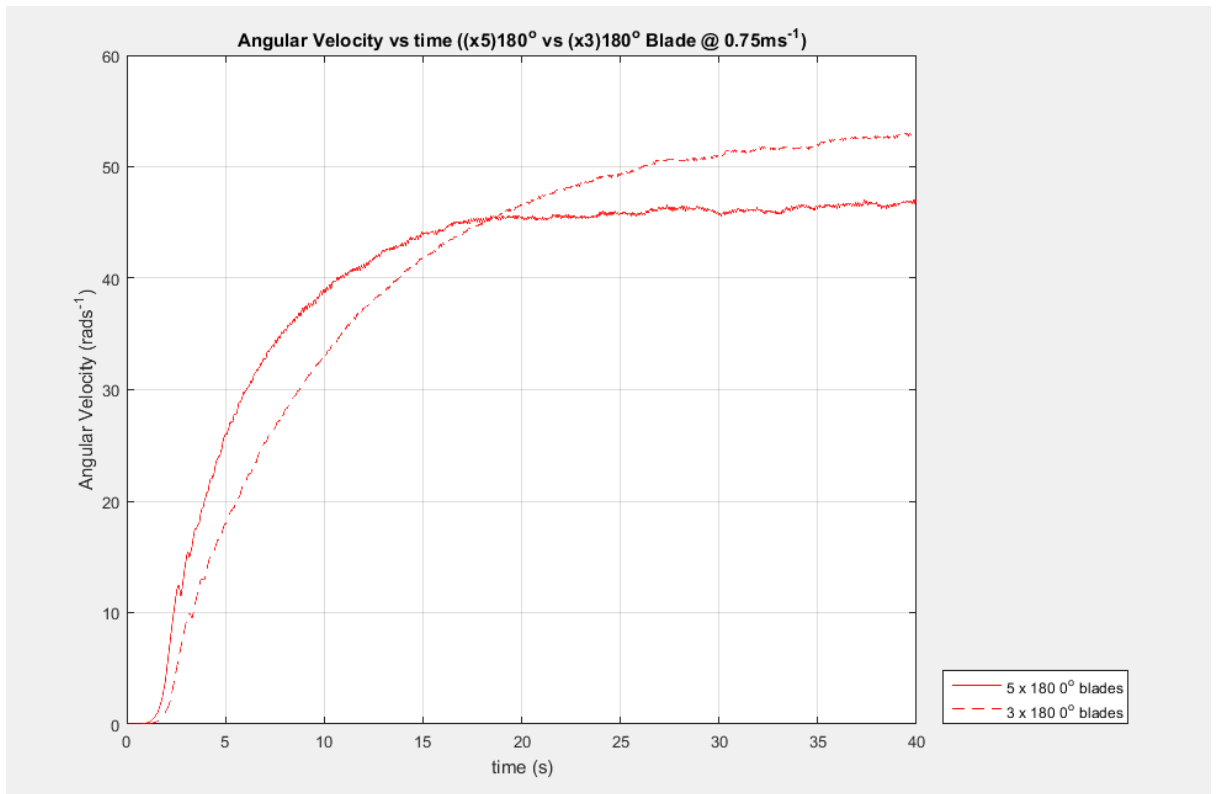


Figure 25: Comparison of 5 and 3 bladed turbines at  $0.75 \text{ ms}^{-1}$  wind speed (both  $180^\circ$  blades).

## 4.4 MATLAB Results Discussion

### 4.4.1 Optimum Offset

No optimum offset for maximum angular velocity was determinable from the results of the MATLAB simulations. The following table shows which 3 offsets gave the fastest angular velocity as the turbines reached the later stages of their initial acceleration (table.1). It should be noted however that the offset giving the maximum angular velocity changed constantly for all simulations, with no clear indication of any one giving the best performance.

Table 1: Table showing the 3 top offsets in terms of angular velocity at the later stages of the initial acceleration phase (for offset description see section 1.3).

	$0.75 \text{ ms}^{-1}$			$7.0 \text{ ms}^{-1}$		
Blade	1 <sup>st</sup>	2 <sup>nd</sup>	3 <sup>rd</sup>	1 <sup>st</sup>	2 <sup>nd</sup>	3 <sup>rd</sup>
$180^\circ$	0	-15	30	0	-15	30
$120^\circ$	0	30	45	-15	15	30

What can be said is that due to the anomaly presented in section (4.3.2), the author believes that selection of a negative offset may be detrimental to a turbines performance during the initial period of rotation from rest. The elements of negative torque presented from the negative offset configuration may work against the starting torque generated by the Savonius turbine. Wind tunnel testing to correlate this anomaly is required to ensure that the effect is not simply an artefact of the numerical process that generated the data.

#### 4.4.2 Optimum Arc Angle

The definition of optimum arc angle depends on what parameter is considered most important for a given turbine, maximum acceleration or maximum angular velocity. Across all simulations, the 180° turbine blades gave faster initial acceleration. This was balanced by reaching a peak angular velocity sooner, while the 120° blades accelerated for a longer period. At the lower wind speeds, the 180° blades gave better performance in both acceleration and peak angular velocity. At the higher wind speeds analysed the 120° blades, while accelerating slower, reached higher peak angular velocities.

As this project is aimed at producing turbines that will maximise performance at low to medium wind speeds ( $<10\text{ms}^{-1}$ ), the 180° blade may give better performance outright. However, if the purpose of the SPD blades is to increase the power production at higher wind speeds, while the Savonius component is used to provide performance at lower wind speeds, then the 120° arc may be more suitable. Given the relationship of Power = Torque\*Rotational Velocity, or

$$P = \tau * \omega$$

a determination of the amount power being produced by the turbines was attempted. Power at the 40 second mark of the simulations was sought for both blade types, using the 3 blades 0.03m radius data at both  $0.75\text{ms}^{-1}$  and  $7.0\text{ms}^{-1}$  wind speeds.

Unfortunately, to determine the power that the turbine could generate, the rotor would need to be turning at a rotational velocity slower than its maximum value. The author was unable to write a script to perform this function at the late stages of the project, and for this reason, no conclusive determination on an optimum arc angle could be made, despite the superior acceleration of the 180° arc blades at low wind speeds. The fluctuations of the angular acceleration data hindered attempts to use the equation

$$\tau = I * \alpha$$

with high negative power values being generated as a result. Investigations into the source of the large fluctuations in the acceleration data are warranted.

#### 4.4.3 Optimum Blade Number

The results of the MATLAB investigations showed that increasing the number of turbine blades increased the rate of acceleration of the turbines, while reducing the maximum angular velocity obtained. As with the optimum arc angle consideration, the optimum value for blade number depends on the application of the individual turbine design, with



greater numbers of turbine blades generally indicating a higher torque according to the simulations.

This must be considered alongside another aspect of turbine design, hitherto not discussed in this paper. Interaction between the turbulence and vortices of advancing blades and those that follow has a large impact on the performance of VAWT's. This is perhaps most notable in Darrieus style VAWT's in a detrimental context, whereas some positive effects have been noted in Savonius clusters (section 2.3). Having some characteristics of the Darrieus design (blades not overlapping on the central chord of the turbine) and Savonius design (not relying on aerodynamic lift for power production) investigations into the effects of blade turbulence interaction is warranted for further study.

As the number of turbine blades used on a turbine increases, the nature of the effects of turbulent wake interaction change. This is in terms of the period of revolution that a turbine blade spends in clean air versus turbulent wake flow, the intensity of the turbulence encountered, and the nature of the turbulent flow (vortices or not). This turbulent interaction may be detrimental, for instance reducing the wind speed impacting on a blade during the power producing portion of its revolution, thus reducing the power generated. However, there may be some beneficial effects, such as reducing the resistance to rotation through the period of rotation where the blade advances into the wind, thereby reducing negative power generation.

The data gathered by this project does not approach this area of study, instead focusing on the attempt to produce a simple quasi-static model that could be correlated to (and perhaps scaled with) wind tunnel tests. Due to the highly complex nature of fluid flows, which become even more complex with increasing interaction with multiple rotating surfaces (the blades), the author feels it is inappropriate to make any comment on an optimum number of blades, beyond saying that there is some evidence to suggest an improvement in power generation by using 5 blades as opposed to 3. Comparison between wind tunnel tests and MATLAB predicted results may shed more light on the reliability of the MATLAB model used.

With regards to self-furling of a prototype turbine in high wind speed condition, the use of a larger number of blades may act to reduce the maximum rotational velocity reached by a turbine. Again though, without more detailed analysis of the behaviour of a turbine with turbulent vortex and blade interaction, this possibility cannot be confirmed or disconfirmed. Also the increased solidity generated by addition of more blades may act to increase moment forces generated by the wind pushing against the turbines average centre of pressure.

## 5. Discussion

### 5.1 Experimental Procedure

There were several steps in the experimental procedure adopted in this project which led to results that were less successful than anticipated. However this is useful in indicating what future methods should be avoided in future work. The main problems encountered were with respect to the test apparatus used in the wind tunnel experimentation, the nature of the CFD analysis undertaken, and the quasi-static model used. Conduction of experiments in future work should take note of the following observations regarding this project.

### 5.2 Test Apparatus

The first problem with the test apparatus was the use of open ended test specimen blades. This limits the usefulness of the data to modelling of blades with the same relative length to diameter ratio as the test specimen. Model blades longer than this will have a different force per mm coefficient as a larger percentage of the flow they experience will be forced in the lateral plane, instead of being able to pass vertically around the ends of the blade. Additionally, the SPD VAWT that this project is aimed at designing will likely have end plates for support, meaning blades with closed ends. Use of test specimens with closed end plates would give more useful data for the modelling process and perhaps be more accurately reflected in 2 dimensional CFD analysis.

The test blade used in the wind tunnel experiment was only supported as a lever, through the universal joint of the base and onto the load cells. This arrangement allows oscillation of the test specimen about the universal joint, and may be responsible for the variations in the load cell readings. The author noted a high frequency vibration of the test specimen during testing, probably related to vortex formation and shedding from the surface of the blade. While this effect cannot be removed from the testing procedure, having a testing apparatus that supports the test specimen at both ends would probably limit the amount of oscillation that occurs as a result.

The load cells used in the data collection process were selected for their resolution and relatively low price, as well as the ability to simply attach the load cells to the test apparatus base and take force measurements. However, data collection could be improved by recording forces at a higher frequency for a period of time and then averaging the resulting data to obtain a more reliable data point for each measurement. This would, if done correctly, improve the accuracy of the data, as well as making the data measurement process easier.

Lack of CFD data prior to the wind tunnel testing process led to the incorrect positioning of the Pitot tube for recording pressure field data downstream of the test specimen. A Pitot tube that could be positioned closer to the blade surface would give data that could be correlated with the CFD model, assisting in determining the validity of the CFD predictions of flow characteristics. As the pressure tube for this kind of data sampling only needs to be at right angles to the flow, a small tube angled vertically could potentially be used to better effect than the large Pitot tube used. This would also allow

sampling of the pressure upstream of the test specimen with minimal disturbance to the flow.

### **5.3 CFD analysis**

The CFD analysis initially undertaken for this project could be improved somewhat. Use of a transient simulation would give a more useful data set for comparison to the wind tunnel results. This may include analysis of the rate of vortex formation and separation from the blade at different wind speeds, and the subsequent oscillation in forces experienced by the surface of the test specimen. Averaging of the forces generated over a period of time would give more useful data to compare with wind tunnel data.

Use of a rotating mesh would also be useful in determining to what extent the turbulent wakes of the blades of a prototype turbine could interact with one another. This would change between turbine designs, but the potential to determine some scaling factor for power production depending on the number of rotors, the tip speed ratio of the blades and their orientation exists.

3D modelling of the test specimen would also likely give more accurate data, being able to allow for flow in all 3 dimensions of the model domain. In addition a mesh independency study should be conducted thoroughly, to the point that the mesh can be determined to be of sufficient resolution that the changes between blade orientations can be safely attributed to real flow changes, not artefacts of an insufficiently posed model. As with the rotating mesh, 3D model and transient solution, computational resources become a factor in improving the quality of the CFD results, with exponentially higher solution times to be expected (section 2.1.5).

The author can now appreciate how involved a CFD analysis can be, and the extent to which a user must go to produce quality data.

### **5.4 Numerical Modelling**

The selection of the quasi-static MATLAB simulation script was in itself a result of the CFD and wind tunnel data obtained. Fluid flow is an inherently 3 dimensional continuum, prone to chaotic and turbulent behaviour. Testing the state of a test specimen at two static angles would not result in the same flow as would be generated by rotating the test specimen between the two positions, with movement of wake flow and vortices changing the characteristic of the resulting wake.

Trying to mimic this flow behaviour with an algorithm would be computationally demanding, and beyond the scope of most undergraduate degrees. Nevertheless, at low rotational velocities the flow around a prototype blade may be estimated by static data, meaning that the static-step model developed has some application. Correlation with wind tunnel testing may lead to an estimation of the range of rotational velocities that the model may be applied to.

Attempts to determine the power output of the turbine iterations were unsuccessful. It may be possible to make some estimations of the power output however. Finding an average value for the slope of the angular velocity plots would allow an interpolation of the average angular acceleration values. In this way, the power production at a particular

angular velocity and wind speed could be determined. This would yield effective data at speeds below the terminal velocity indicated by the data. At terminal velocity the average power approaches zero, hence the limit to acceleration.

As an example, consider (fig.80) in appendix D. At 5 seconds, the angular velocity is approximately  $25\text{rads}^{-1}$ , and the slope of the plot at this point (the acceleration) is approximately  $4\text{rads}^{-2}$ . Combining this data with an 'I' value of  $0.00008\text{kgm}^2$ , and using the equations from section (4.4.2) a power output at this rotational velocity and wind speed of approximately 0.8 mW would be predicted. Again, wind tunnel experiments would be required to confirm the accuracy of this prediction.

## **5.5 Wind Tunnel Testing of a Prototype Turbine**

This stage of the project was not attempted due to time restraints. However the method of testing would reflect the nature of the MATLAB program. A turbine with suitable proportions for wind tunnel testing (section 2.2.5), using blades the same diameter as those in the MATLAB program, would be fabricated, and include addition of mass to increase its moment of rotational inertia, in an attempt to slow its acceleration and allow more data to be captured before its maximum angular velocity is reached. By measuring the rate of acceleration and knowing the rotational inertia of the specimen, the torque being developed throughout each portion of the test regime may be determined. Knowing torque and rotational velocity, the power being used to accelerate the turbine could be inferred.

## **5.6 Benefits**

There are several benefits to come out of this project so far. A definite difference in the forces generated on  $180^\circ$  and  $120^\circ$  SPD blades was shown in the wind tunnel experiments. Greater coefficient of lift values were produced on the  $120^\circ$  blades through a range of angular offsets. When simulated in the simple MATLAB model, a tendency for these  $120^\circ$  blades to out-perform the  $180^\circ$  blades at higher wind speeds in terms of maximum angular velocity was observed. In contrast, improved performance at lower speeds by the  $180^\circ$  blades was also observed, with higher accelerations during the starting phase.

These results show potential to be able to alter the performance of a turbine by changing the blade type employed. It may even be possible to use a range of blade types on the same turbine to fine tune its performance. In addition to this, changing the radius of the turbine resulted in the simulation accelerating faster, and reaching a slower maximum angular velocity. It is possible that this effect could scale to provide a level of self-furling during high wind speed conditions.

Dimensionless parameter charts for the coefficients of lift and drag on  $120^\circ$  and  $180^\circ$  arc blades have been produced. This will enable designers to determine what forces could be expected on any diameter blade at analogous wind speeds. This information will be useful in determination of torque generation by a blade. It will also be useful as a tool when calculating the stresses a blade may endure at different wind speeds. Knowledge of these stresses will enable safe and effective design limits to be determined.

All of these contribute towards the ultimate goal of this project, assisting in the design and optimisation of renewable energy capture devices using predominantly recycled materials. This will allow remote and low income communities to enjoy the health and educational benefits that access to electricity provides. This in turn assists in steering humanity towards a sustainable and prosperous future.

## 6. Conclusion

An investigation into the modelling of a Simple Peripheral Drag VAWT was undertaken. CFD solutions to two nominal blade types of 180° and 120° internal arc and 20mm diameter were performed at a range of wind speeds achievable by the University wind tunnel. The results of these CFD simulations were compared to test data obtained from the wind tunnel using test specimens of the same sectional dimensions. The CFD data was not correlated by the wind tunnel data, and subsequent re-modelling using a different approach failed to achieve any useable data from the CFD analysis (section 4.1.2).

A quasi-static MATLAB model was written to attempt to predict the behaviour of a novel turbine design using blades of the same dimensions as the test specimens. The test data from the wind tunnel was used as baseline information for the MATLAB program to interpolate force data at different wind speeds encountered during the simulation for each blade. The MATLAB program was run using a range of variables to investigate their effect on the simulated turbines performance. This included altering the radius of the turbines rotors (10mm and 30mm), the free stream wind speed used ( $0.75 \text{ ms}^{-1}$  and  $7.0 \text{ ms}^{-1}$ ), the number of blades (3 and 5) and the internal arc of the blade (180° and 120°) (Appendix D2).

The model showed that at lower wind speeds the 180° arc blades gave better acceleration than the 120° arc blades and a higher rotational velocity. At the higher wind speeds the 180° blades accelerated faster during at the start of the simulation, however their maximum rotational velocity levelled out first, and the 120° blades continued accelerating to a greater rotation velocity than the 180° blades.

Increasing the number of blades on the simulated turbine increased the acceleration of the turbine, while reducing its maximum rotational velocity. No conclusive determination could be made as to an optimal offset angle for either blade type, with the plotted comparative data overlapping to a great degree (Appendix F2). However, there is some evidence that 120° blades may provide improved power generation at higher rotational velocities compared to the traditional 180° blades. Increasing the radius that the blades are mounted on the simulated turbine decreases the maximum rotational velocity while improving its initial acceleration from rest.

### 6.1 Contribution

1. Demonstrate the need for more thorough CFD process, including a mesh independency analysis, transient solution, and preferably a 3D analysis.
2. Gathered data from wind tunnel experiments indicating a difference in the flow characteristics between 180° and 120° arc blades in terms of coefficients of lift and drag at various orientations to the wind, each potentially advantageous depending on a particular turbines performance requirements.
3. Used this wind tunnel data to build a simple dimensionless parameter plot that may assist in the use of various diameters of turbines using the principals of similitude.
4. Used a quasi-static numerical model to demonstrate the potential effects of altering design parameters on the performance characteristics of novel SPD VAWT designs.

5. Proposed an experimental process for correlating the numerical models effectiveness.
6. Highlighted improvements that could be made to increase the usefulness of future experimental investigations related to this stage of the modelling process.

## 6.2 Further work

CFD results could be reinvestigated using transient simulations, after conducting a thorough mesh independency analysis. The data from these solutions could then be correlated with improved wind tunnel test data gathered with greater accuracy. Combined with a dimensionless parameter investigation, useful data may be produced for scale prototype pipe sizes. MATLAB modelling of a turbine could then be performed and correlated with wind tunnel testing of scale prototype to determine the usefulness of the quasi-static MATLAB model.

Further investigations could be made into the use of  $90^\circ$  or even  $60^\circ$  arc blades to see if lift effects of a greater magnitude can be observed and applied successfully to the SPD design. Research into the structural role of SPD blades in a turbines design could be pursued, including fatigue analysis and deformation under load of various blade shapes under operating conditions. Low cost methods of strengthening an SPD design without deleterious effects on its operation would be of interest to this project.

Options for the modular design of a hybrid Savonius and SPD VAWT could be investigated, to determine if there is an optimum arrangement to maximise power generation. The ability of SPD turbines to self-furl needs to be investigated to determine if braking mechanisms need to be investigated, or if other protection measures are required in adverse conditions.

## 6.3 Reflection

I have learnt about a range of experimental methods and procedures in the field of mechanical engineering over the last few months. One common theme that has come up through them all is the depth of knowledge and experience that can be required to gather useful data. At the start of the year I thought that I had a plan all ready to go. I gave myself 2 weeks to do a literature review about CFD and to learn ANSYS. Now, at the end of the project, I am beginning to understand the intricacies of mesh design and analysis, when and where different solution models are appropriate, and just how computationally demanding a rigorous solution can be.

A clearer plan at the outset would have allowed more efficient use of the time available, and perhaps given me the time to revisit aspects of the project that needed review. Having said that, it was good to have an opportunity to visit a few different areas of mechanical engineering and get a feel for their applications. Above all, it has been an educational experience learning how to learn, how to find the information I needed.

I would have liked to have 3D printed a range of scale hybrid turbines and wind tunnel tested them. It would have been satisfying to correlate even some of the hypotheses generated by the results of the numerical model. I will build a few basic SPD VAWTs this summer, take them to the beach, and see if I can correlate some of those hypotheses

in real conditions. I'll just make sure I have the right test types organised first, and perhaps I'll just concentrate on testing one of the parameters at a time.



# Bibliography

*ProJet 3500 SD & HD*, 2015, pamphlet, PDF, created by 3dsystems, 3dsystems, viewed 1/06/2016,  
<[http://www.3dsystems.com/sites/www.3dsystems.com/files/projet\\_3500\\_plastic\\_0115\\_usen\\_web.pdf](http://www.3dsystems.com/sites/www.3dsystems.com/files/projet_3500_plastic_0115_usen_web.pdf)>.

Akwa, JV, Alves da Silva Júnior, G & Petry, AP 2012, 'Discussion on the verification of the overlap ratio influence on performance coefficients of a Savonius wind rotor using computational fluid dynamics', *Renewable Energy*, vol. 38, no. 1, pp. 141-9.

Almohammadi, KM, Ingham, DB, Ma, L & Pourkashan, M 2013, 'Computational fluid dynamics (CFD) mesh independency techniques for a straight blade vertical axis wind turbine', *Energy*, vol. 58, pp. 483-93.

Çete, AR, Yükselen, MA & Kaynak, Ü 2008, 'A unifying grid approach for solving potential flows applicable to structured and unstructured grid configurations', *Computers & Fluids*, vol. 37, no. 1, pp. 35-50.

Daka, KR & Ballet, J 2011, 'Children's education and home electrification: A case study in northwestern Madagascar', *Energy Policy*, vol. 39, no. 5, pp. 2866-74.

Dawoud, M, Taha, I & Ebeid, SJ 2016, 'Mechanical behaviour of ABS: An experimental study using FDM and injection moulding techniques', *Journal of Manufacturing Processes*, vol. 21, pp. 39-45.

Deda Altan, B, Altan, G & Kovan, V 2016, 'Investigation of 3D printed Savonius rotor performance', *Renewable Energy*, vol. 99, pp. 584-91.

Dobrev, I & Massouh, F 2011, 'CFD and PIV investigation of unsteady flow through Savonius wind turbine', *Energy Procedia*, vol. 6, pp. 711-20.

Dornan, M & Shah, KU 'Energy policy, aid, and the development of renewable energy resources in Small Island Developing States', *Energy Policy*.

Farah, S, Anderson, DG & Langer, R 'Physical and mechanical properties of PLA, and their functions in widespread applications — A comprehensive review', *Advanced Drug Delivery Reviews*.

Gustavsson, M 2007, 'Educational benefits from solar technology—Access to solar electric services and changes in children's study routines, experiences from eastern province Zambia', *Energy Policy*, vol. 35, no. 2, pp. 1292-9.

'HAWT versus VAWT: Small VAWTs find a clear niche', 2003, *Refocus*, vol. 4, no. 4, pp. 44-6.

*World Energy Outlook 2013*, 2013, created by IEA, International Energy Agency,  
<<https://www.iea.org/Textbase/npsum/WEO2013SUM.pdf>>.

Jeon, KS, Jeong, JI, Pan, J-K & Ryu, K-W 2015, 'Effects of end plates with various shapes and sizes on helical Savonius wind turbines', *Renewable Energy*, vol. 79, pp. 167-76.

- Kanagawa, M & Nakata, T 2008, 'Assessment of access to electricity and the socio-economic impacts in rural areas of developing countries', *Energy Policy*, vol. 36, no. 6, pp. 2016-29.
- Lanzafame, R, Mauro, S & Messina, M 2014, '2D CFD Modeling of H-Darrieus Wind Turbines Using a Transition Turbulence Model', *Energy Procedia*, vol. 45, pp. 131-40.
- Liu, J & Niu, J 2016, 'CFD simulation of the wind environment around an isolated high-rise building: An evaluation of SRANS, LES and DES models', *Building and Environment*, vol. 96, pp. 91-106.
- Menter, FR 1996, 'On the Connection between One- and Two-Equation Models of Turbulence A2 - RODI, W', in G Bergeles (ed.), *Engineering Turbulence Modelling and Experiments*, Elsevier, Oxford, vol. 3, pp. 131-40.
- Ross, I & Altman, A 2011, 'Wind tunnel blockage corrections: Review and application to Savonius vertical-axis wind turbines', *Journal of Wind Engineering and Industrial Aerodynamics*, vol. 99, no. 5, pp. 523-38.
- Roy, S & Saha, UK 2013, 'Review on the numerical investigations into the design and development of Savonius wind rotors', *Renewable and Sustainable Energy Reviews*, vol. 24, pp. 73-83.
- Roy, S & Saha, UK 2014, 'An adapted blockage factor correlation approach in wind tunnel experiments of a Savonius-style wind turbine', *Energy Conversion and Management*, vol. 86, pp. 418-27.
- Roy, S & Ducoin, A 2016, 'Unsteady analysis on the instantaneous forces and moment arms acting on a novel Savonius-style wind turbine', *Energy Conversion and Management*, vol. 121, pp. 281-96.
- Saha, UK & Rajkumar, MJ 2006, 'On the performance analysis of Savonius rotor with twisted blades', *Renewable Energy*, vol. 31, no. 11, pp. 1776-88.
- Senatov, FS, Niaza, KV, Stepashkin, AA & Kaloshkin, SD 2016, 'Low-cycle fatigue behavior of 3d-printed PLA-based porous scaffolds', *Composites Part B: Engineering*, vol. 97, pp. 193-200.
- Shaheen, M, El-Sayed, M & Abdallah, S 2015, 'Numerical study of two-bucket Savonius wind turbine cluster', *Journal of Wind Engineering and Industrial Aerodynamics*, vol. 137, pp. 78-89.
- Sheldahl, RE, Feltz, LV & Blackwell, BF 1978, 'Wind tunnel performance data for two- and three-bucket Savonius rotors', *Journal of Energy*, vol. 2, no. 3, pp. 160-4.
- Tjiu, W, Marnoto, T, Mat, S, Ruslan, MH & Sopian, K 2015, 'Darrieus vertical axis wind turbine for power generation I: Assessment of Darrieus VAWT configurations', *Renewable Energy*, vol. 75, pp. 50-67.
- Tu, J 2013, *Computational fluid dynamics : a practical approach*, Second edition. edn, Elsevier/BH, Amsterdam.
- UP3D 2015, *UP3D information*, viewed 30/09/2016, <<https://www.up3d.com/?r=up>>.

Zhou, T & Rempfer, D 2013, 'Numerical study of detailed flow field and performance of Savonius wind turbines', *Renewable Energy*, vol. 51, pp. 373-81.

# Appendices

## Appendix A

### A1 Project Specification

ENG4111/4112 Research Project

#### **Project Specification**

For: Kristan Sedgman

Title: **Analysis of Circular Section blade profiles in a Simple Peripheral Drag VAWT:**

#### **Design Investigations and Performance Modelling**

Major: Mechanical Engineering Hons

Supervisors: Andreas Helwig and Ray Malpress

Enrolment: ENG4111 – ONC S1, 2016

ENG4112 – ONC S2, 2016

Project Aim: To investigate the suitability of 120° circular blade profiles for use in drag type VAWTs, and create a modelling program to predict the performance of a prototype Simple Peripheral Drag VAWT based on 120° and 180° circular section blade profiles.

#### **Programme: Issue A, 16th March 2016**


1. Research CFD modelling methodologies and design a suitable model to analyse the performance of various circular blade profiles.
2. Research wind tunnel testing methodologies and design a suitable set of data acquisition systems and tests to analyse the forces experienced by 120° and 180° circular section blade profiles at various wind speeds and orientations.
3. Design a suitable CFD model to analyse the dynamic performance of 120° and 180° circular blade profiles, arranged as a Simple Peripheral Drag rotor.
4. Use test data and literature reviews to develop a program to predict the performance of a novel SPD rotor, given geometry and wind speed inputs.
5. 3d print and conduct wind tunnel tests of a novel SPD rotor to verify the accuracy of the model.
6. Liaise with Supervisors and Staff in a professional manner, including appropriate communication protocols.

*If time and resources permit:*

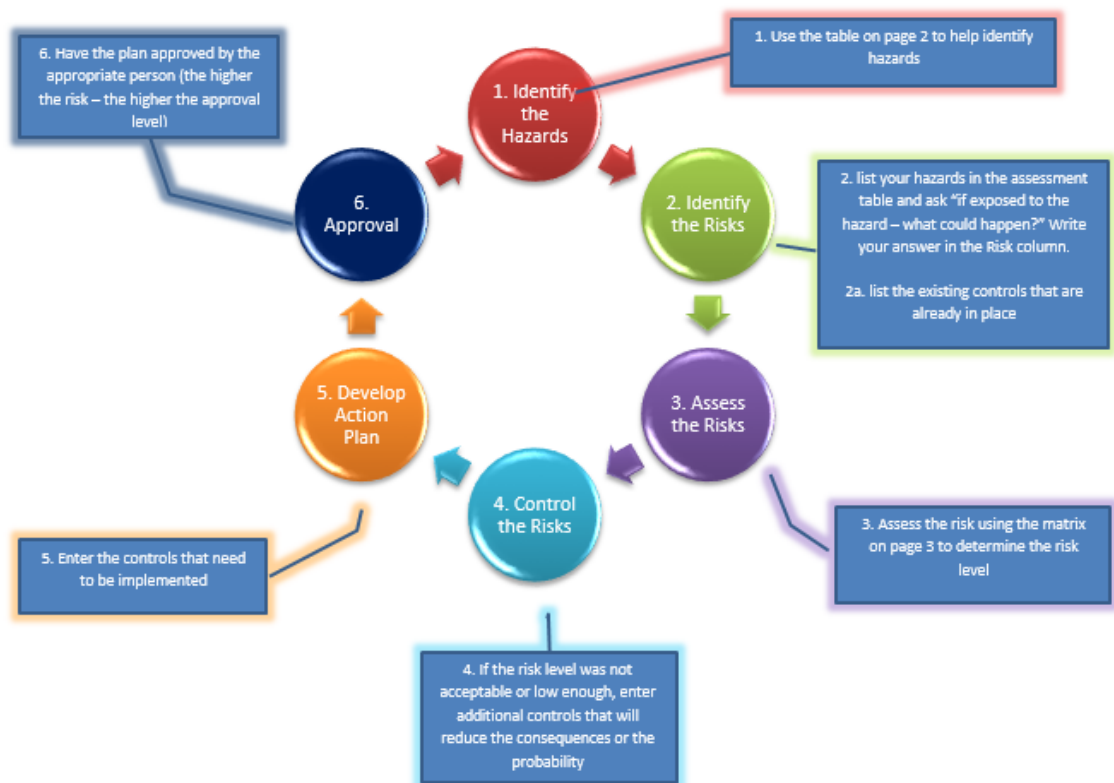
7. Refine the SPD modelling program.

## Appendix B

### B1 Risk Management Plan

 <div style="background-color: black; color: white; padding: 5px; text-align: center;">University of Southern Queensland</div> <h2 style="text-align: center;">Generic Risk Management Plan</h2>		
<b>Workplace (Division/Faculty/Section):</b> Faculty of health , Engineering and Science / Mechanical Engineering		
<b>Assessment No (if applicable):</b> 4	<b>Assessment Date:</b> 01/6/2016	<b>Review Date: (5 years maximum)</b> / /
<b>Context:</b> What is being assessed? Describe the item, job, process, work arrangement, event etc: Use of UV curing 3D printer		
<b>Assessment Team – who is conducting the assessment?</b>		
<b>Assessor(s):</b> Kristan Sedgman		
<b>Others consulted:</b> (eg elected health and safety representative, other personnel exposed to risks) Ray Malpress/Adrian Blokland		

### The Risk Management Process



J:\usqsafe\PZ USQ SMS\300 - EL3 - Risk Management\370 - Tools and Templates\RMP V3.5.docx

Page 1 of 7

Figure 26: Risk management plan image 1.

Step 1 - Identify the hazards (use this table to help identify hazards then list all hazards in the risk table)		
<b>General Work Environment</b>		
<input type="checkbox"/> Sun exposure	<input type="checkbox"/> Water (creek, river, beach, dam)	<input type="checkbox"/> Sound / Noise
<input type="checkbox"/> Animals / Insects	<input type="checkbox"/> Storms / Weather/Wind/Lightning	<input type="checkbox"/> Temperature (heat, cold)
<input type="checkbox"/> Air Quality	<input type="checkbox"/> Lighting	<input type="checkbox"/> Uneven Walking Surface
<input type="checkbox"/> Trip Hazards	<input type="checkbox"/> Confined Spaces	<input type="checkbox"/> Restricted access/egress
<input type="checkbox"/> Pressure (Diving/Altitude)	<input type="checkbox"/> Smoke	<input type="checkbox"/>
Other/Details: <input type="text"/>		
<b>Machinery, Plant and Equipment</b>		
<input checked="" type="checkbox"/> Machinery (fixed plant)	<input type="checkbox"/> Machinery (portable)	<input type="checkbox"/> Hand tools
<input type="checkbox"/> Laser (Class 2 or above)	<input type="checkbox"/> Elevated work platforms	<input type="checkbox"/> Traffic Control
<input type="checkbox"/> Non-powered equipment	<input type="checkbox"/> Pressure Vessel	<input type="checkbox"/> Electrical
<input type="checkbox"/> Vibration	<input type="checkbox"/> Moving Parts	<input type="checkbox"/> Acoustic/Noise
<input type="checkbox"/> Vehicles	<input type="checkbox"/> Trailers	<input type="checkbox"/> Hand tools
Other/Details: <input type="text"/>		
<b>Manual Tasks / Ergonomics</b>		
<input type="checkbox"/> Manual tasks (repetitive, heavy)	<input type="checkbox"/> Working at heights	<input type="checkbox"/> Restricted space
<input type="checkbox"/> Vibration	<input type="checkbox"/> Lifting Carrying	<input type="checkbox"/> Pushing/pulling
<input type="checkbox"/> Reaching/Overstretching	<input type="checkbox"/> Repetitive Movement	<input type="checkbox"/> Bending
<input type="checkbox"/> Eye strain	<input type="checkbox"/> Machinery (portable)	<input type="checkbox"/> Hand tools
Other/Details: <input type="text"/>		
<b>Biological</b> (e.g. hygiene, disease, infection)		
<input type="checkbox"/> Human tissue/fluids	<input type="checkbox"/> Virus / Disease	<input type="checkbox"/> Food handling
<input type="checkbox"/> Microbiological	<input type="checkbox"/> Animal tissue/fluids	<input type="checkbox"/> Allergenic
Other/Details: <input type="text"/>		
<b>Chemicals</b> Note: Refer to the label and Safety Data Sheet (SDS) for the classification and management of all chemicals.		
<input type="checkbox"/> Non-hazardous chemical(s)	<input type="checkbox"/> 'Hazardous' chemical (Refer to a completed <u>hazardous chemical risk assessment</u> )	
<input type="checkbox"/> Engineered nanoparticles	<input type="checkbox"/> Explosives	<input type="checkbox"/> Gas Cylinders
Name of chemical(s) / Details: <input type="text"/>		
<b>Critical Incident – resulting in:</b>		
<input type="checkbox"/> Lockdown	<input type="checkbox"/> Evacuation	<input type="checkbox"/> Disruption
<input type="checkbox"/> Public Image/Adverse Media Issue	<input type="checkbox"/> Violence	<input type="checkbox"/> Environmental Issue
Other/Details: <input type="text"/>		
<b>Radiation</b>		
<input type="checkbox"/> Ionising radiation	<input checked="" type="checkbox"/> Ultraviolet (UV) radiation	<input type="checkbox"/> Radio frequency/microwave
<input type="checkbox"/> Infrared (IR) radiation	<input type="checkbox"/> Laser (class 2 or above)	<input type="checkbox"/>
Other/Details: <input type="text"/>		
<b>Energy Systems – incident / issues involving:</b>		
<input type="checkbox"/> Electricity (incl. Mains and Solar)	<input type="checkbox"/> LPG Gas	<input type="checkbox"/> Gas / Pressurised containers
Other/Details: <input type="text"/>		
<b>Facilities / Built Environment</b>		
<input type="checkbox"/> Buildings and fixtures	<input type="checkbox"/> Driveway / Paths	<input checked="" type="checkbox"/> Workshops / Work rooms
<input type="checkbox"/> Playground equipment	<input type="checkbox"/> Furniture	<input type="checkbox"/> Swimming pool
Other/Details: <input type="text"/>		
<b>People issues</b>		
<input checked="" type="checkbox"/> Students	<input checked="" type="checkbox"/> Staff	<input type="checkbox"/> Visitors / Others
<input type="checkbox"/> Physical	<input type="checkbox"/> Psychological / Stress	<input type="checkbox"/> Contractors
<input type="checkbox"/> Fatigue	<input type="checkbox"/> Workload	<input type="checkbox"/> Organisational Change
<input type="checkbox"/> Workplace Violence/Bullying	<input type="checkbox"/> Inexperienced/new personnel	<input type="checkbox"/>
Other/Details: <input type="text"/>		

Figure 27: Risk management plan image2.

[illegible]

## Restricted Chemicals

11

11

11

---

---

---

---

---

---

---

---

---

---

---

Figure 28: Risk management plan image 3.

## Risk Matrix

Eg 1. Enter Consequence

		Consequence				
		Insignificant No Injury 0-\$5K	Minor First Aid \$5K-\$50K	Moderate Med Treatment \$50K-\$100K	Major Serious Injuries \$100K-\$250K	Catastrophic Death More than \$250K
Eg 2. Enter Probability	Almost Certain 1 in 2	M	H	E	E	E
	Likely 1 in 100	M	H	H	E	E
	Possible 1 in 1000	L	M	H	H	H
	Unlikely 1 in 10 000	L	L	M	M	M
	Rare 1 in 1 000 000	L	L	L	L	L
Recommended Action Guide						
E=Extreme Risk – Task <b>MUST NOT</b> proceed						
H=High Risk – Special Procedures Required (See USQSafe)						
M=Moderate Risk – Risk Management Plan/Work Method Statement Required						
L=Low Risk – Use Routine Procedures						

Eg 3. Find Action

Figure 29: Risk management plan image 4.



[illegible]

- 6 -





## B2 Test Apparatus Base



*Figure 33: LENS printed base and universal joint with load cells attached.*

## B3 Pitot Assembly and Graduation Collar



*Figure 34: Test specimen with graduated collar fitted (top) and complete Pitot tube and microcontroller assembly (bottom)*

## B4 STL File For 3D Printing

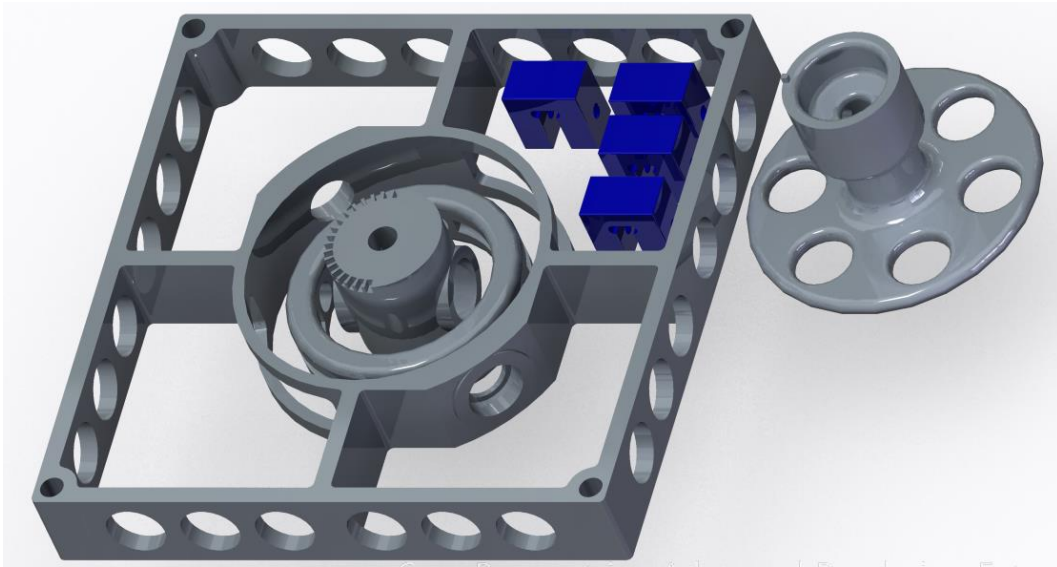


*Figure 35: Creo model ready to be transferred as an \*.stl file for LENS printing.*


## B5 Force Measurement Assembly

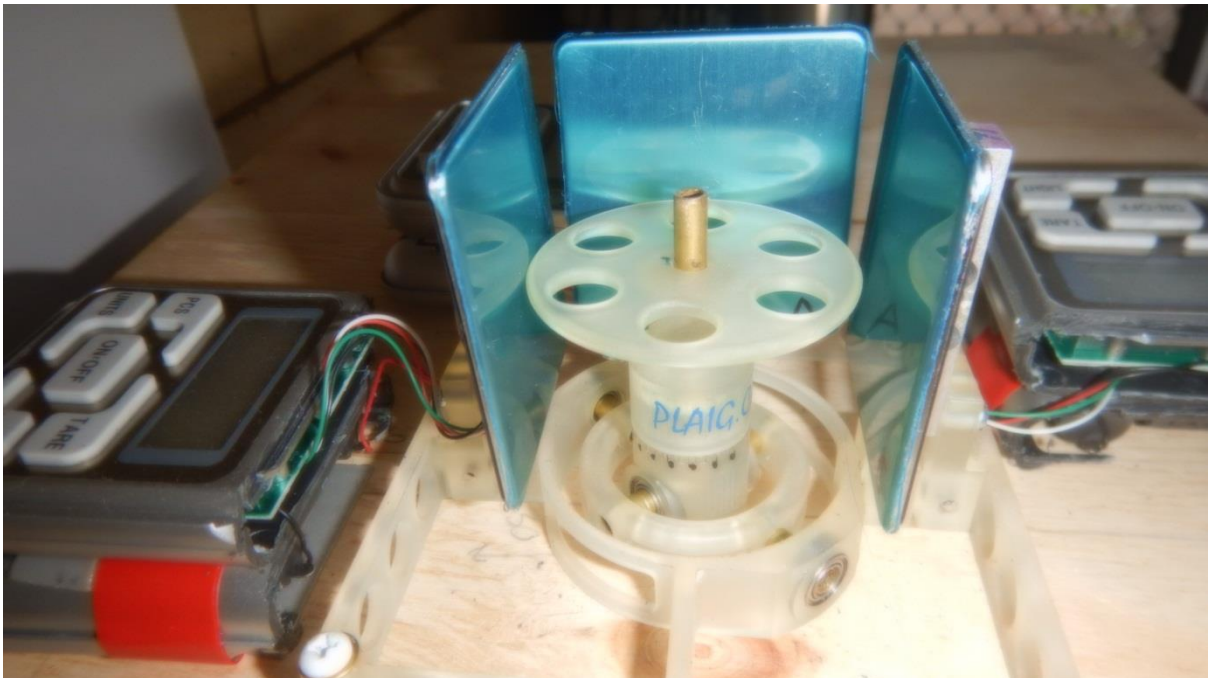


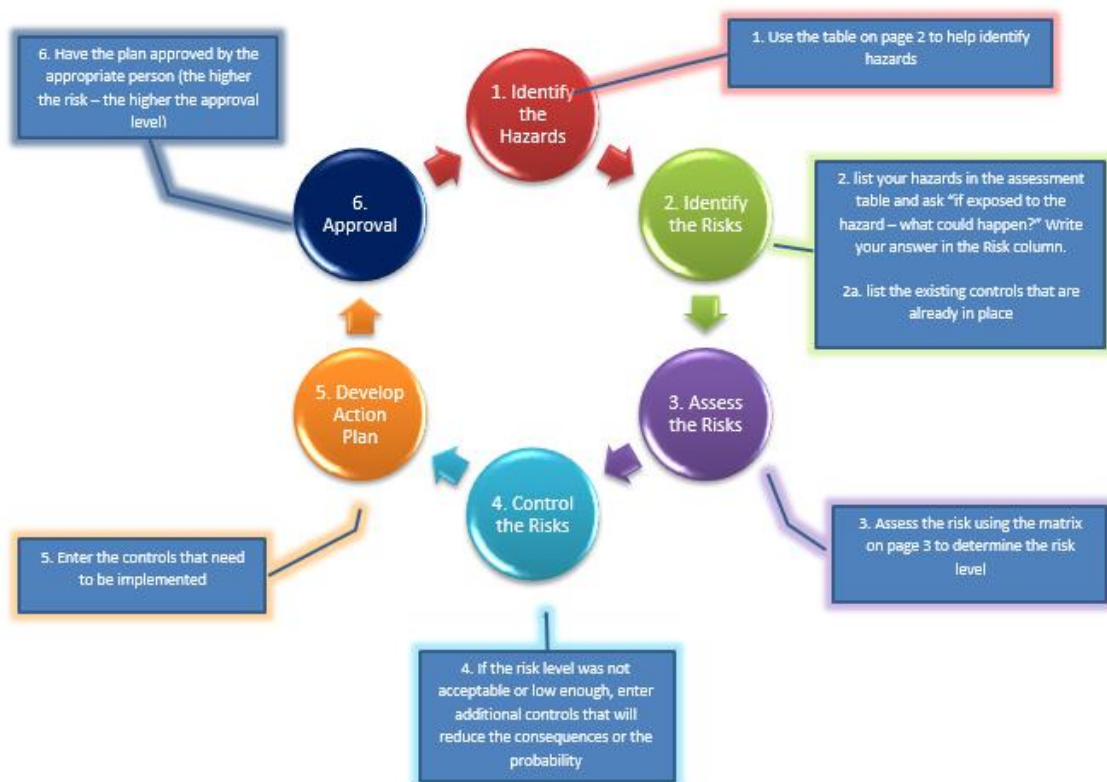
*Figure 36: Test specimen with graduation collar fitted in universal joint ready for wind tunnel testing.*

## Appendix C

### C1 Risk Management Plan

		
University of Southern Queensland		
Generic Risk Management Plan		
Workplace (Division/Faculty/Section): Faculty of health , Engineering and Science / Mechanical Engineering		
Assessment No (if applicable): 1	Assessment Date: 01/6/2016	Review Date: (5 years maximum) / /
Context: What is being assessed? Describe the item, job, process, work arrangement, event etc: Use of Wind Tunnel for testing purposes		
Assessment Team – who is conducting the assessment?		
Assessor(s): Kristan Sedgman		
Others consulted: (eg elected health and safety representative, other personnel exposed to risks) Ray Malpress		

### The Risk Management Process



J:\usqsafe\PZ USQ SMS\300 - EL3 - Risk Management\370 - Tools and Templates\RMP V3.5.docx

Page 1 of 7

Figure 37: Risk management plan image 1.



Step 1 - Identify the hazards (use this table to help identify hazards then list all hazards in the risk table)		
<b>General Work Environment</b>		
<input type="checkbox"/> Sun exposure	<input type="checkbox"/> Water (creek, river, beach, dam)	<input checked="" type="checkbox"/> Sound / Noise
<input type="checkbox"/> Animals / Insects	<input type="checkbox"/> Storms / Weather/Wind/Lightning	<input type="checkbox"/> Temperature (heat, cold)
<input type="checkbox"/> Air Quality	<input type="checkbox"/> Lighting	<input type="checkbox"/> Uneven Walking Surface
<input type="checkbox"/> Trip Hazards	<input type="checkbox"/> Confined Spaces	<input type="checkbox"/> Restricted access/egress
<input type="checkbox"/> Pressure (Diving/Altitude)	<input type="checkbox"/> Smoke	<input type="checkbox"/>
Other/Details: <input type="text"/>		
<b>Machinery, Plant and Equipment</b>		
<input checked="" type="checkbox"/> Machinery (fixed plant)	<input type="checkbox"/> Machinery (portable)	<input type="checkbox"/> Hand tools
<input type="checkbox"/> Laser (Class 2 or above)	<input type="checkbox"/> Elevated work platforms	<input type="checkbox"/> Traffic Control
<input checked="" type="checkbox"/> Non-powered equipment	<input type="checkbox"/> Pressure Vessel	<input type="checkbox"/> Electrical
<input type="checkbox"/> Vibration	<input checked="" type="checkbox"/> Moving Parts	<input type="checkbox"/> Acoustic/Noise
<input type="checkbox"/> Vehicles	<input type="checkbox"/> Trailers	<input type="checkbox"/> Hand tools
Other/Details: <input type="text"/>		
<b>Manual Tasks / Ergonomics</b>		
<input type="checkbox"/> Manual tasks (repetitive, heavy)	<input type="checkbox"/> Working at heights	<input type="checkbox"/> Restricted space
<input type="checkbox"/> Vibration	<input type="checkbox"/> Lifting Carrying	<input type="checkbox"/> Pushing/pulling
<input type="checkbox"/> Reaching/Overstretching	<input checked="" type="checkbox"/> Repetitive Movement	<input type="checkbox"/> Bending
<input type="checkbox"/> Eye strain	<input type="checkbox"/> Machinery (portable)	<input type="checkbox"/> Hand tools
Other/Details: <input type="text"/>		
<b>Biological</b> (e.g. hygiene, disease, infection)		
<input type="checkbox"/> Human tissue/fluids	<input type="checkbox"/> Virus / Disease	<input type="checkbox"/> Food handling
<input type="checkbox"/> Microbiological	<input type="checkbox"/> Animal tissue/fluids	<input type="checkbox"/> Allergenic
Other/Details: <input type="text"/>		
<b>Chemicals</b> Note: Refer to the label and Safety Data Sheet (SDS) for the classification and management of all chemicals.		
<input type="checkbox"/> Non-hazardous chemical(s)	<input type="checkbox"/> 'Hazardous' chemical (Refer to a completed <u>hazardous chemical risk assessment</u> )	
<input type="checkbox"/> Engineered nanoparticles	<input type="checkbox"/> Explosives	<input type="checkbox"/> Gas Cylinders
Name of chemical(s) / Details: <input type="text"/>		
<b>Critical Incident – resulting in:</b>		
<input type="checkbox"/> Lockdown	<input type="checkbox"/> Evacuation	<input type="checkbox"/> Disruption
<input type="checkbox"/> Public Image/Adverse Media Issue	<input type="checkbox"/> Violence	<input type="checkbox"/> Environmental Issue
Other/Details: <input type="text"/>		
<b>Radiation</b>		
<input type="checkbox"/> Ionising radiation	<input type="checkbox"/> Ultraviolet (UV) radiation	<input type="checkbox"/> Radio frequency/microwave
<input type="checkbox"/> Infrared (IR) radiation	<input type="checkbox"/> Laser (class 2 or above)	<input type="checkbox"/>
Other/Details: <input type="text"/>		
<b>Energy Systems – incident / issues involving:</b>		
<input type="checkbox"/> Electricity (incl. Mains and Solar)	<input type="checkbox"/> LPG Gas	<input type="checkbox"/> Gas / Pressurised containers
Other/Details: <input type="text"/>		
<b>Facilities / Built Environment</b>		
<input type="checkbox"/> Buildings and fixtures	<input type="checkbox"/> Driveway / Paths	<input checked="" type="checkbox"/> Workshops / Work rooms
<input type="checkbox"/> Playground equipment	<input type="checkbox"/> Furniture	<input type="checkbox"/> Swimming pool
Other/Details: <input type="text"/>		
<b>People issues</b>		
<input checked="" type="checkbox"/> Students	<input checked="" type="checkbox"/> Staff	<input checked="" type="checkbox"/> Visitors / Others
<input type="checkbox"/> Physical	<input type="checkbox"/> Psychological / Stress	<input type="checkbox"/> Contractors
<input type="checkbox"/> Fatigue	<input type="checkbox"/> Workload	<input type="checkbox"/> Organisational Change
<input type="checkbox"/> Workplace Violence/Bullying	<input checked="" type="checkbox"/> Inexperienced/new personnel	<input type="checkbox"/>
Other/Details: <input type="text"/>		

Figure 38: Risk management plan image 2.

Step 1 (cont) Other Hazards / Details (enter other hazards not identified on the table)	
<input type="checkbox"/>	
<input type="checkbox"/>	
<input type="checkbox"/>	
<input type="checkbox"/>	
<input type="checkbox"/>	
<input type="checkbox"/>	
<input type="checkbox"/>	
<input type="checkbox"/>	
<input type="checkbox"/>	
<input type="checkbox"/>	
<input type="checkbox"/>	
<input type="checkbox"/>	
<input type="checkbox"/>	
<input type="checkbox"/>	
<input type="checkbox"/>	
<input type="checkbox"/>	
<input type="checkbox"/>	
<input type="checkbox"/>	
<input type="checkbox"/>	
<input type="checkbox"/>	

Figure 39: Risk management plan image 3.



Risk Matrix

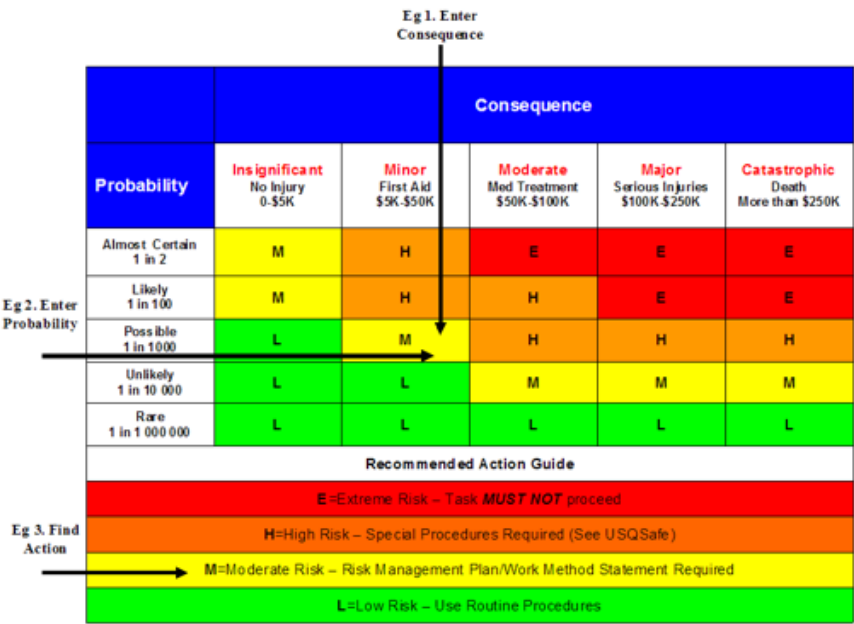


Figure 40: Risk management plan image 4.

## Risk register and Analysis

Step 1 (cont)	Step 2	Step 2a	Step 3			Step 4				
Hazards: From step 1 or more if identified	The Risk: What can happen if exposed to the hazard with existing controls in place?	Existing Controls: What are the existing controls that are already in place?	Risk Assessment: (use the Risk Matrix on p3) Consequence x Probability = Risk Level			Additional controls: Enter additional controls if required to reduce the risk level	Risk assessment with additional controls: (use the Risk Matrix on p3 – has the consequence or probability changed?)			Controls Implemented? Yes/No
			Consequence	Probability	Risk Level		Consequence	Probability	Risk Level	
Example Working in temperatures over 35° C	Heat stress/heat stroke/exhaustion leading to serious personal injury/death	Regular breaks, chilled water available, loose clothing, fatigue management policy.	catastrophic	possible	high	temporary shade shelters, essential tasks only, close supervision, buddy system	catastrophic	unlikely	mod	Yes
Noise	hearing damage for personnel doing the experiment.	Noise levels can not be reduced . PPE hearing protection required.	Minor	Unlikely	Low		Select a consequence	Select a probability	Select a Risk Level	Yes or No
Hand tools and moving parts	personal injury.	SOP to be followed . Personnel involved have been inducted in the correct use of all tools.	Minor	Unlikely	Low	Check tools for damage before use	Minor	Unlikely	Low	Yes or No
Staff or students come into the area	Personnel unfamiliar with the operation of the wind tunnel come into the area without appropriate PPE.	Display signage at entrances alerting personnel to the requirement of PPE and potential hazards.	Minor	Unlikely	Low		Select a consequence	Select a probability	Select a Risk Level	Yes or No
efflux from the wind tunnel lifts loose objects creating a flying object hazard.	Ensure the efflux is direct into a safe area free from objects which may become a hazard if lifted by the efflux.	Personnel operating the wind tunnel are aware of potential hazard from flying objects.	Moderate	Rare	Low		Select a consequence	Select a probability	Select a Risk Level	Yes or No
			Select a consequence	Select a probability	Select a Risk Level		Select a consequence	Select a probability	Select a Risk Level	Yes or No
			Select a consequence	Select a probability	Select a Risk Level		Select a consequence	Select a probability	Select a Risk Level	Yes or No
			Select a consequence	Select a probability	Select a Risk Level		Select a consequence	Select a probability	Select a Risk Level	Yes or No
			Select a consequence	Select a probability	Select a Risk Level		Select a consequence	Select a probability	Select a Risk Level	Yes or No

Figure 41: Risk management plan image 5.



Step 5 – Action Plan (for controls not already in place)			
Control Option	Resources	Person(s) responsible	Proposed implementation date

Step 6 – Approval			
<b>Drafter's Comments:</b> 			
<b>Drafter Details:</b> Name: Kristan Sedgman      Signature: Sedgman      Date: 1/6/2016			
<b>Assessment Approval:</b> (Extreme or High = VC, Moderate = Cat 4 delegate or above, Low = Manager/Supervisor) I am satisfied that the risks are as low as reasonably practicable and that the resources required will be provided.			
Name: Ray Malpress      Signature:      Date: / /			
Position Title:			

Figure 43: Risk management plan image 7.

## C2 Scales comparison



Figure 44: Image 1 from the verification process of the jewellery scales. A range of 0.04 grams was seen between the 3 scales. This was far below the level of fluctuations experienced in the wind tunnel testing.



Figure 45: Image 2 from the verification process of the jewellery scales.



*Figure 46: Image 3 from the verification process of the jewellery scales.*

### **C3 Test Rig on Wind Tunnel**



*Figure 47: Photograph of the testing apparatus on top of the wind tunnel test section, inlet to the left hand side of the image. The Pitot tube can be seen inserted into one of the 6 self-sealing slots available.*

## C4 Assembled Test Rig

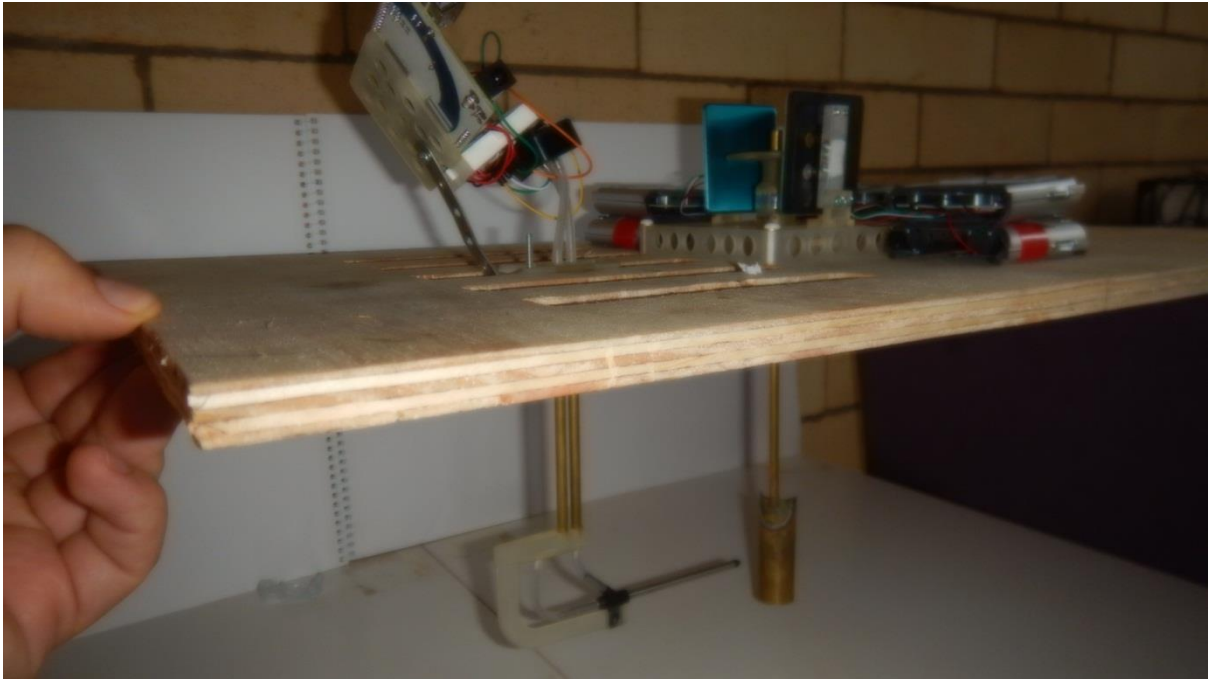


Figure 48: Photograph of the assembled test apparatus showing the Pitot tube for pressure data acquisition (left) and a test specimen connected through to the force measurement apparatus. The static pressure reading ports on the Pitot tube are too small to be seen in this image, and are about 2cm from the tip of the tube.

## Appendix D

### D1 MATLAB code

#### D1.1 Main Script

```
% *** version [1.8] ***
% Author[Kristan Sedgman, 3/10/2016]
% Script to model a turbine, given input parameters, using wind
tunnel
% data.
% Perform a loop for given duration
% Records angular velocity data and displays it...
% Increments offset angle and repeats... (-min : +max)
% Parameters: [# blades][blade type][blade_length][radius][wind
speed]
%           [inertia][timestep][duration]
%           [offset min][offset max][offset increment]
% loaded data columns format: [angle][180_x][180_y][120_x][120_y]]
% interpolated data columns format: [angle][x][y]
% Data imported from ".csv" files of wind tunnel data, into 3D
array
```



```

close all; clear; clc;
colours1 = ['r', 'g', 'm', 'k', 'b', 'y', 'c', '--', '-.', ':'];
blades = 3; % Number of turbine blades
blade_length = 60; % mm *****
r = 0.03; % [3cm]
windspeed = [0.75,0]; % [x,y] components
I = 0.00008; % Moment of inertia of proposed turbine design
[kg.m^2]
dt = 0.0002; % Timestep being used (s)
torque = 0; % Initialise the net torque value
omega = 0; alpha = 0; % angular velocity/acceleration
blade_angle = (2*pi)/blades;
angles = zeros(blades,2);
for i=1:blades
    angles(i,1) = (i-1)*blade_angle;
end
velocities = zeros(blades, 2); %[magnitude angle] components
apparent_ws = zeros(blades,4); % [x,y,angle,mag] components
forces = zeros(3,4); % [Fx, Fy, (angle from interp_vector),
magnitude]
off_min = -30; % Minimum offset angle
off_max = 45; % Maximum offset angle
off_step = 15; % Offset step size
offsets = (off_min:off_step:off_max); % Array of offsets angles
addpath('C:\Users\Kristan\Desktop\matlab');
data(:, :, 1) =
importdata('C:\Users\Kristan\Desktop\matlab\0.0.csv');
data(:, :, 2) =
importdata('C:\Users\Kristan\Desktop\matlab\6.6.csv');
data(:, :, 3) =
importdata('C:\Users\Kristan\Desktop\matlab\15.1.csv');
data(:, :, 4) =
importdata('C:\Users\Kristan\Desktop\matlab\20.1.csv');
ws_data = zeros(15,3,blades);
range = zeros(3,1); % Data sets to interpolate between
torc = zeros(blades,5); %[magnitude, tang_x, tang_y, int_x, int_y]
time = 0; % To determine time to reach top speed
duration = 40; % 40 seconds of data points
time_data_1 = zeros(4, (duration/dt)+1, length(offsets));
time_data_2 = zeros(4, (duration/dt)+1, length(offsets));

%time_data(1, :, :) = 0:dt:duration;
% Loop... \Blade type
%           \Offset angles
%           \Timesteps
% 180 degree blade first
blade_type = 1;
for c = 1:(length(offsets)) % For each offset angle trialed **
    time = 0; % Reset clock each loop
    offset = offsets(c); % Set the offset amount
    angles = zeros(blades,2); % RESET
    for i=1:blades % Start angles each loop from 0
        angles(i,1) = (i-1)*blade_angle;
    end
    alpha = 0; omega = 0; % RESET

    for n = 1:((duration/dt)+1)
        time_data_1(3,n,c) = omega;
        time_data_1(1,n,c) = time;
        velocities = veloc(velocities, angles, r, omega, blades);
        apparent_ws = apparent(apparent_ws, windspeed, velocities,
blades);
        range = det_range(apparent_ws, range, blades);

```



```

        ws_data = get_ws_data(apparent_ws, blades,
data,ws_data,range, blade_type);
        angles = get_angles(angles, apparent_ws, blades);
        forces = get_forces(ws_data, angles, forces, blades,
offset, blade_length);
        torc = get_torc(blaides, apparent_ws, forces, velocities,
torc);
        torque = (sum(torc(:,1))*r);
        alpha = torque/I;
        omega = omega+(alpha*dt);
        time = time + dt;
        time_data_1(2,n,c) = alpha;
        time_data_1(4,n,c) = velocities(1,1);
        angles = update_angles(angles, dt, omega, blades);
    end

end

% 120 degree blade next
blade_type = 2;
for c = 1:(length(offsets)) % For each offset angle trialed **
    time = 0; % Reset clock each loop
    offset = offsets(c); % Set the offset amount
    angles = zeros(blaides,2); % RESET
    for i=1:blades % Start angles each loop from 0
        angles(i,1) = (i-1)*blade_angle;
    end
    alpha = 0; omega = 0; % RESET

    for n = 1:((duration/dt)+1)
        time_data_2(3,n,c) = omega;
        time_data_2(1,n,c) = time;
        velocities = veloc(velocities,angles,r,omega,blades);
        apparent_ws = apparent(apparent_ws,windspeed,velocities,
blades);
        range = det_range(apparent_ws, range, blades);
        ws_data = get_ws_data(apparent_ws, blades,data,ws_data,
range, blade_type);
        angles = get_angles(angles, apparent_ws, blades);
        forces = get_forces(ws_data, angles, forces, blades,
offset, blade_length);
        torc = get_torc(blaides, apparent_ws, forces, velocities,
torc);
        torque = (sum(torc(:,1))*r);
        alpha = torque/I;
        omega = omega+(alpha*dt);
        time = time + dt;
        time_data_2(2,n,c) = alpha;
        time_data_2(4,n,c) = velocities(1,1);
        angles = update_angles(angles, dt, omega, blades);
    end

end

```

## D1.2 veloc Function

```

%                                     *** version [1.2] ***
% Author[Kristan Sedgman, 3/10/2016]
% Script to determine the tangential velocity [magnitude] and
[direction]
% of the blades for each iteration

```

```

function velocities = veloc(velocities, angles, r, omega, blades)
for n = 1:blades
    velocities(n,1) = r*omega; % Tangential velocity magnitude
    velocities(n,2) = angles(n) + (pi/2); % Tangential velocity
    direction
    if(velocities(n,2) >= (2*pi)) % Trim direction to within 0-2Pi
        velocities(n,2) = velocities(n,2)-(2*pi);
    end
    if(velocities(n,2) < 0)
        velocities(n,2) = velocities(n,2)+(2*pi);
    end
end
end

```

### D1.3 apparent Function

```

% *** version [1.2] ***
% Author[Kristan Sedgman, 3/10/2016]
% Script to determine the apparent windspeed magnitude and
direction
% experienced by each blade, a combination of velocity induced
flow and
% wind flow.
function apparent_ws = apparent(apparent_ws, windspeed, velocities,
blades)
for n=1:blades
    velocities(n,2) = velocities(n,2)+pi; % Add pi radians as wind
opposes direction
    if velocities(n,2) >=(2*pi) % Trim this angle to within 0-2Pi
        velocities(n,2) = velocities(n,2)-(2*pi);
    end
end
for n=1:blades % For each blade
    apparent_ws(n,1) = windspeed(1,1)+...
        ( velocities(n,1)*(cos(velocities(n,2))) ); % x data

    apparent_ws(n,2) = windspeed(1,2)+...
        ( velocities(n,1)*(sin(velocities(n,2))) ); % y data

    apparent_ws(n,3) = atan( (apparent_ws(n,2)) /...
        (apparent_ws(n,1)) ); % Angle of vector

    apparent_ws(n,4) = sqrt(apparent_ws(n,1)^2 +...
        apparent_ws(n,2)^2); % Magnitude of vector

    if apparent_ws(n,3) < 0 % Trim vector to within 0-2Pi
        apparent_ws(n,3) = (2*pi) + apparent_ws(n,3);
    end
    if apparent_ws(n,3) > (2*pi) % Trim vector to within 0-2Pi
        apparent_ws(n,3) = apparent_ws(n,3)-(2*pi);
    end
end

end

```

## D1.4 det\_range Function

```
% *** version [1.1] ***
% Author[Kristan Sedgman, 3/10/2016]
% Script to determine what range of windspeeds the [get_ws_data]
function
% needs to interpolate between for each blade.
function range = det_range(apparent_ws, range, blades)
for n = 1:blades
    if apparent_ws(n,4) > 20.1
        range(n,1) = 4;
    end
    if (apparent_ws(n,4) <= 20.1)&&(apparent_ws(n,4) > 15.1)
        range(n,1) = 3;
    end
    if (apparent_ws(n,4) <= 15.1)&&(apparent_ws(n,4) > 6.6)
        range(n,1) = 2;
    end
    if (apparent_ws(n,4) <= 6.6)&&(apparent_ws(n,4) >= 0)
        range(n,1) = 1;
    end
    % Could do with a catch statement here in case of error
end
end
```

## D1.5 get\_ws\_data Function

```
% *** version [1.3] ***
% Author[Kristan Sedgman, 3/10/2016]
% Script to build an interpolated array of windspeed data for each
blade,
% depending on the magnitude of the relative windspeed for each
blade.
% Data is linearly interpolated from the wind tunnel test data
loaded into
% the main program. Dependant on blade type.
function ws_data = get_ws_data(apparent_ws, blades, data, ws_data,
range,...
    blade_type)

% case loop for... \Blade type
% \Range of windspeed data to interpolate
between
switch blade_type
case 1
    for n = 1:blades % For each blade
        range_n = range(n);
        switch range_n
        case 1
            for r = 1:15
                ws_data(r,2, n) = (apparent_ws(n,4)-
0)/(6.6-0) *...
                    (data(r,2,2)-(data(r,2,1)));
                ws_data(r,3, n) = (apparent_ws(n,4)-
0)/(6.6-0) *...
                    (data(r,3,2)-(data(r,3,1)));
            end
        end
    end
end
```

```

        case 2
            for r = 1:15
                ws_data(r,2,n)=(apparent_ws(n,4)-
6.6)/(15.1-6.6) *...
                    (data(r,2,3)-(data(r,2,2)));
                ws_data(r,3,n)=(apparent_ws(n,4)-
6.6)/(15.1-6.6) *...
                    (data(r,3,3)-(data(r,3,2)));
            end

        case 3
            for r = 1:15
                ws_data(r,2,n)=(apparent_ws(n,4)-
15.1)/(20.1-15.1)*...
                    (data(r,2,4)-(data(r,2,3)));
                ws_data(r,3,n)=(apparent_ws(n,4)-
15.1)/(20.1-15.1)*...
                    (data(r,3,4)-(data(r,3,3)));
            end

        case 4
            for r = 1:15
                % Linear extrapolation of data, hopefully
the required wind
                % speed isn't too far off 20.1 ms-1
                ws_data(r,2,n)=(data(r,2,4)-
data(r,2,3))/(20.1-15.1) *...
                    (apparent_ws(n,2)-20.1);
                ws_data(r,3,n)=(data(r,3,4)-
data(r,3,3))/(20.1-15.1) *...
                    (apparent_ws(n,3)-20.1);
            end

        end
        ws_data(:,1,n) = data(:,1,1); % write angle values
into the
        %interpolated array
    end

    case 2
        for n = 1:blades % For each blade
            range_n = range(n);
            switch range_n

                case 1
                    for r = 1:15
                        ws_data(r,2, n) = (apparent_ws(n,4)-
0)/(6.6-0) *...
                            (data(r,4,2)-(data(r,4,1)));
                        ws_data(r,3, n) = (apparent_ws(n,4)-
0)/(6.6-0) *...
                            (data(r,5,2)-(data(r,5,1)));
                    end

                case 2
                    for r = 1:15
                        ws_data(r,2,n)=(apparent_ws(n,4)-
6.6)/(15.1-6.6) *...
                            (data(r,4,3)-(data(r,4,2)));
                        ws_data(r,3,n)=(apparent_ws(n,4)-
6.6)/(15.1-6.6)*...
                            (data(r,5,3)-(data(r,5,2)));
                    end

```

```

        case 3
            for r = 1:15
                ws_data(r,2,n)=(apparent_ws(n,4)-
15.1)/(20.1-15.1)*...
                    (data(r,4,4)-(data(r,4,3)));
                ws_data(r,3,n)=(apparent_ws(n,4)-
15.1)/(20.1-15.1)*...
                    (data(r,5,4)-(data(r,5,3)));
            end

        case 4
            for r = 1:15
                % Linear extrapolation of data, hopefully the
required wind
                % speed isn't too far off 20.1 ms-1
                ws_data(r,2,n)=(data(r,4,4)-
data(r,4,3))/(20.1-15.1)...
                    * (apparent_ws(n,2)-20.1);
                ws_data(r,3,n)=(data(r,5,4)-
data(r,5,3))/(20.1-15.1)...
                    * (apparent_ws(n,3)-20.1);
            end

        end
        ws_data(:,1,n) = data(:,1,1); % write angles into the
interpolated array
    end
end

end

```

## D1.6 get\_angles Function

```

%                                     *** version [1.3] ***
% Author[Kristan Sedgman, 3/10/2016]
% Function to determine the angle at which each blade interacts
with flow
function angles = get_angles(angles, apparent_ws, blades)
for n = 1:blades % For each blade
    angles(n,2) = angles(n,1)-apparent_ws(n,3);
    if angles(n,2) < 0
        angles(n,2) = angles(n,2)+(2*pi);
    end
    if angles(n,2) > (2*pi)
        angles(n,2) = angles(n,2)-(2*pi);
    end
end
end
end

```

## D1.7 get\_forces Function

```

%                                     *** version [1.3] ***
% Author[Kristan Sedgman, 3/10/2016]
% Script to linearly interpolate the x and y components of force
for each
% blade from the ws_data array built by the [get_ws_data]function.

```

```

function forces = get_forces(ws_data, angles, forces, blades,
offset,...
    blade_length)

local_angles = angles; % Local array to work with
for j = 1:blades % For each blade
    local_angles(j,2) = local_angles(j,2)+((offset/360)*(2*pi));
end
for i = 1:blades % Trim range to within 0-2Pi
    if local_angles(i,2)>(2*pi)
        local_angles(i,2)=local_angles(i,2)-(2*pi);
    end
    if local_angles(i,2)<0
        local_angles(i,2)=local_angles(i,2)+(2*pi);
    end
end
for n = 1:blades % Each blades force linearly interpolated by
*angle*
    % against its interpolated *data* array
    forces(n,1) = interp1( ws_data(:,1,n), ws_data(:,2,n),...
        (local_angles(n,2)/((2*pi)*360)) *blade_length); %force/mm
* mm
    forces(n,2) = interp1( ws_data(:,1,n), ws_data(:,3,n),...
        (local_angles(n,2)/((2*pi)*360)) *blade_length);
    forces(n,3) = atan(forces(n,2)/forces(n,1));
    if forces(n,3) > (2*pi) % Resulting direction trimmed to
within
        % 0-2Pi (to be sure to be sure)
        forces(n,3) = forces(n,3)-(2*pi);
    end
    if forces(n,3) < (2*pi)
        forces(n,3) = forces(n,3)+(2*pi);
    end
    forces(n,4) = sqrt(forces(n,1)^2 + forces(n,2)^2); % Magnitude
of Force
end

end

```

## D1.8 get\_torc Function

```

%
% *** version [1.2] ***
% Author[Kristan Sedgman, 3/10/2016]
% Script to determine the force in the tangential direction for
each blade.
% Use of the modified cosine rule for cartesian values.
function torc = get_torc(blaides, apparent_ws, forces, velocities,
torc)
for n = 1:blades
    % Determine the x and y components of the tangential unit
vector,
    % and store them in the torc array (2 and 3)...
    torc(n,2) = 1*cos(velocities(n,2));
    torc(n,3) = 1*sin(velocities(n,2));

    % Determine the x and y components of the resultant vectors,
% relative to the datum, and store them in the torc array (4
and 5)...
    torc(n,4) = forces(n,4) * (cos(apparent_ws(n,3)-forces(n,3)));

```

```

torc(n,5) = forces(n,4) * (sin(apparent_ws(n,3)-forces(n,3)));

% A cosine rule states: cos_O = u.v / |u|.|v|
% and cos_O is the action to project the resultant force
% onto the tangential vector, therefore I need to multiply
% the resultant magnitude by this result.
% u = resultant vectors
% v = tangential vectors
% torque = magnitude * [u(1)*v(1) + u(2)*v(2)] /
[u(4)*v(1)]
torc(n,1) = forces(n,4) * ( (torc(n,4)*torc(n,2) +
torc(n,5)*torc(n,3))...
/ (forces(n,4)*1) );
end
end

% *** version [1.4] ***
% Author[Kristan Sedgman, 3/10/2016]
% Script to increment the angles of the blades between iterations,
trimming
% them to between 0 and 2Pi radians
function angles = update_angles(angles, dt, omega, blades)
for n = 1:blades
angles(n,1) = angles(n,1) + (angles(n,1)*(omega*dt));
if angles(n,1) > (2*pi)
angles(n,1) = angles(n,1) - (2*pi);
end
if angles(n,1) < 0
angles(n,1) = angles(n,1) + (2*pi);
end
end
end
end

```

## D2 Variable Comparison

### D2.1 Blade arc angle comparison data

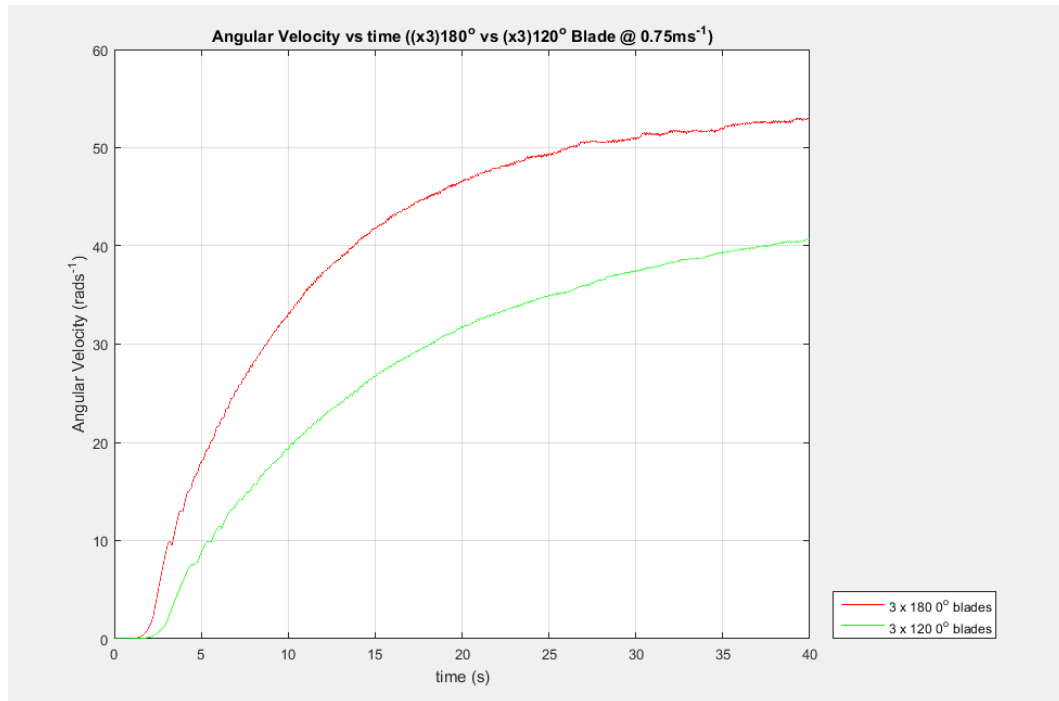


Figure 49: Comparison of (3) blade arc angles at 0.75 ms<sup>-1</sup>.

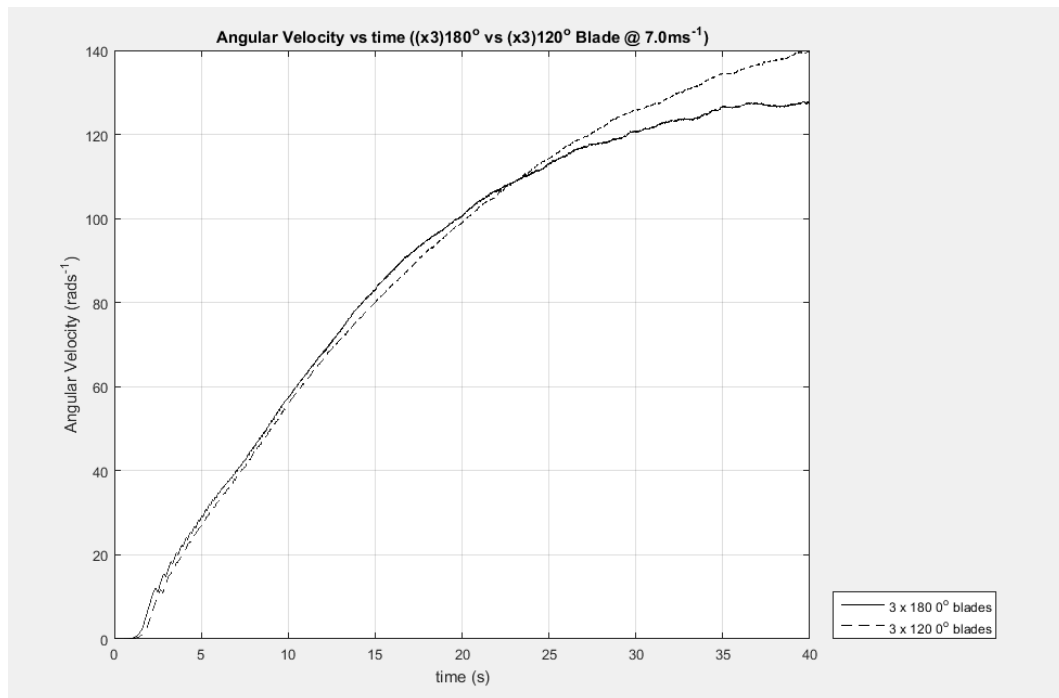


Figure 50: Comparison of (3) blade arc angles at 7.0 ms<sup>-1</sup>.



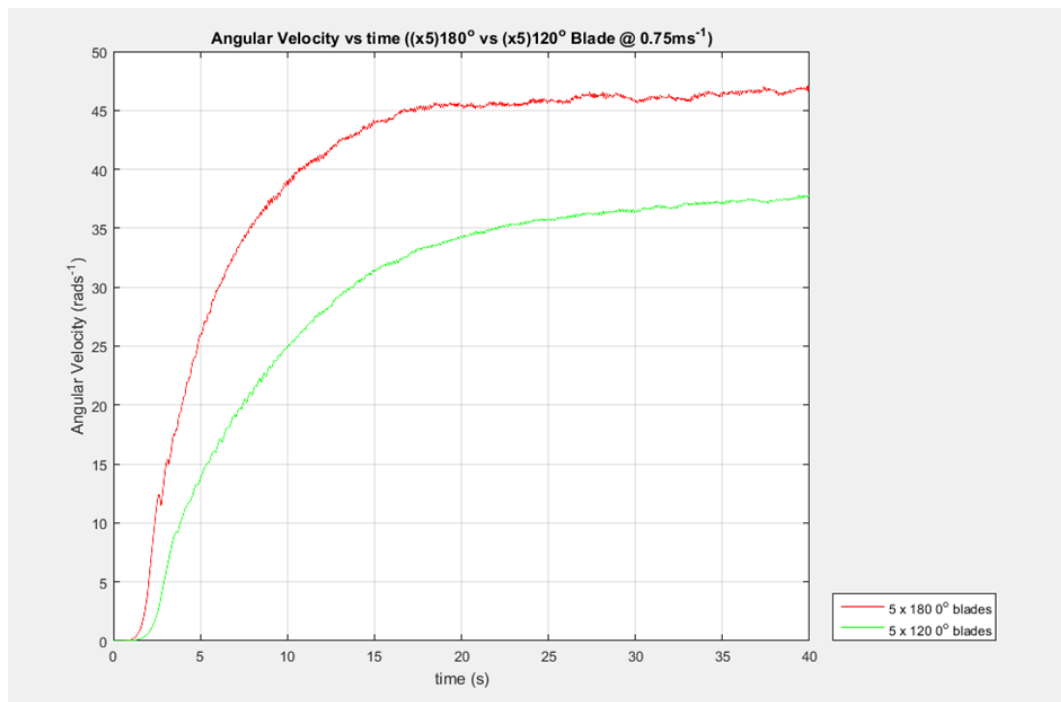


Figure 51: Comparison of (5) blade arc angles at 7.0 ms<sup>-1</sup>.

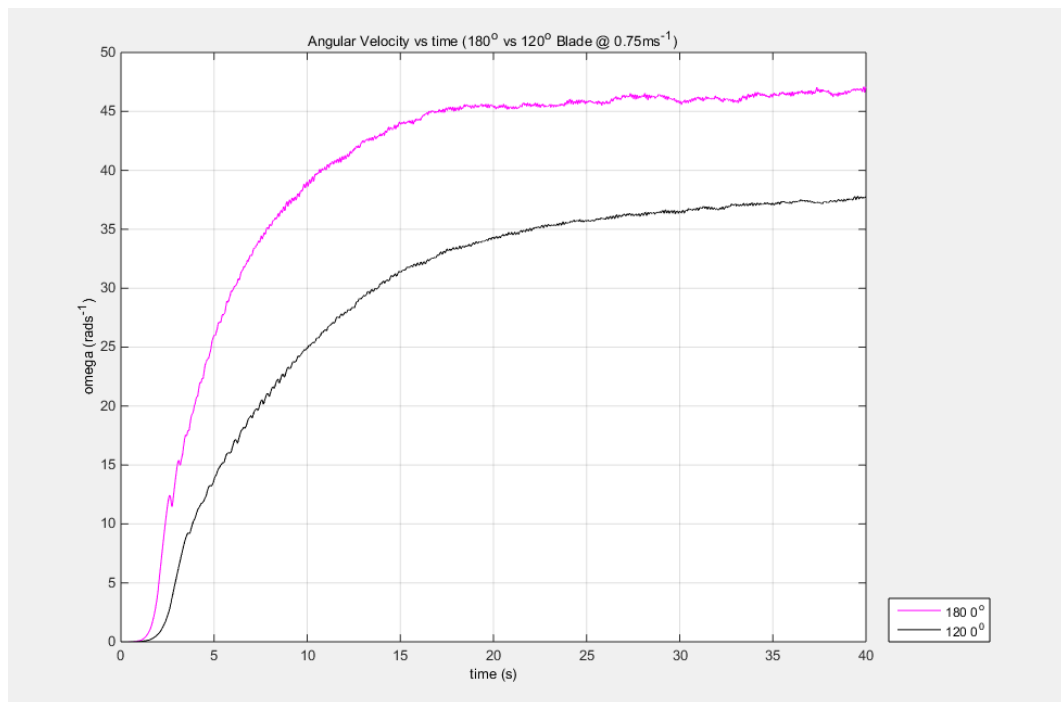


Figure 52: Comparison of 180° vs 120° blades at 0.75 ms<sup>-1</sup>.

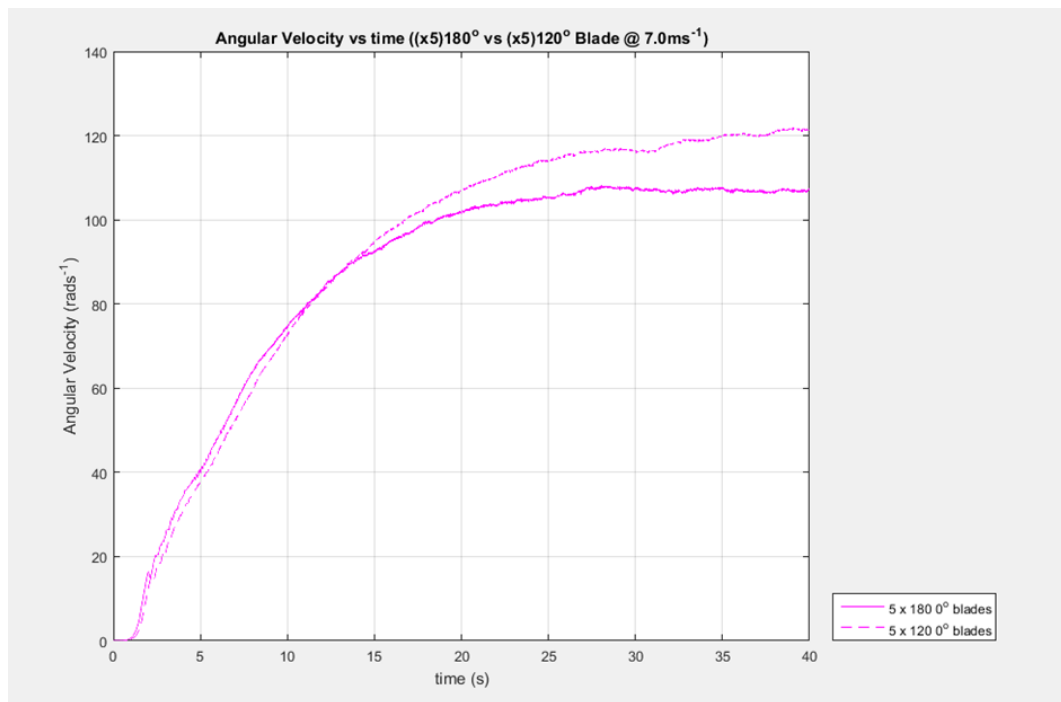


Figure 53: Comparison of (5) blade arc angles at  $7.0 \text{ ms}^{-1}$ .

## D2.2 Blade Number comparison data

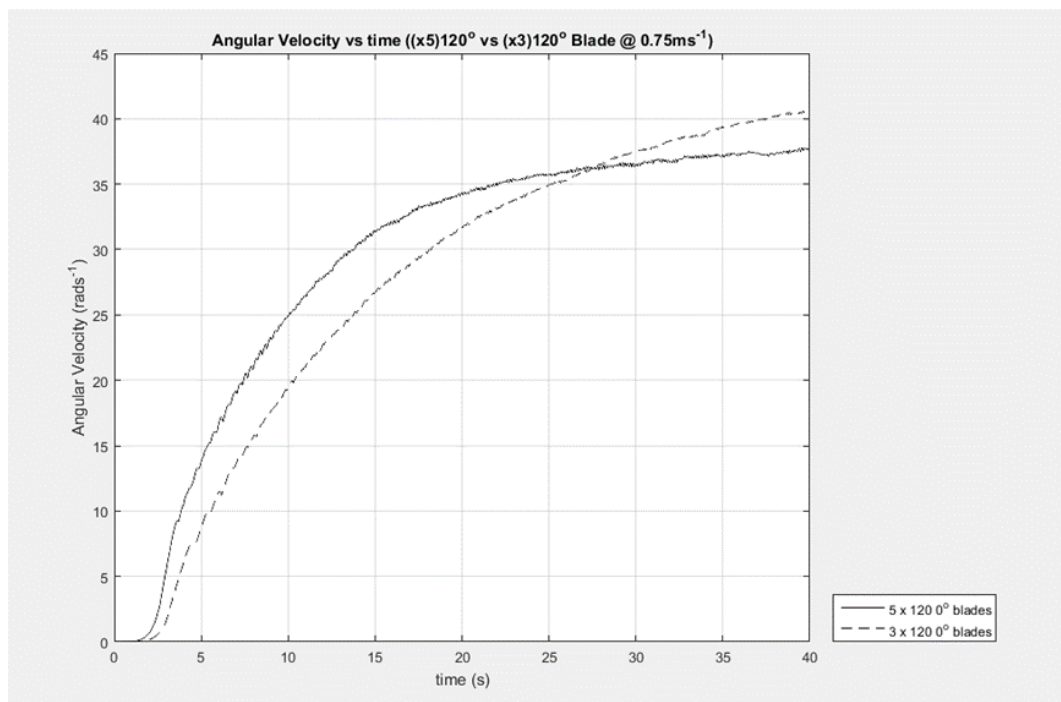


Figure 54: Comparison of (120°) blade numbers at  $0.75 \text{ ms}^{-1}$ .

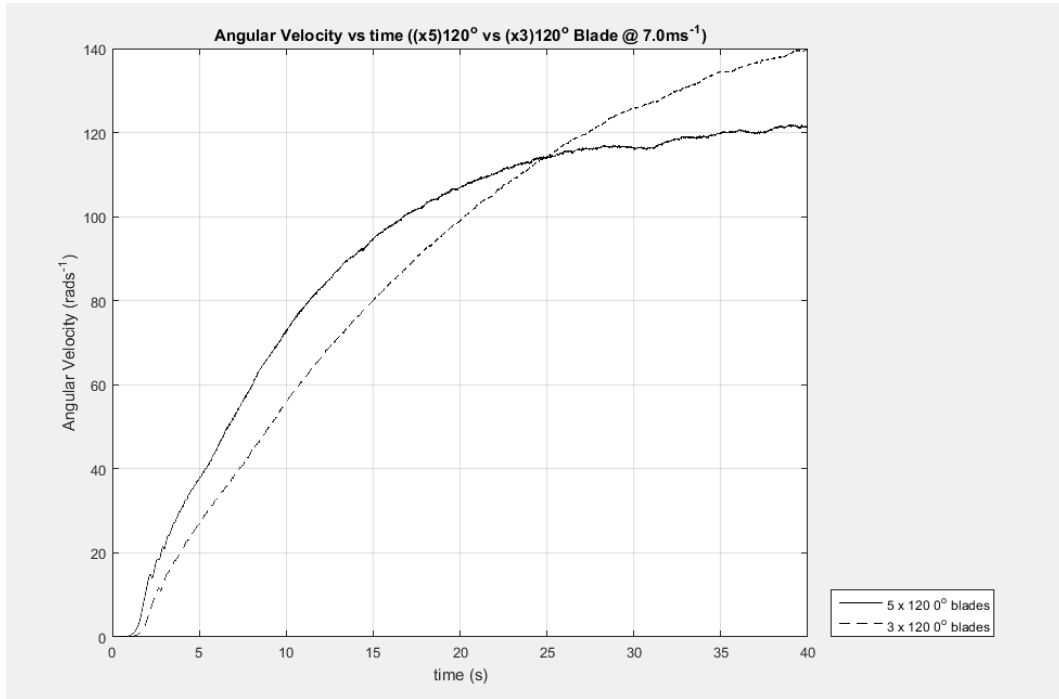


Figure 55: Comparison of (120°) blade numbers at 7.0 ms<sup>-1</sup>.

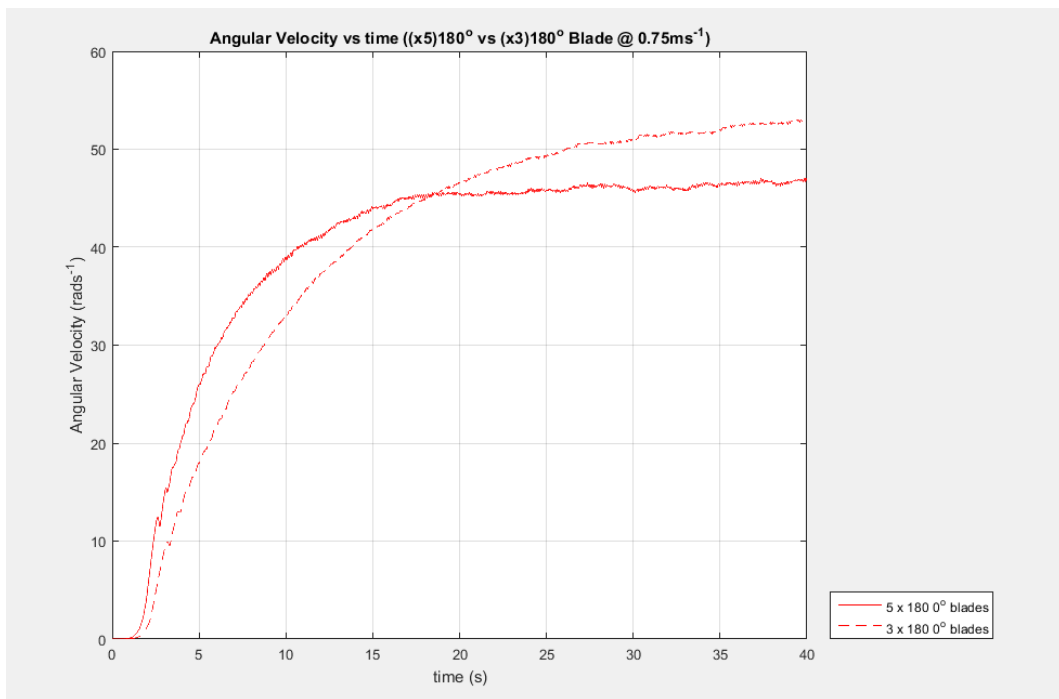


Figure 56: Comparison of (180°) blade numbers at 0.75 ms<sup>-1</sup>.

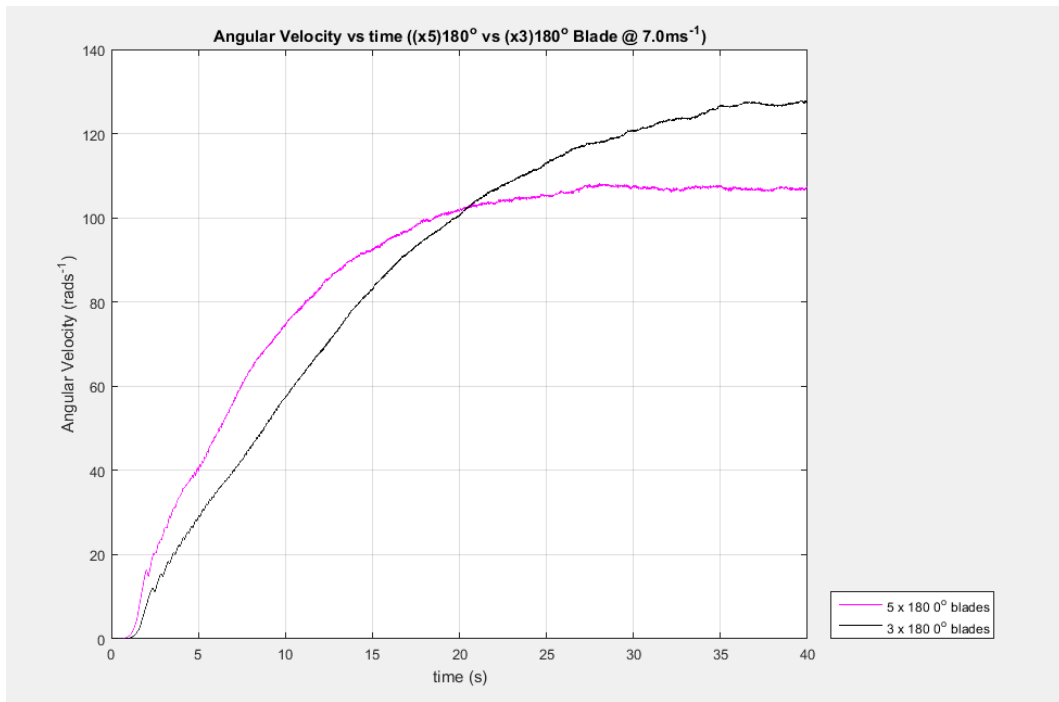


Figure 57: Comparison of (180°) blade numbers at 7.0 ms<sup>-1</sup>.

## D2.3 Turbine Radius comparison data

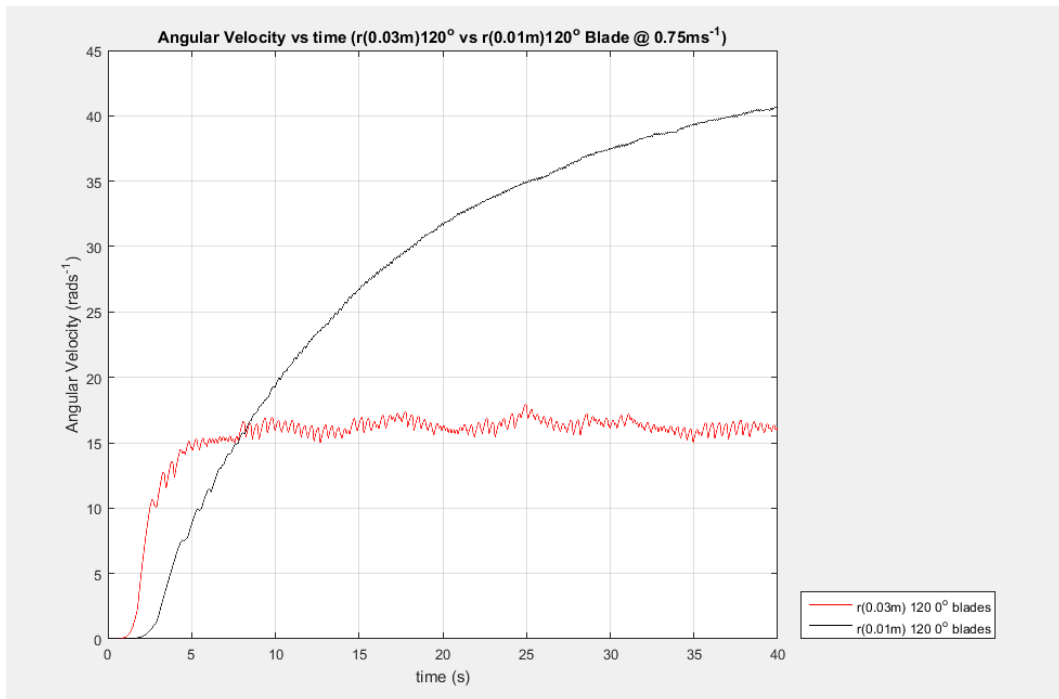


Figure 58: Comparison of (120°) turbine radius at 0.75 ms<sup>-1</sup>.

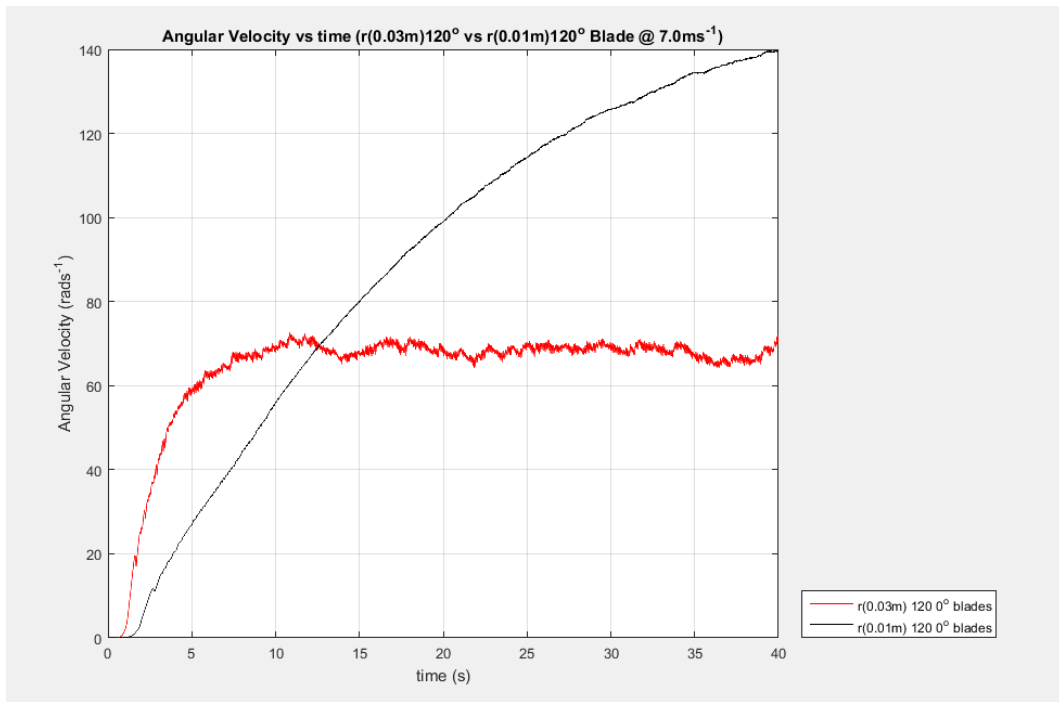


Figure 59: Comparison of (120°) turbine radius at 7.0 ms<sup>-1</sup>.

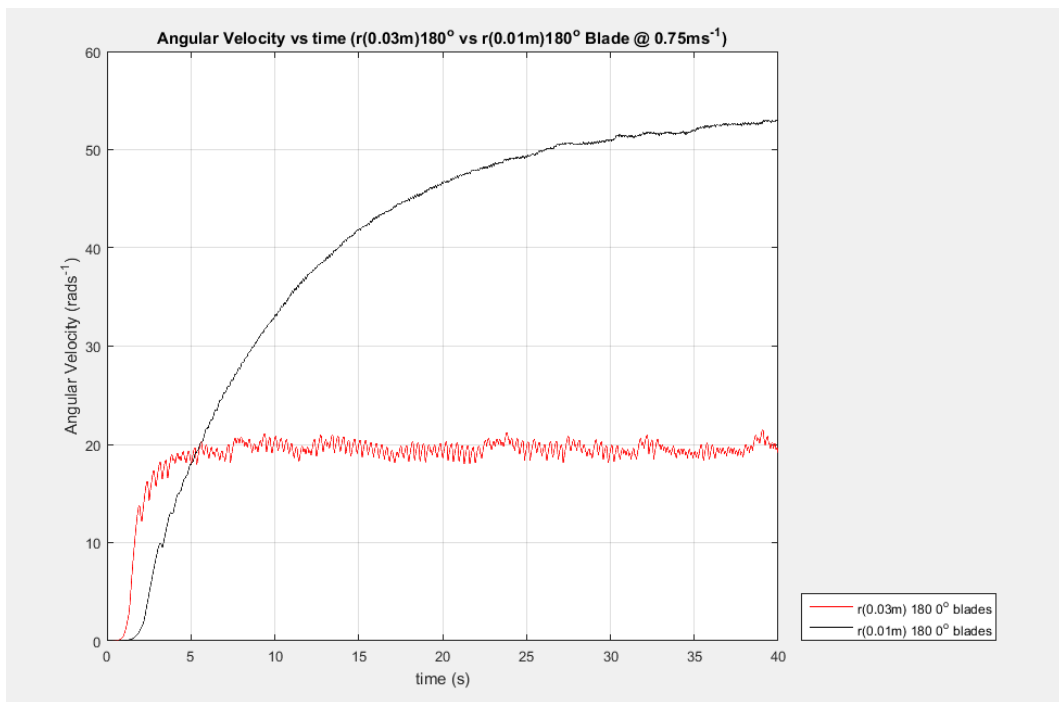


Figure 60: Comparison of (180°) turbine radius at 0.75 ms<sup>-1</sup>.

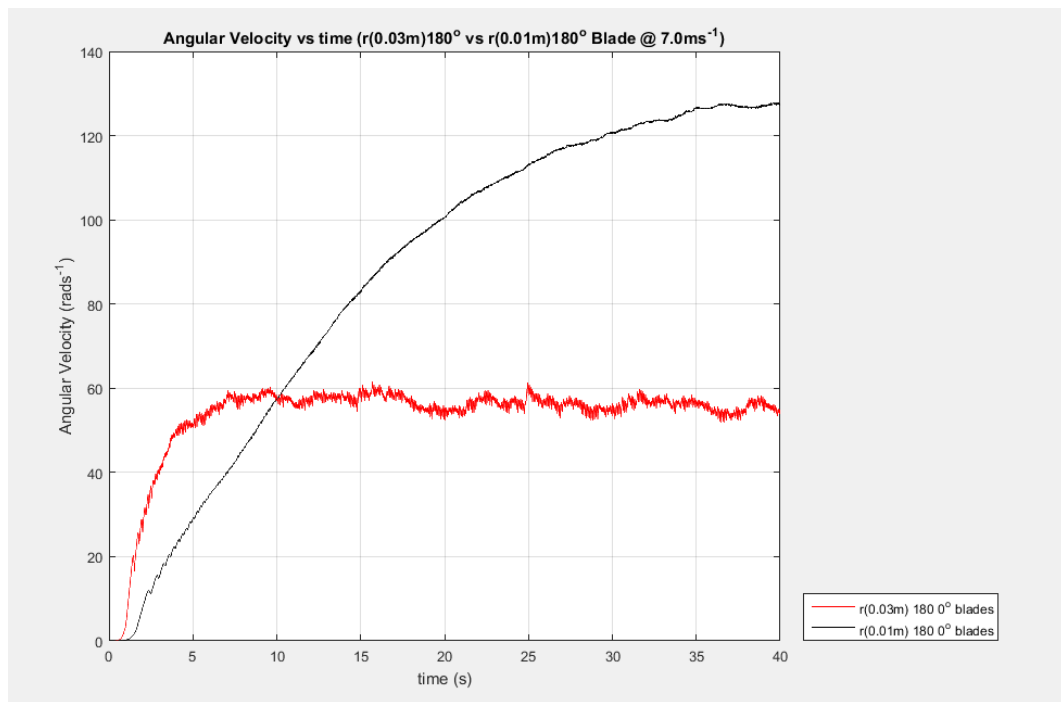


Figure 61: Comparison of (180°) turbine radius at 7.0 ms<sup>-1</sup>.

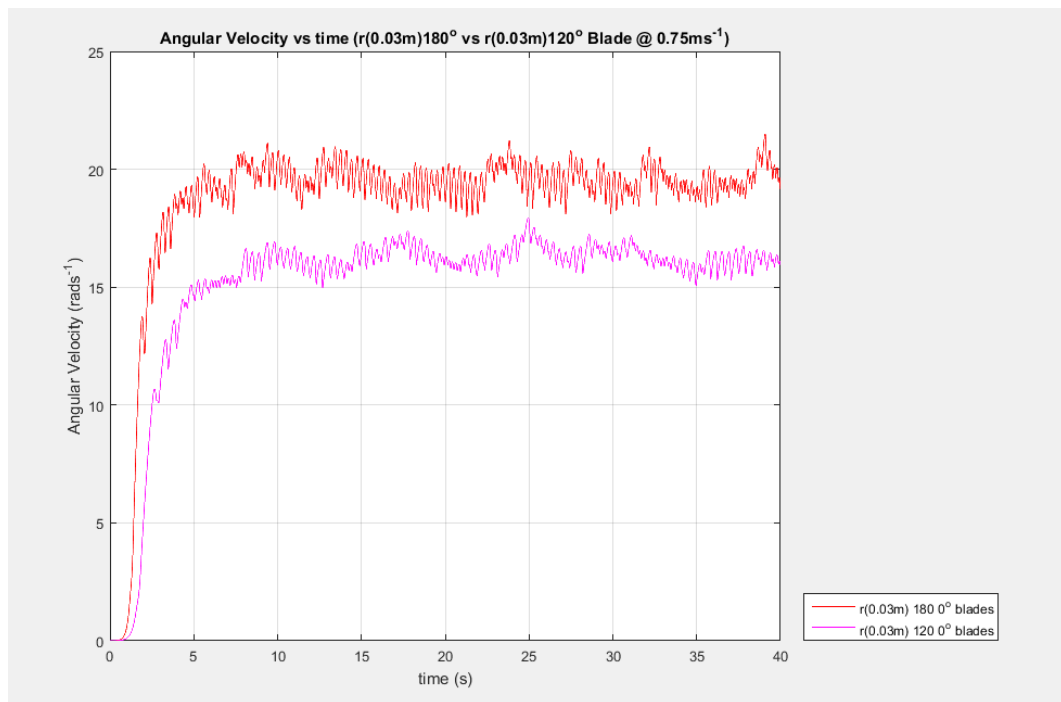


Figure 62: Comparison of (0.03 m) turbine blade angle at 0.75 ms<sup>-1</sup>.

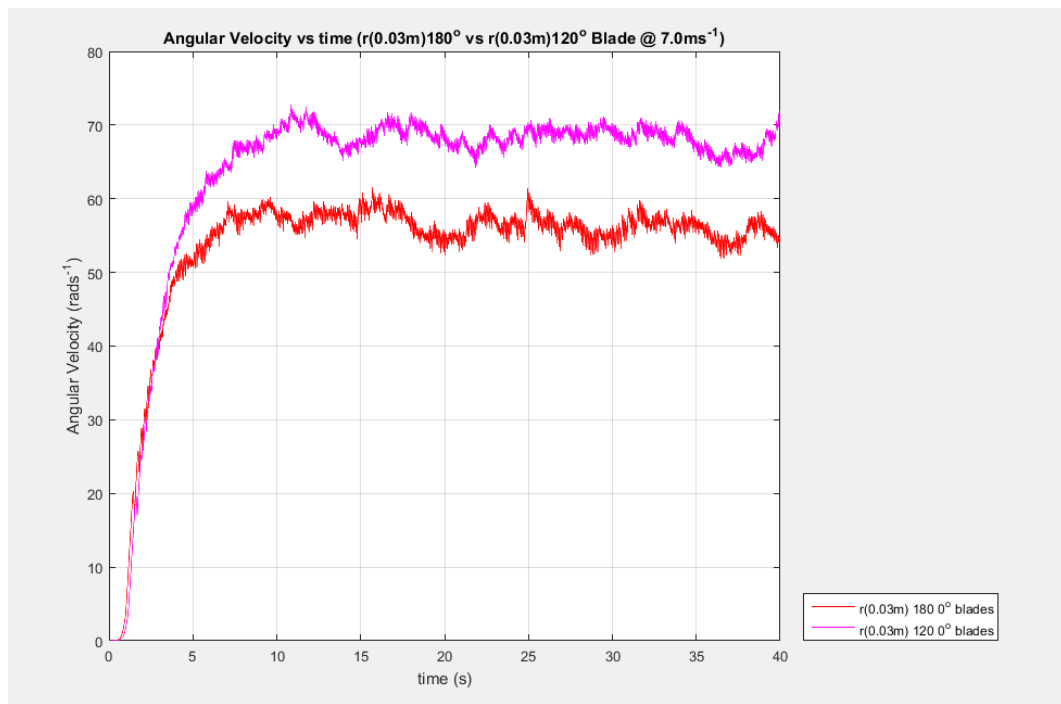


Figure 63: Comparison of (0.03 m) blade angle at 7.0 ms<sup>-1</sup>.

## D3 MATLAB Simulation data: $0.75\text{ms}^{-1}$

### D3.1 Acceleration with Offset data

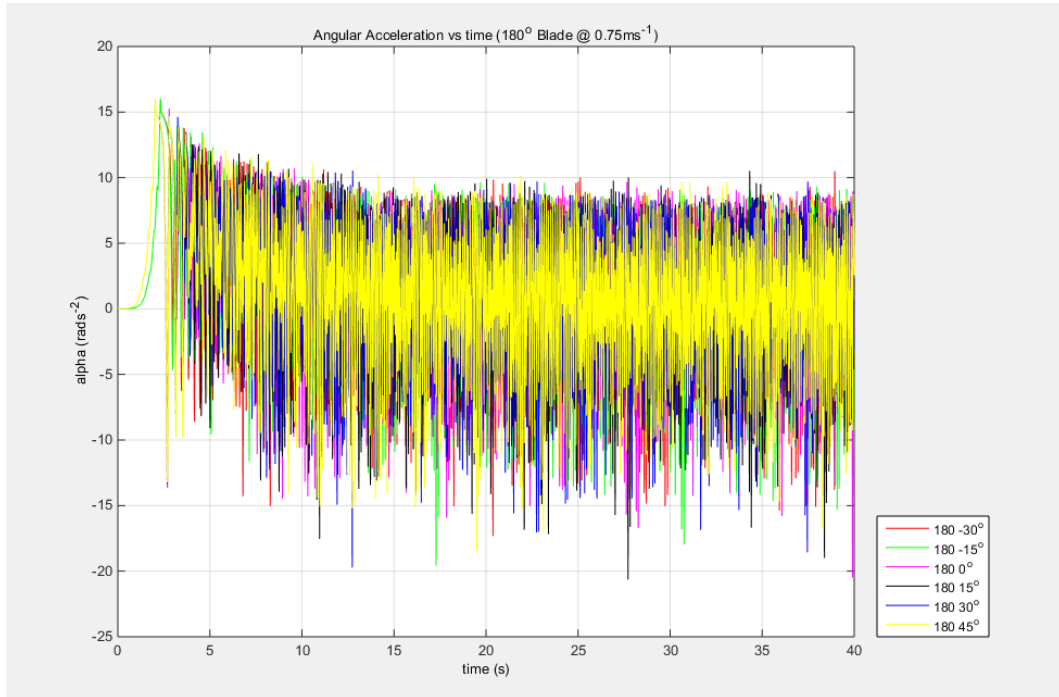


Figure 64: Angular acceleration of all offsets for  $180^\circ$  blade at  $0.75\text{ms}^{-1}$ .

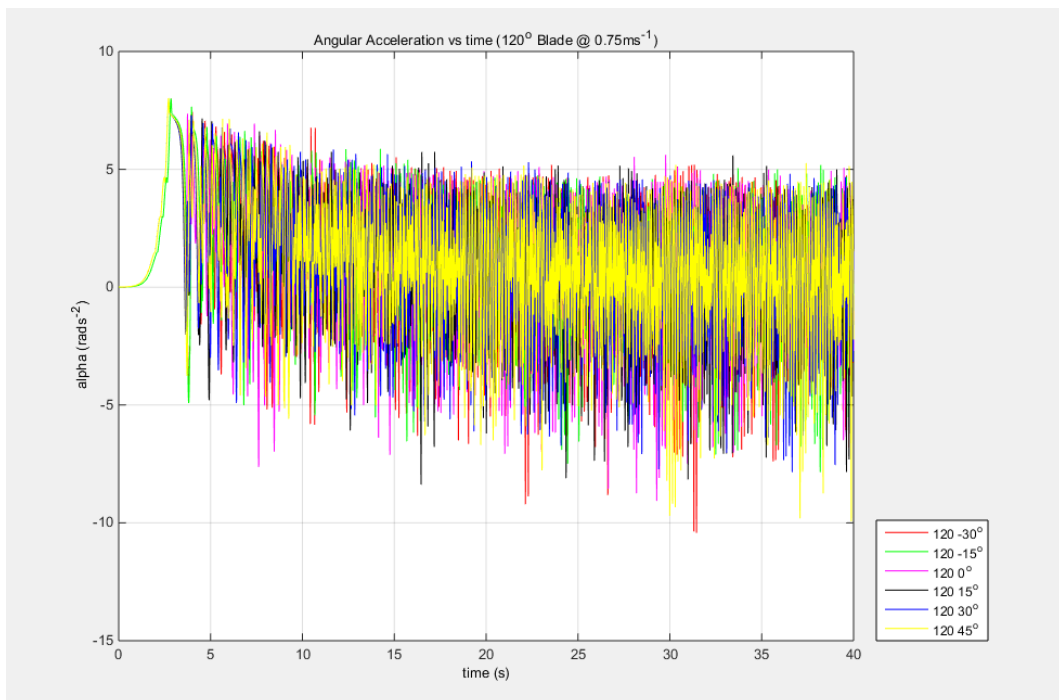


Figure 65: Angular acceleration of all offsets for  $120^\circ$  blade at  $0.75\text{ms}^{-1}$ .



### D3.2 Velocity with Offset data

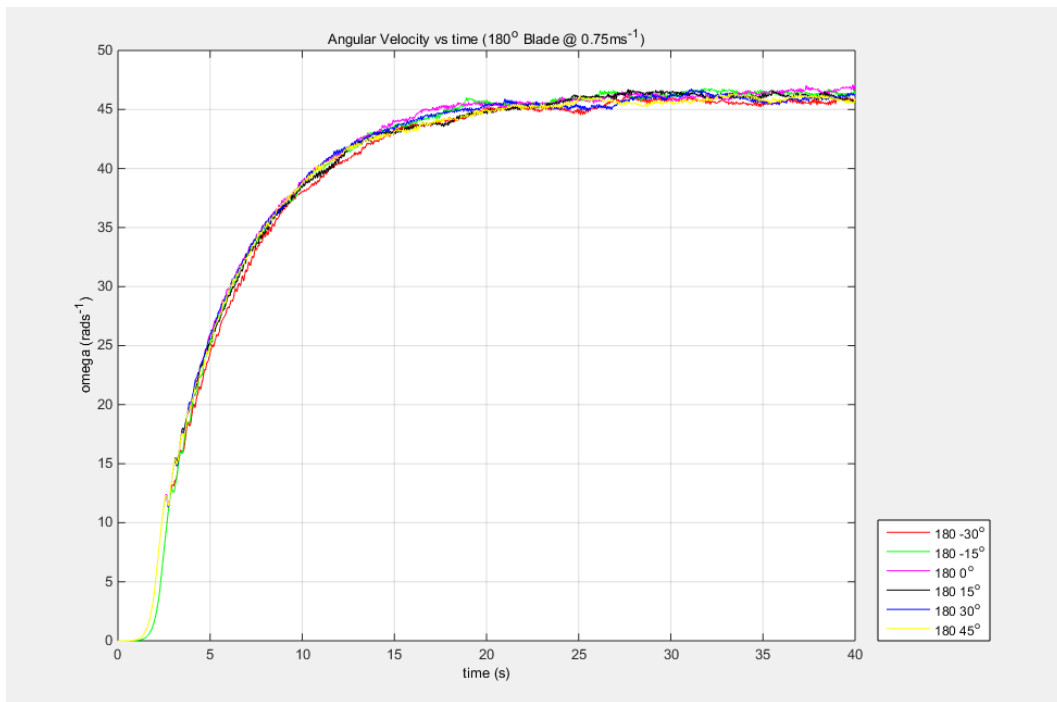


Figure 66: Angular velocity for all offsets of  $180^\circ$  blade at  $0.75\text{ ms}^{-1}$ .

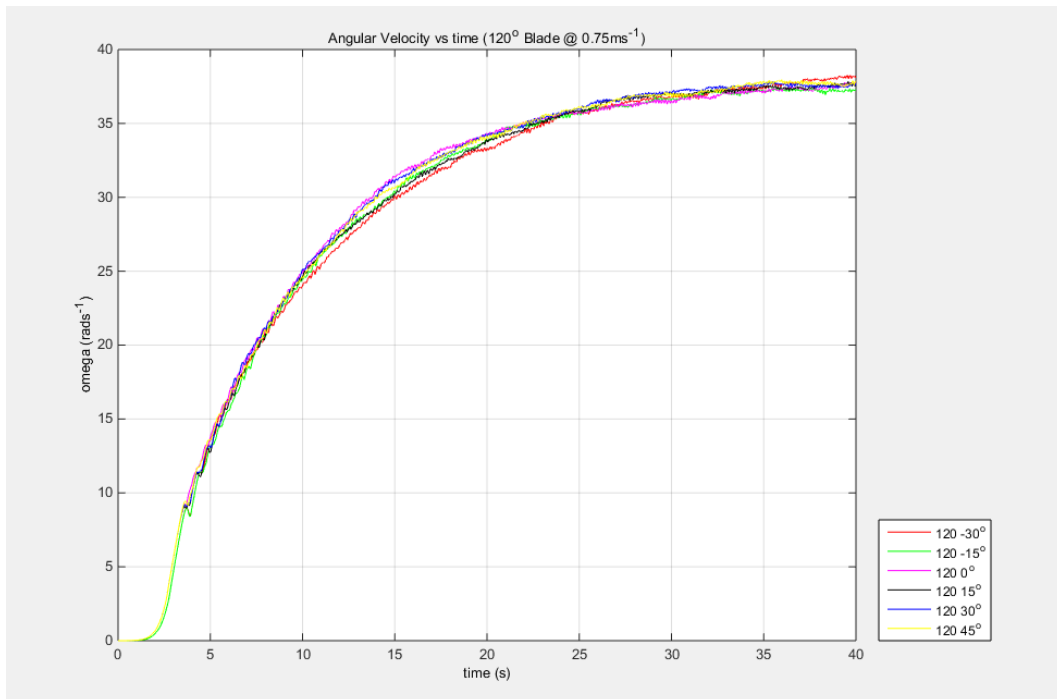


Figure 67: Angular velocity for all offsets of  $120^\circ$  blade at  $0.75\text{ ms}^{-1}$ .

### D3.3 Tip Speed with Offset data

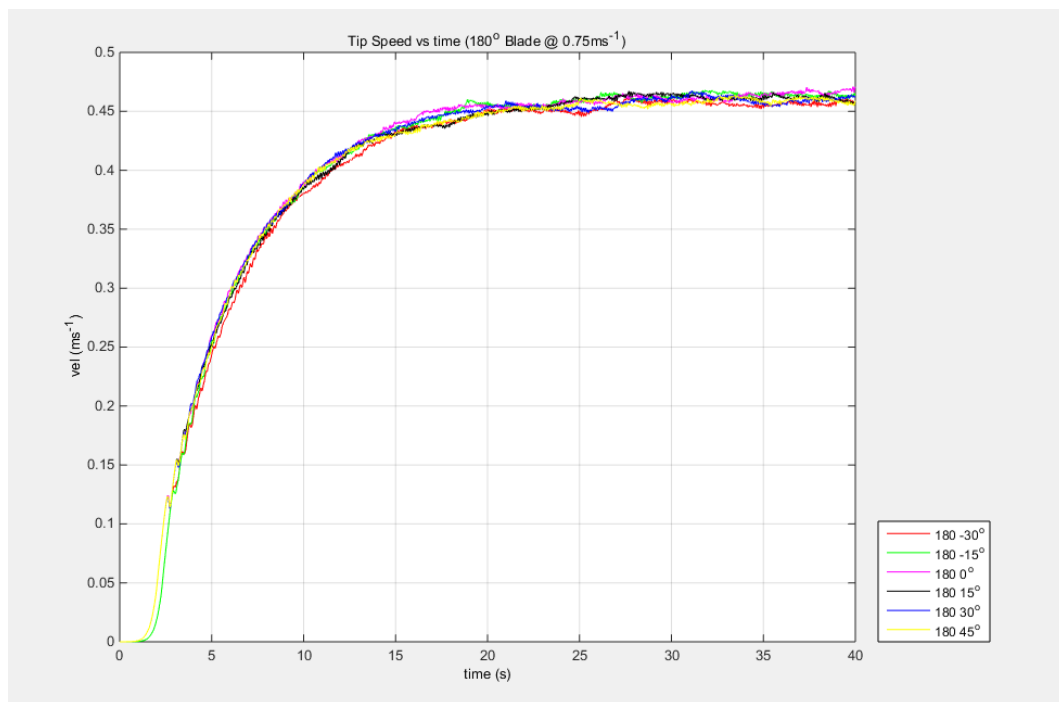


Figure 68: Tip speed for all offsets of 180° blade at 0.75 ms<sup>-1</sup>.

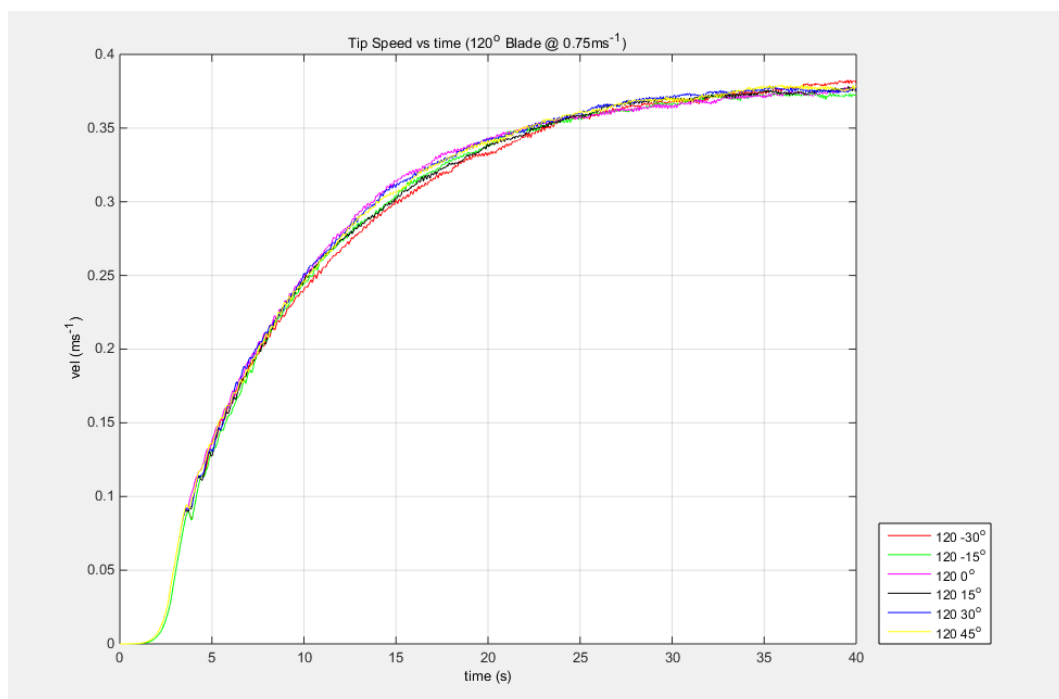


Figure 69: Tip speed for all offsets of 120° blade at 0.75 ms<sup>-1</sup>.

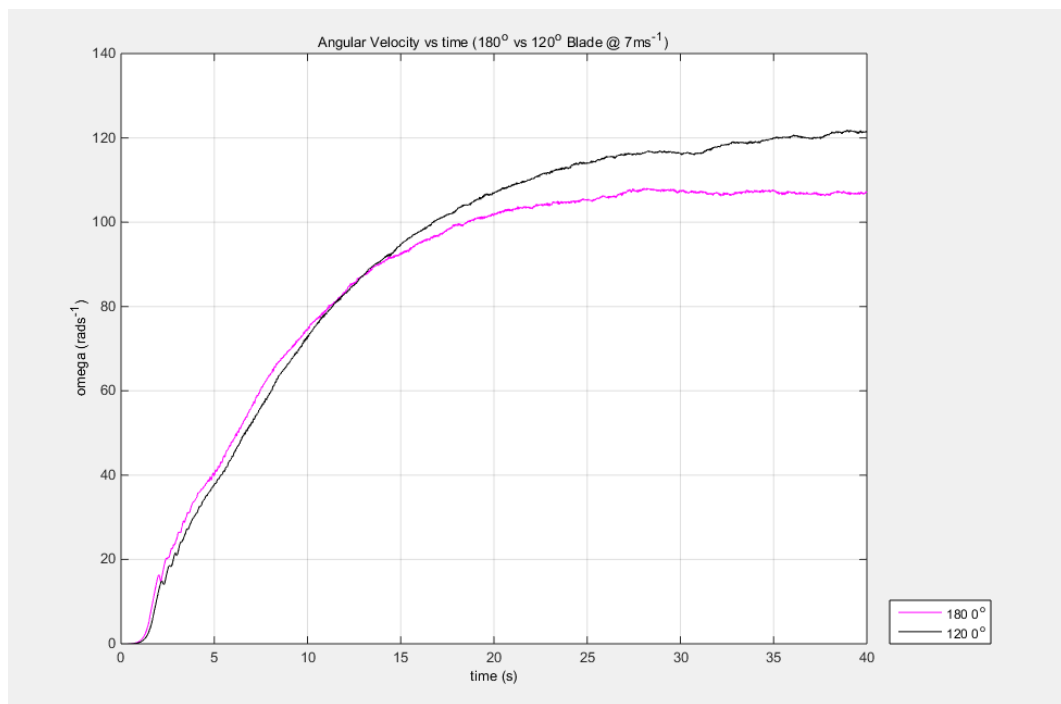


Figure 70: Comparison of angular velocity for  $180^\circ$  vs  $120^\circ$  blades at  $7.0\text{ms}^{-1}$ .

## D4 MATLAB Simulation data: $7.0\text{ms}^{-1}$

### D4.1 Acceleration with Offset data

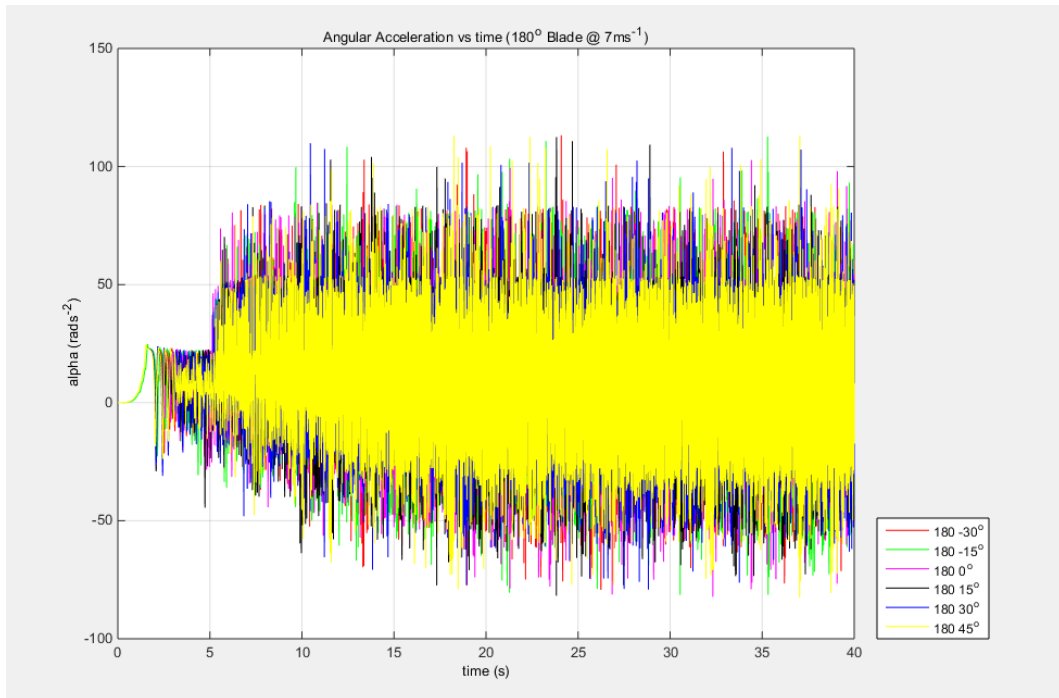


Figure 71: Angular acceleration of all offsets for  $180^\circ$  blade at  $7.0\text{ms}^{-1}$ .

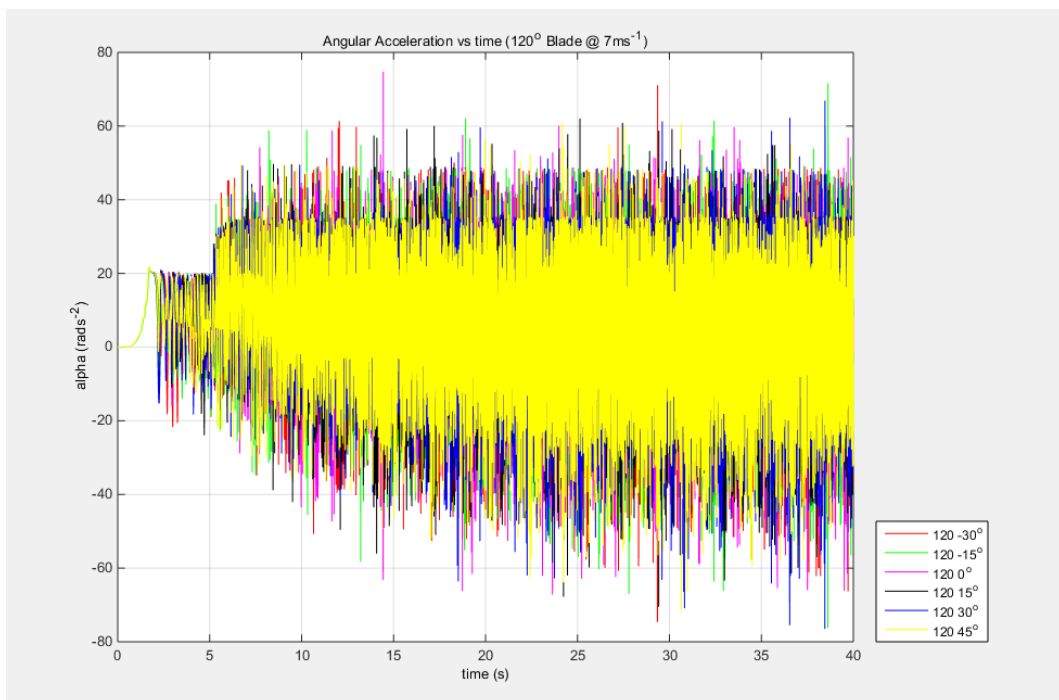


Figure 72: Angular acceleration of all offsets for  $120^\circ$  blade at  $7.0\text{ms}^{-1}$ .

## D4.2 Velocity with Offset data

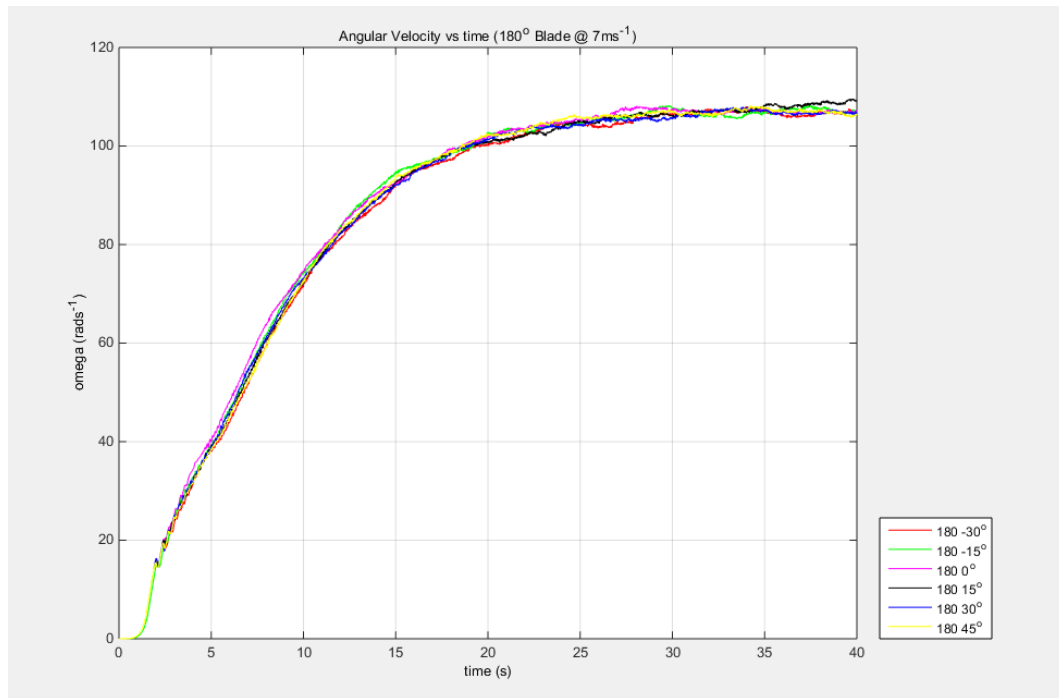


Figure 73: Angular velocity for all offsets of 180° blade at 7.0 ms<sup>-1</sup>.

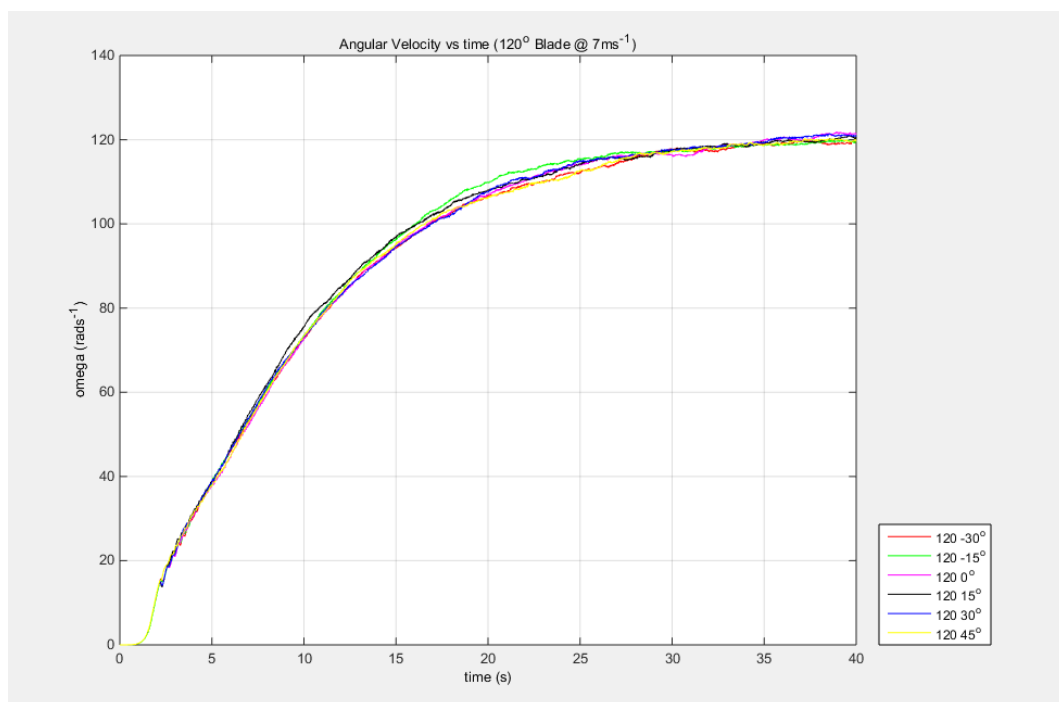


Figure 74: Angular velocity for all offsets of 120° blade at 7.0 ms<sup>-1</sup>.

### D4.3 Tip Speed with Offset data

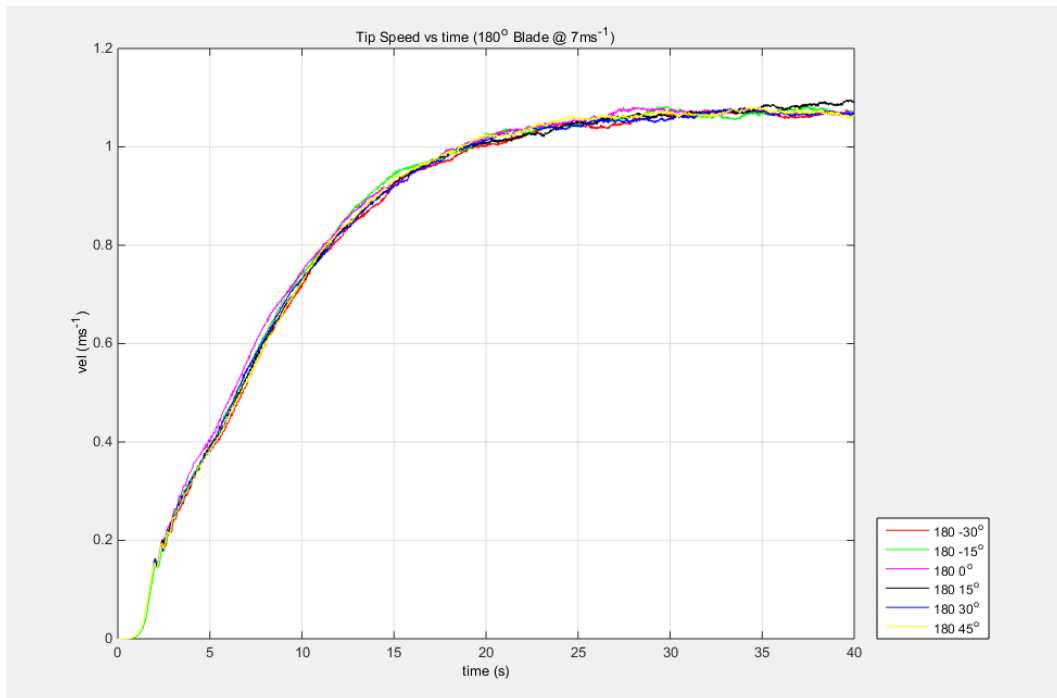


Figure 75: Tip speed for all offsets of 180° blade at 7.0 ms<sup>-1</sup>.

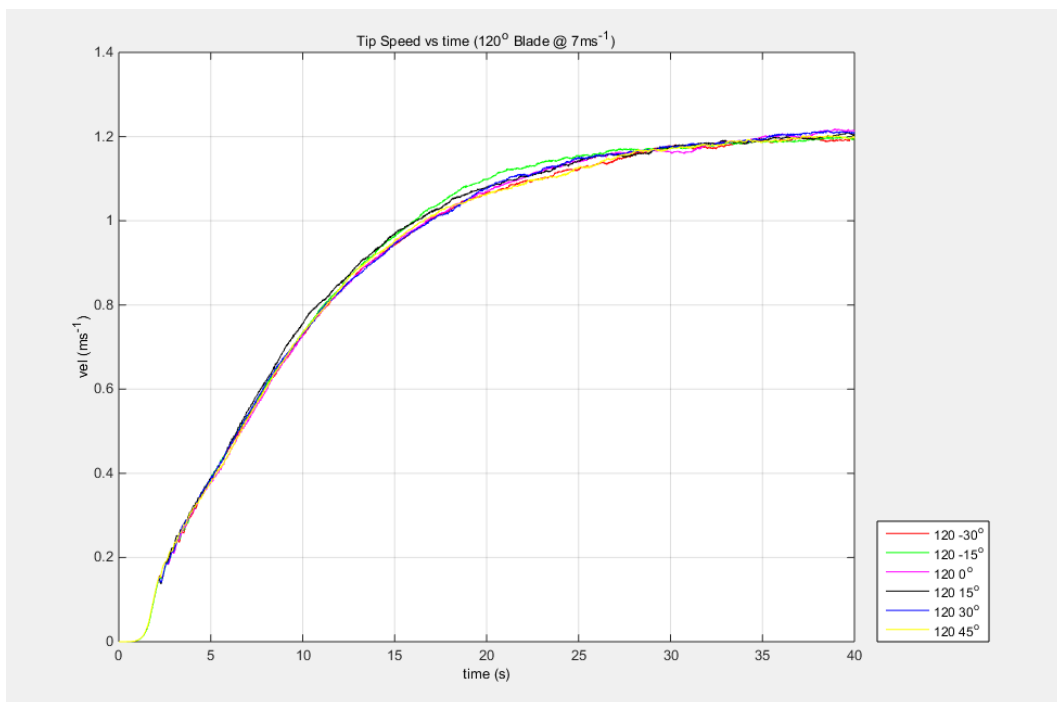


Figure 76: Tip speed for all offsets of 120° blade at 7.0 ms<sup>-1</sup>.

## Appendix E

### E1 CFD Force Data

	Angle degrees	CFD X N/mm	CFD Y N/mm
180 @ 6.6m/s	0	1.0245	0.0431
	15	1.1648	-0.7684
	30	1.7057	0.0062
	45	1.3944	-0.3866
	60	1.0194	-0.1344
	75	0.3009	-0.5551
	90	0.2651	0.7284
	105	0.5199	-0.9912
	120	0.6191	0.4009
	135	0.2357	-0.7591
	150	0.2674	-0.7711
	165	0.3051	-0.07
	180	0.2949	0.01
180 @ 15.1m/s	0	5.0311	0.4177
	15	6.5471	-4.1455
	30	9.1236	0.2981
	45	7.3743	-1.1963
	60	2.9686	-1.3931
	75	1.6303	-2.8565
	90	1.1745	3.5476
	105	2.0162	-3.7832
	120	3.2566	0.0908
	135	2.8684	0.4408
	150	1.9149	-3.6196
	165	1.2763	-0.5161
	180	2.3688	-0.1833
180 @ 20.1m/s	0	8.9236	0.8041
	15	11.39	-7.2697
	30	16.9426	0.4339
	45	12.8993	-0.9388
	60	4.9974	-3.1254
	75	2.5432	-4.9071
	90	2.0693	6.4153
	105	2.6466	-4.2103
	120	5.428	-3.6606
	135	5.6685	2.6694
	150	3.3551	-5.7005
	165	4.0785	-0.338
	180	4.5072	-0.0032

Figure 77: EXCEL worksheet showing the total x and y components of force from the CFD solutions for the 180° blade at the three wind speeds tested.

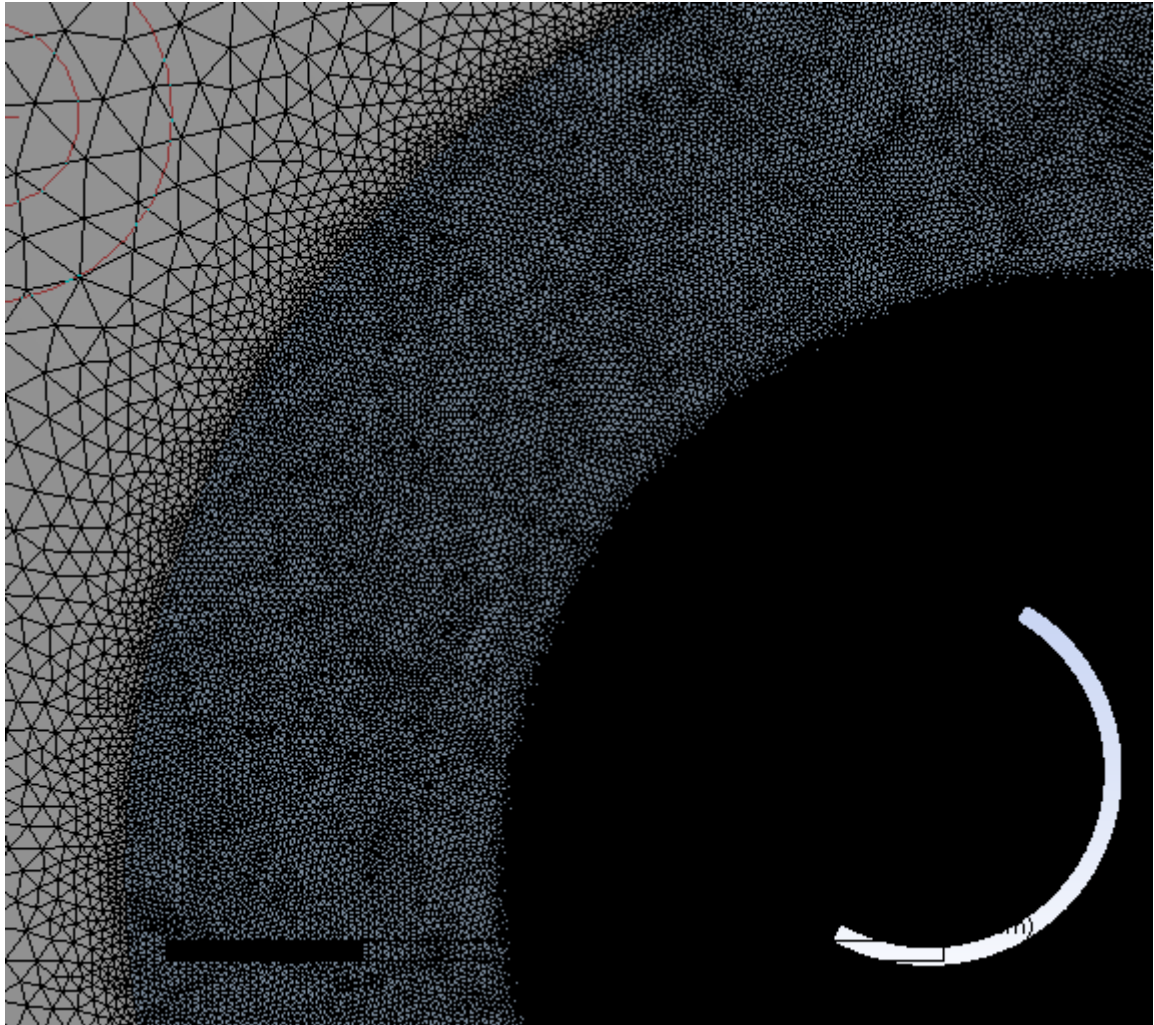
## E2 Domain for Transient Solution



Figure 78: Domain of the transient solution mesh showing the three separate meshing regions.



### E3 Mesh Refinement for Transient Solution



*Figure 79: Image showing the three relative mesh sizes in each zone, used for the transient solution.*

#### E4 Inflation on Blade for Transient Solution

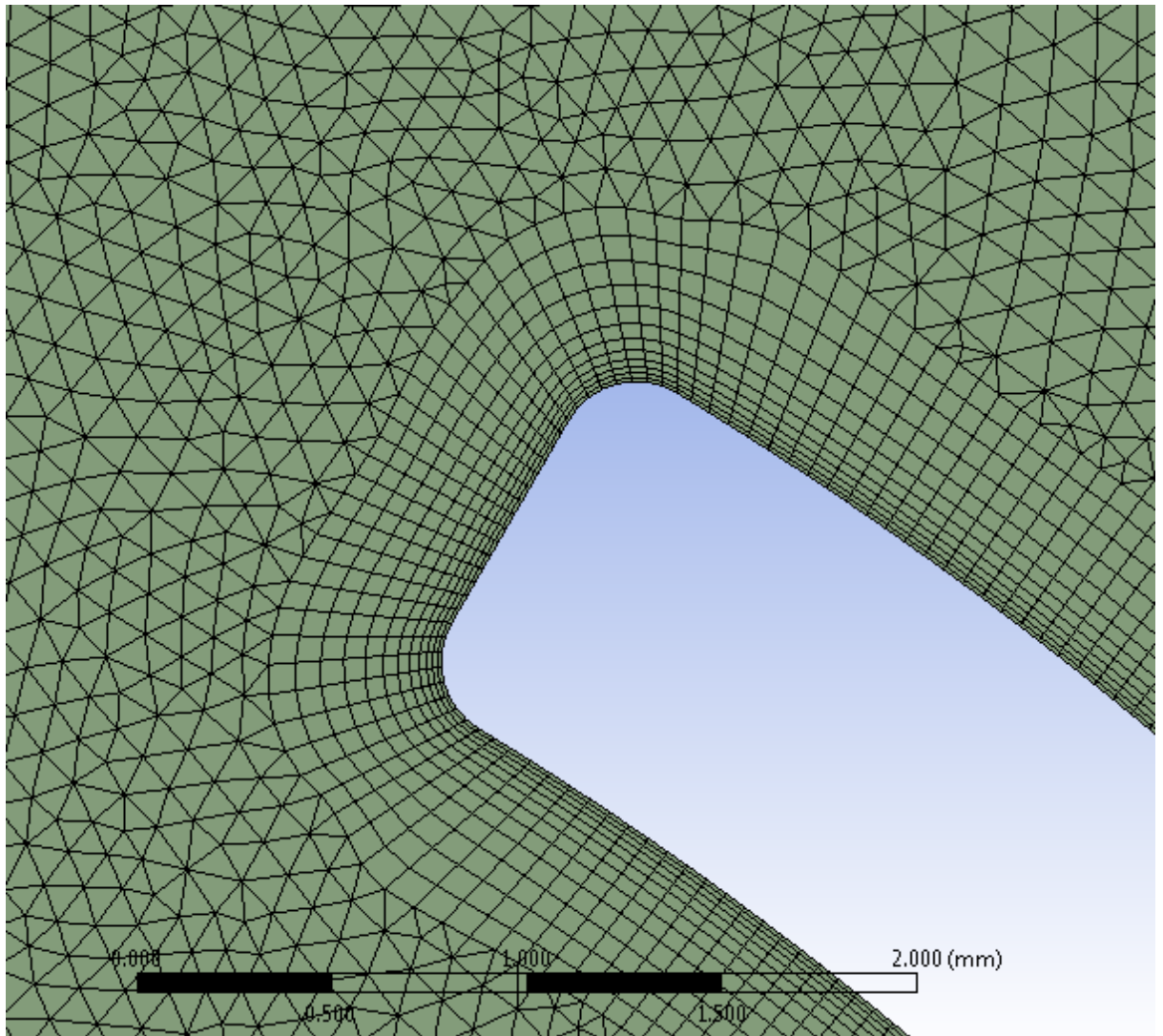


*Figure 80: Close up of the mesh around the blade surface region showing inflation from the surface, the 0.2mm rounded corners, and the triangular mesh (for the transient solution).*

## E5 Transient Solution Parameters

### Run Calculation

Check Case...

Preview Mesh Motion...

Time Stepping Method

Fixed

Time Step Size (s)

0.02

Number of Time Steps

50

Settings...

Options

☐ Extrapolate Variables

☐ Data Sampling for Time Statistics

Sampling Interval

1

Sampling Options...

Time Sampled (s)

0

Max Iterations/Time Step Reporting Interval

50

10

Profile Update Interval

1

Data File Quantities...

Acoustic Signals...

Calculate

Help

### General

Mesh

Scale...

Check

Report Quality

Display...

Solver

Type

☒ Pressure-Based
 ☐ Density-Based

Velocity Formulation

☒ Absolute
 ☐ Relative

Time

☐ Steady
 ☒ Transient

2D Space

☒ Planar
 ☐ Axisymmetric
 ☐ Axisymmetric Swirl

☒ Gravity

Units...

Gravitational Acceleration

X (m/s<sup>2</sup>)

0

Y (m/s<sup>2</sup>)

9.81

Z (m/s<sup>2</sup>)

0

Help

Mesh Quality:

Minimum Orthogonal Quality = 3.37249e-01  
(Orthogonal Quality ranges from 0 to 1, where values close to 0 correspond to low quality.)

Maximum Ortho Skew = 3.65994e-01  
(Ortho Skew ranges from 0 to 1, where values close to 1 correspond to low quality.)

Maximum Aspect Ratio = 6.54642e+00

Figure 81: Solution parameters image 1, transient setup and mesh statistics.

- 48 -

### Solution Methods

Pressure-Velocity Coupling

Scheme  
PISO

Skewness Correction  
1

Neighbor Correction  
1

☒ Skewness-Neighbor Coupling

### Spatial Discretization

Gradient  
Least Squares Cell Based

Pressure  
Second Order

Momentum  
Second Order Upwind

Turbulent Kinetic Energy  
First Order Upwind

Specific Dissipation Rate  
First Order Upwind

### Transient Formulation

First Order Implicit

☐ Non-Iterative Time Advancement

☐ Frozen Flux Formulation

☐ Warped-Face Gradient Correction

☐ High Order Term Relaxation

Options...

Default

Help

### Models

Models

Multiphase - Off

Energy - Off

Viscous - Transition SST (4 eqn)

Radiation - Off

Heat Exchanger - Off

Species - Off

Discrete Phase - Off

Solidification & Melting - Off

Acoustics - Off

Electric Potential - Off

Edit...

Help

Figure 82: Transient solution setup using PISO scheme and the transition SST turbulence model, suitable for flows where separation of the boundary layer is apparent.

## E6 Pressure field for Transient Solution

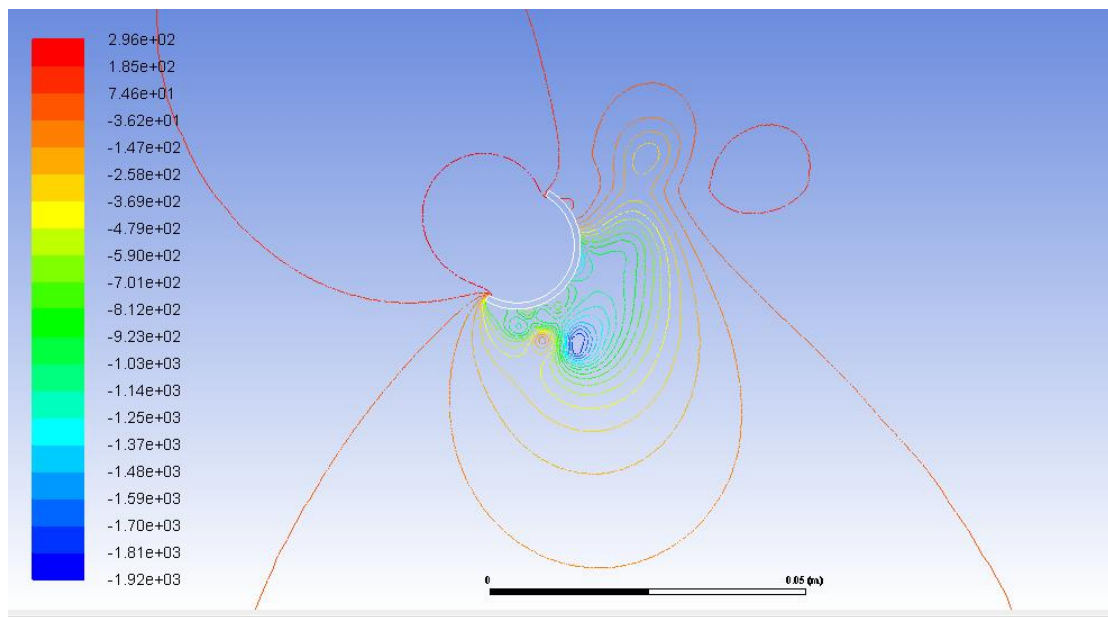


Figure 83: Pressure field from transient solution showing detached vortex in low pressure (blue) region of the flow.

## E7 Velocity field for Transient Solution

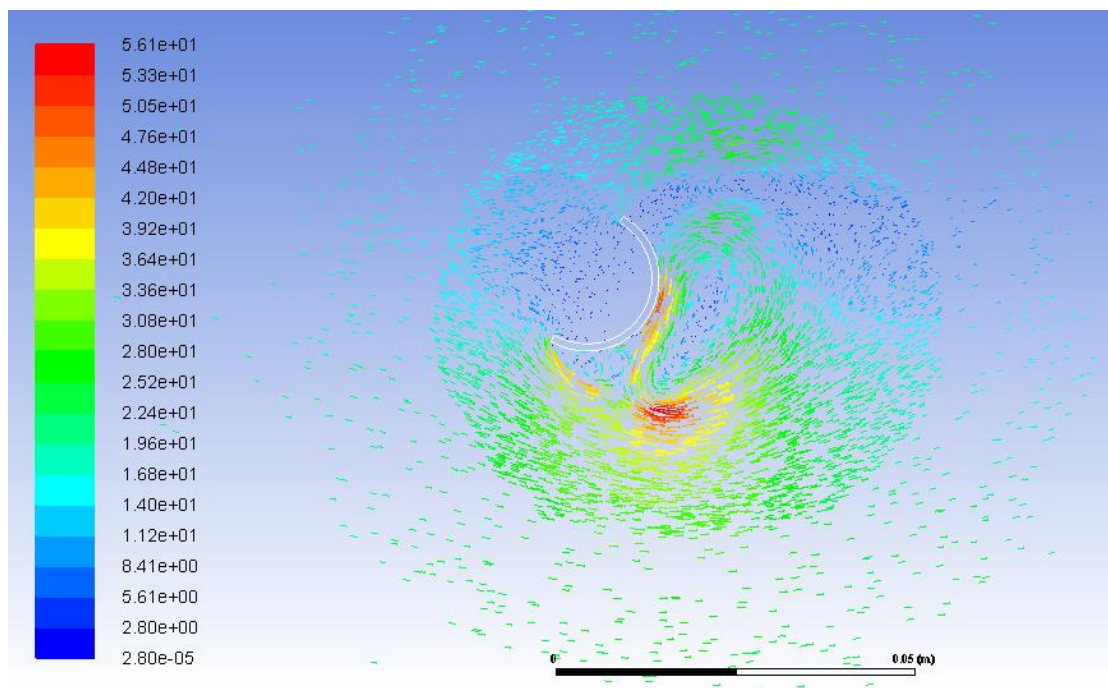


Figure 84: Velocity field from the transient solution showing high velocity flow (red) on the lower side of the image, and lower velocity flow (blue) on the upper side of the image, with some flow back across the rear side of the blade from the vortex.

## E8 Turbulent Kinetic Energy for Transient Solution

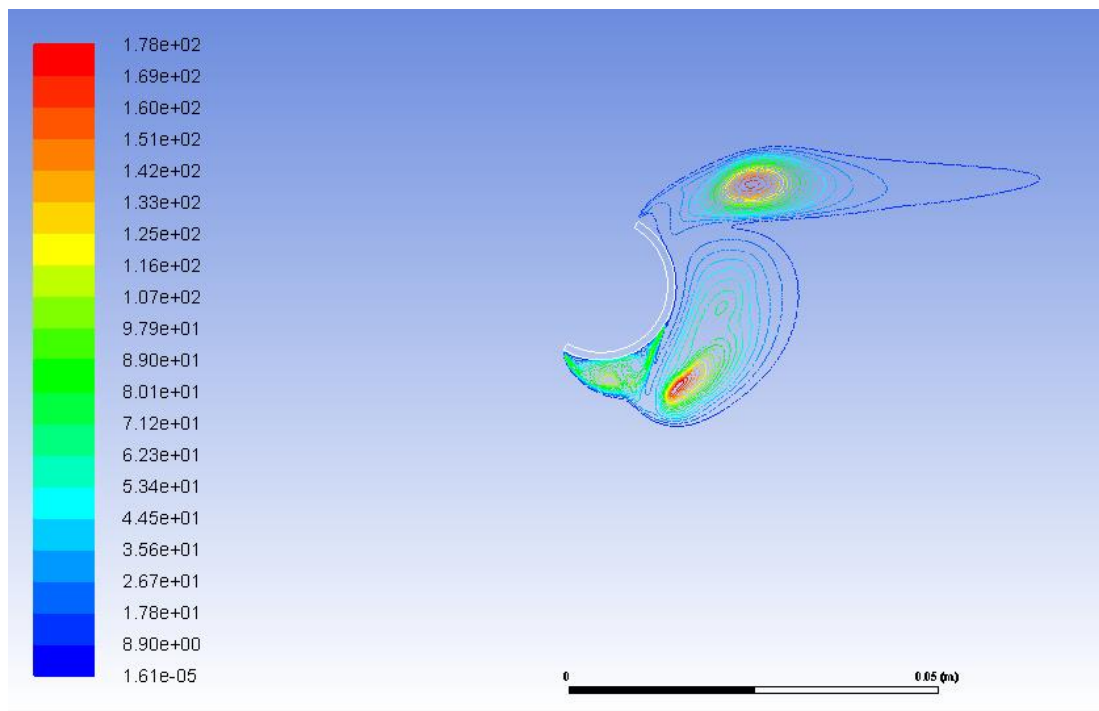


Figure 85: Turbulent kinetic energy regions from the transient solution.



## \Appendix F

### F1 Wind Tunnel spreadsheet data

	F_tang @ v	A(g) raw	A(g)	B(g)	C(g)	A(N) (*lever)/(6 0mm) per	B(N) (*lever)/(6 0mm) per	C(N) (*lever)/(6 0mm) per
<b>180(6.6)</b>								
0	2.8	22	19.2			0.7466	0.0000	0.0000
30	2.8	18.2	15.4		7.2	0.5988	0.0000	0.2800
60	2.8	12.4	9.6		8.2	0.3733	0.0000	0.3188
90	2.8	7.5	4.7	5.8		0.1828	0.2255	0.0000
120	2.8	10.3	7.5	3.6		0.2916	0.1400	0.0000
150	2.8	10.8	8	2.7		0.3111	0.1050	0.0000
180	2.8	10.3	7.5			0.2916	0.0000	0.0000
<b>120(6.6)</b>			0					
0	2.8	17.4	14.6			0.5677	0.0000	0.0000
30	2.8	15.9	13.1		6.9	0.5094	0.0000	0.2683
60	2.8	9.9	7.1		11.2	0.2761	0.0000	0.4355
90	2.8	5.1	2.3	2.4		0.0894	0.0933	0.0000
120	2.8	7.5	4.7	1.7		0.1828	0.0661	0.0000
150	2.8	11.7	8.9			0.3461	0.0000	0.0000
180	2.8	12.6	9.8			0.3811	0.0000	0.0000
<b>180(15.1)</b>			0					
0	12.3	105	92.7			3.6045	0.0000	0.0000
30	12.3	92.8	80.5		36.1	3.1302	0.0000	1.4037
60	12.3	68	55.7		39.6	2.1658	0.0000	1.5398
90	12.3	40.6	28.3	26.2		1.1004	1.0188	0.0000
120	12.3	65.2	52.9	16.7		2.0570	0.6494	0.0000
150	12.3	71	58.7	4.6		2.2825	0.1789	0.0000
180	12.3	62.5	50.2			1.9520	0.0000	0.0000
<b>120(15.1)</b>			0					
0	12.3	89	76.7			2.9824	0.0000	0.0000
30	12.3	75	62.7		18.9	2.4380	0.0000	0.7349
60	12.3	47	34.7		58	1.3493	0.0000	2.2553
90	12.3	30.1	17.8	17.9		0.6921	0.6960	0.0000
120	12.3	48.3	36	15.8		1.3998	0.6144	0.0000
150	12.3	61	48.7			1.8936	0.0000	0.0000
180	12.3	65.7	53.4			2.0764	0.0000	0.0000
<b>180(20.1)</b>			0					
0	21.4	187	165.6			6.4392	0.0000	0.0000
30	21.4	161	139.6		81.6	5.4282	0.0000	3.1729
60	21.4	129	107.6		53	4.1839	0.0000	2.0608
90	21.4	70	48.6	46		1.8898	1.7887	0.0000
120	21.4	100	78.6	21		3.0563	0.8166	0.0000
150	21.4	110	88.6			3.4451	0.0000	0.0000
180	21.4	107	85.6			3.3285	0.0000	0.0000
<b>120(20.1)</b>			0					
0	21.4	157	135.6			5.2727	0.0000	0.0000
30	21.4	134	112.6		70	4.3783	0.0000	2.7219
60	21.4	79	57.6		90	2.2397	0.0000	3.4996
90	21.4	51	29.6	29		1.1510	1.1276	0.0000
120	21.4	76	54.6	22.5		2.1231	0.8749	0.0000
150	21.4	102	80.6			3.1340	0.0000	0.0000
180	21.4	111	89.6			3.4840	0.0000	0.0000
rig v dist	41.5	mm						
tunl v dist	174.5	mm						
lever factor	0.23782235							

Figure 86: EXCEL spreadsheet 1 for wind tunnel data.

	1(Pa)	2(Pa)	3(Pa)	4(Pa)	5(Pa)	Pstag (Pa)	Pstat(Pa)	v (m/s)	1(Pa) delta	2(Pa) delta	3(Pa) delta	4(Pa) delta	5(Pa) delta
180(6.6)													
0	94903	94900	94890	94908	94906	94954	94933	6.12372436	30	33	43	25	27
30	94885	94878	94876	94877	94886			6.1	48	55	57	56	47
60	94883	94881	94878	94881	94878			6.1	50	52	55	52	55
90	94882	94880	94879	94882	94880			6.1	51	53	54	51	53
120	94882	94870	94869	94877	94880			6.1	51	63	64	56	53
150	94882	94866	94860	94866	94880			6.1	51	67	73	67	53
180	94882	94860	94846	94862	94880			6.1	51	73	87	71	53
120(6.6)									94933	94933	94933	94933	94933
0	94861	94846	94839	94847	94850			6.1	72	87	94	86	83
30	94832	94832	94829	94837	94837			6.1	101	101	104	96	96
60	94820	94824	94814	94814	94820			6.1	113	109	119	119	113
90	94790	94790	94784	94790	94790			6.1	143	143	149	143	143
120	94790	94786	94777	94787	94790			6.1	143	147	156	146	143
150	94790	94772	94757	94764	94790			6.1	143	161	176	169	143
180	94790	94764	94761	94766	94790			6.1	143	169	172	167	143
180(15.1)									94933	94933	94933	94933	94933
0	94560	94545	94487	94532	94560	94714	94586	15.1185789	94933	94933	94933	94933	94933
30	94564	94560	94510	94550	94568			15.1	373	388	446	401	373
60	94563	94565	94550	94564	94566			15.1	369	373	423	383	365
90	94571	94565	94558	94561	94566			15.1	370	368	383	369	367
120	94565	94549	94528	94561	94566			15.1	362	368	375	372	367
150	94572	94559	94505	94565	94576			15.1	368	384	405	372	367
180	94572	94560	94501	94568	94569			15.1	361	374	428	368	357
120(15.1)									94933	94933	94933	94933	94933
0	94591	94571	94501	94572	94585			15.1	94933	94933	94933	94933	94933
30	94588	94575	94521	94562	94585			15.1	342	362	432	361	348
60	94592	94587	94584	94580	94587			15.1	345	358	412	371	348
90	94572	94570	94570	94574	94568			15.1	341	346	349	353	346
120	94575	94577	94578	94575	94573			15.1	361	363	363	359	365
150	94570	94555	94515	94563	94564			15.1	358	356	355	358	360
180	94568	94565	94500	94560	94560			15.1	363	378	418	370	369
180(20.1)									94933	94933	94933	94933	94933
0	94715	94710	94388	94712	94716	94707	94481	20.0890873	94933	94933	94933	94933	94933
30	94710	94701	94360	94710	94710			20.1	218	223	545	221	217
60	94713	94714	94380	94720	94717			20.1	223	232	573	223	223
90	94725	94720	94570	94719	94716			20.1	220	219	553	213	216
120	94720	94720	94410	94720	94725			20.1	208	213	363	214	217
150	94723	94723	94412	94729	94724			20.1	213	213	523	213	208
180	94660	94660	94345	94665	94670			20.1	210	210	521	204	209
120(20.1)									94933	94933	94933	94933	94933
0	94730	94730	94405	94730	94735			20.1	273	273	588	268	263
30	94737	94735	94405	94726	94726			20.1	94933	94933	94933	94933	94933
60	94728	94735	94560	94725	94727			20.1	203	203	528	203	198
90	94720	94720	94500	94725	94720			20.1	196	198	528	207	207
120	94700	94700	94390	94700	94700			20.1	205	198	373	208	206
150	94690	94690	94370	94690	94690			20.1	213	213	433	208	213
180	94685	94685	94370	94685	94685			20.1	233	233	543	233	233
									243	243	563	243	243
									248	248	563	248	248
rig v dist													
tunl v dist													
lever factor													

Figure: EXCEL spreadsheet 2 for wind tunnel data.



## F2 Dimensionless Parameter Table

$p = 1.14$	$A = 0.0012$				
V m/s	Re #	Cd @ 180	Cl @180	Cd @120	Cl @120
0	0	0.00	0.00	0.00	0.00
0		0.00	0.00	0.00	0.00
0		0.00	0.00	0.00	0.00
0		0.00	0.00	0.00	0.00
0		0.00	0.00	0.00	0.00
0		0.00	0.00	0.00	0.00
0		0.00	0.00	0.00	0.00
0		0.00	0.00	0.00	0.00
0		0.00	0.00	0.00	0.00
0		0.00	0.00	0.00	0.00
0		0.00	0.00	0.00	0.00
0		0.00	0.00	0.00	0.00
0		0.00	0.00	0.00	0.00
0		0.00	0.00	0.00	0.00
0		0.00	0.00	0.00	0.00
6.6	7600	12.53	10.70	10.87	17.15
6.6		25.06	0.00	22.36	0.00
6.6		20.10	-9.40	20.06	-10.57
6.6		12.53	-10.70	10.87	-17.15
6.6		6.13	7.57	3.52	3.68
6.6		9.79	4.70	7.20	2.60
6.6		10.44	3.52	13.63	0.00
6.6		9.79	0.00	15.01	0.00
6.6		10.44	-3.52	13.63	0.00
6.6		9.79	-4.70	7.20	-2.60
6.6		6.13	-7.57	3.52	-3.68
6.6		12.53	10.70	10.87	17.15
6.6		20.10	9.40	20.06	10.57
6.6		25.06	0.00	22.36	0.00
6.6		9.79	-4.70	7.20	-2.60
15.1	17387.8788	13.89	9.87	10.15	16.97
15.1		23.11	0.00	22.44	0.00
15.1		20.07	-9.00	18.34	-5.53
15.1		13.89	-9.87	10.15	-16.97
15.1		7.06	6.53	5.21	5.24
15.1		13.19	4.16	10.53	4.62
15.1		14.64	1.15	14.25	0.00
15.1		12.52	0.00	15.62	0.00
15.1		14.64	-1.15	14.25	0.00
15.1		13.19	-4.16	10.53	-4.62
15.1		7.06	-6.53	5.21	-5.24
15.1		13.89	9.87	10.15	16.97
15.1		20.07	9.00	18.34	5.53
15.1		23.11	0.00	22.44	0.00
15.1		13.19	-4.16	10.53	-4.62
20.1	23145.4545	15.14	7.46	9.51	14.86
20.1		23.30	0.00	22.39	0.00
20.1		19.64	-11.48	18.59	-11.56
20.1		15.14	-7.46	9.51	-14.86
20.1		6.84	6.47	4.89	4.79
20.1		11.06	2.95	9.02	3.72
20.1		12.47	0.00	13.31	0.00
20.1		14.13	0.00	14.79	0.00
20.1		12.47	0.00	13.31	0.00
20.1		11.06	-2.95	9.02	-3.72
20.1		6.84	-6.47	4.89	-4.79
20.1		15.14	7.46	9.51	14.86
20.1		19.64	11.48	18.59	11.56
20.1		23.30	0.00	22.39	0.00
20.1		11.06	-2.95	9.02	-3.72

Figure 87: EXCEL spreadsheet showing  $C_D$  and  $C_L$  for various  $Re$  values.

### F3 Plots of Dimensionless Parameters

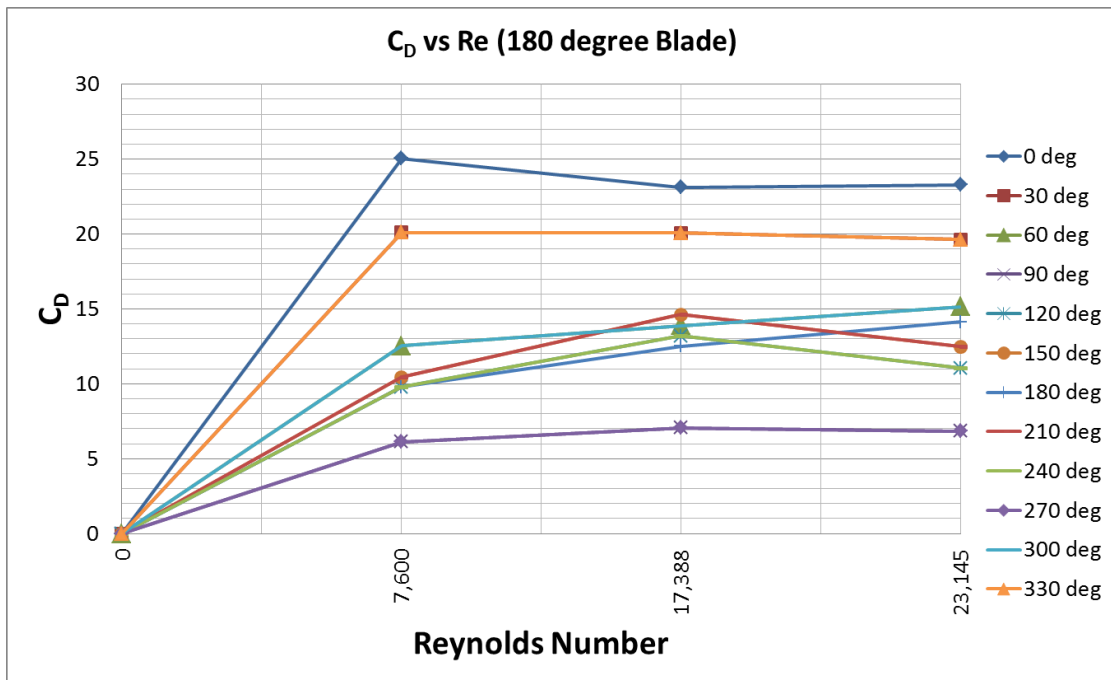


Figure 88: Plot of  $C_D$  vs Re for 180° blade.

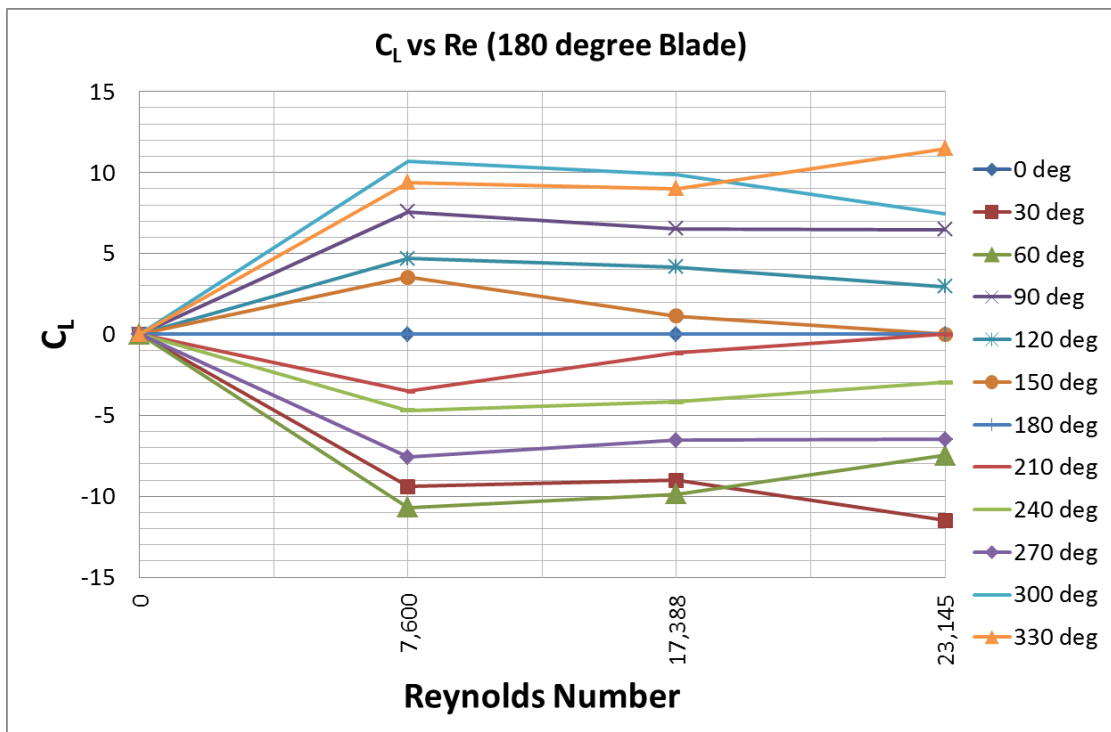


Figure 89: Plot of  $C_L$  vs Re for 180° blade.

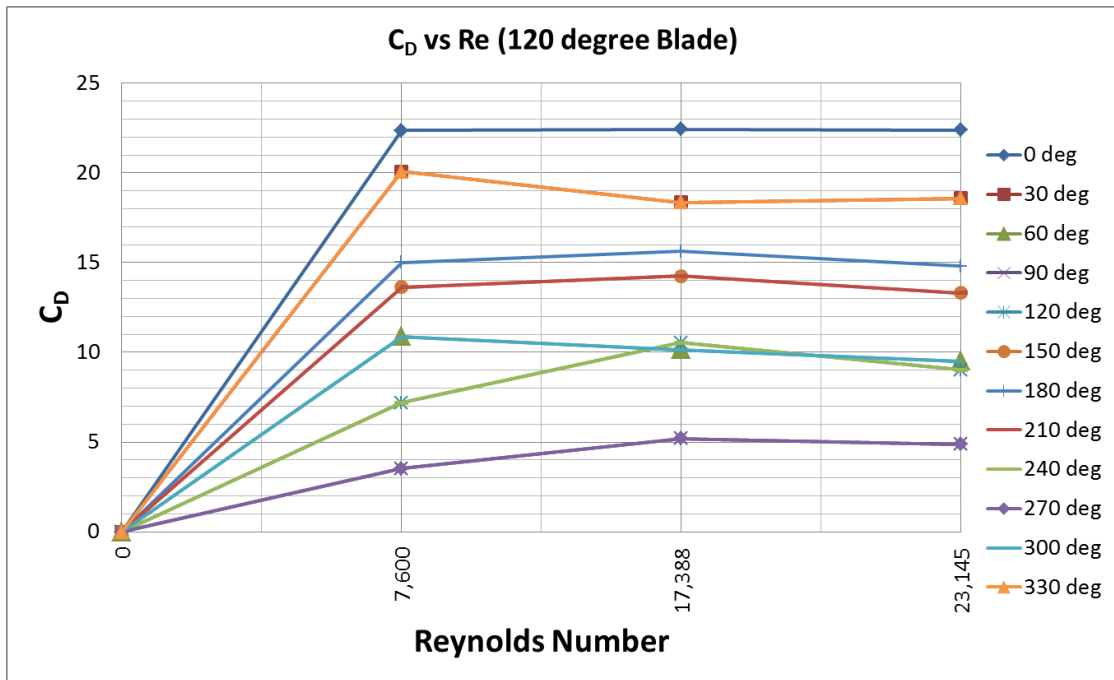


Figure 90: Plot of  $C_D$  vs Re for 120° blade.

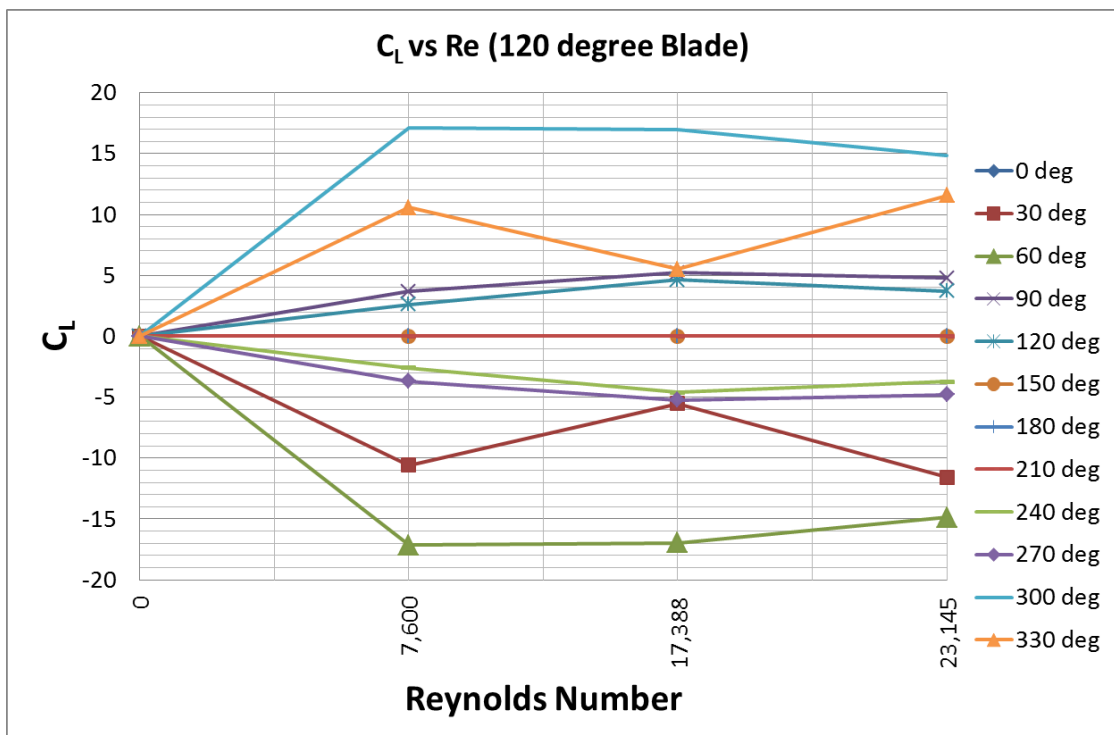


Figure 91: Plot of  $C_L$  vs Re for 120° blade.